

Measurement of the b-jet cross section at $\sqrt{s}=1.96$ TeV

O. Peters

May 28, 2003

Contents

1	Introduction	3
2	The Standard Model	5
2.1	Asymptotic Freedom	7
2.2	Heavy quark production	8
3	The Apparatus	15
3.1	The Tevatron	15
3.2	The DØ Detector	17
3.2.1	Inner Tracker	20
3.2.2	Calorimeter	22
3.2.3	Muon Detector	24
3.2.4	Forward Proton Detector	29
3.2.5	Luminosity Monitor	30
4	DØ Trigger System	33
4.1	Level 1	34
4.1.1	Level 1 Central Track Trigger	36
4.1.2	Level 1 Calorimeter Trigger	37
4.1.3	Level 1 Muon Trigger	37
4.2	Level 2	38
4.2.1	Central Track Preprocessor	39
4.2.2	Preshower Preprocessor	39
4.2.3	Calorimeter Preprocessor	39
4.2.4	Muon Preprocessor	40
4.3	Level 3	40
4.4	Triggers used for data selection	41
4.5	Efficiency for Jet+ μ Trigger	42
4.5.1	Level 1 Calorimeter Trigger Efficiency	42
4.5.2	Level 1 Muon Trigger efficiency	44

4.5.3	Trigger correlations	48
5	Offline Event Reconstruction	49
5.1	Central Track Reconstruction	49
5.2	Jet Reconstruction	49
5.3	Muon Reconstruction	68
5.3.1	Hit Reconstruction	68
5.3.2	Segment Reconstruction	75
5.3.3	Local Track Reconstruction	87
5.4	DØVE	96
6	Event Selection	99
6.1	Muon Identification	100
6.1.1	Cosmic ray contamination	103
6.1.2	Punch through	103
6.2	Jet Selection and Identification	105
6.2.1	Jet ID Efficiency	107
7	Muon + Jet Cross section	111
7.1	Differential cross section for μ + jet events	111
7.2	Efficiency corrections	113
7.3	Unfolding the μ +jet cross section	117
7.4	Kinematic acceptance corrections	120
8	B-jet cross section	123
8.1	Extraction of the b -jet component	125
8.1.1	P_T^{Rel} Tagging variable	125
8.1.2	Kinematic dependance	130
8.1.3	Template fit	133
8.2	b -jet cross section	137
8.2.1	Unfolding the b -jet cross section	137
8.2.2	Resolution and lepton corrections	138
8.3	Kinematic acceptance and branching ratio	146
9	Theory comparison	149
9.1	Comparison of data and theory	149
9.1.1	χ^2 comparison of data and theory	149
9.1.2	The correlation matrix for the b -content fit	153
9.2	Covariance matrix and result	154
9.3	Comparison to the uncorrected b -jet cross section	156
9.4	Conclusions	159

9.5 Outlook	159
A Glossary	165

Chapter 1

Introduction

As long as mankind has existed on the face of this earth, he has tried to unravel the mysteries of the nature of space surrounding him. From the ancient Greeks, who could merely philosophize that we only had four elements, to the high-energy accelerators and powerful computers that help use today to probe the smallest particles of nature, we are still trying to grasp what is around us. The real materialization of the modern study we now call particle physics took place at the start of the last century [27]. It can be said that it started with the discovery of the electron in 1897 by J.J. Thomson [34], who established the electron's charge and mass. Quickly after, γ rays were discovered, but not yet recognized as electromagnetic radiation. A crucial step to the understanding of sub-atomic particles was taken with the development of the theory of Quantum Mechanics by Planck around 1900. Soon after this, Einstein postulated his theory that light consisted of quanta that behaved like particles. From the 1910's through the 1930's the nuclear model was developed, with a model postulating a nucleus made up of protons and neutrons, bound together by the strong force and circled by electrons. However, it turned out that the world was not as simple as this, and these particles were just the lightest in a whole spectrum of particles. Soon, many more heavier versions of the proton and neutron were discovered, together with their anti-particles, which were interacting through the strong interaction (mesons and baryons). This proliferation of particles pointed the way to a substructure of these particles, culminating in the quark model proposed by Gell-Mann and Zweig in 1964, who originally proposed 3 quarks. Hitherto, 6 different kinds of quarks have been discovered, the most recent the bottom quark in 1977 [23] and the top quark in 1995 [16, 22]. Heavier versions of the electron were found as well: the μ in 1937 and the τ in 1976. The neutrino, already predicted by Pauli at the start of the last century, was found in 1956 by Cowan and Reines. To understand how all these particles interacted, theoretical frameworks were needed and developed: the electromagnetic interaction, carried by photons, the weak interaction, carried by the W^\pm and Z^0 bosons (which were discovered in 1983 at CERN by UA1),

and the strong interaction, carried by gluons. In 1967, Weinberg and Salam unified the weak and the electromagnetic interaction into the electroweak interaction, requiring the existence of a Higgs boson.

All these interactions together are now known as the Standard Model. The Standard Model has proven to be a very precise explanation of what happens around us. Many tests of the Standard Model have been executed and so far none has proven beyond doubt that the Standard Model is incorrect. However, mysteries still remain. The most feeble force in nature, gravity, cannot be accommodated in the current standard model, without extensions such as super symmetry. Another curious fact is the high mass of the top quark, when compared with the other quarks. Also, the existence of the Higgs boson, the last building block of the Standard Model, has yet to be proven, even though the LEP experiments at CERN found tantalizing hints for the existence of a Higgs boson with a mass of $115 \text{ GeV}/c^2$. Other measurements have hinted at something more beyond the Standard Model, such as the $g-2$ experiment that measured the magnetic moment of the muon to be 3σ away from the value predicted by the Standard Model, or the measurement of SNO that neutrinos have a mass while the Standard Model predicts these particles to be massless. Another interesting probe for the Standard Model is the b -quark production cross section, measured first by UA1, which was a factor 2–3 too high when compared with theory. Consequent measurements by CDF and DØ in Run I were also on the high side, but could not prove a significant excess. In Run II, with an upgraded accelerator that provides 10 times more luminosity and a 10% higher energy, together with an upgraded detector, this measurement can be done with more precision, testing the Standard Model.

This thesis describes a measurement of the b -quark production cross section at a center of mass energy of 1.96 TeV, using a muon tag to identify jets containing a b -quark. This is done using the DØ detector, based at the Tevatron $\bar{p}p$ collider. Chapter 2 describes the Standard Model, and gives an overview of the theoretical prediction by the Standard Model of the b -quark production cross section. Chapter 3 describes the apparatus used, with a special emphasis on the muon system. All three levels of the trigger system, crucial for a hadron collider such as the Tevatron, are handled in Chapter 4. Offline reconstruction of selected events is described in Chapter 5, while Chapter 6 deals with the selection of those events used in the analysis. In Chapter 7 the $\mu + \text{jet}$ cross section is calculated, of which the b -jet content is extracted in Chapter 8, where ultimately the b -jet cross section is calculated. Chapter 9 then concludes this thesis by confronting this measurement with the prediction of the Standard Model.

Chapter 2

The Standard Model

The Standard Model is currently the best theory describing subnuclear matter and its interactions. It encompasses the electromagnetic and weak forces, unified in the electroweak theory, QED, and the strong force described by the theory of quantum chromodynamics, QCD. The model is a Quantum Field theory based on the perception of local gauge invariance. For the Standard Model, the gauge symmetry group is $SU(3)_C \times SU(2)_L \times U(1)_Y$, where $SU(3)_C$ is the symmetry group describing the strong interaction and $SU(2)_L \times SU(1)_Y$ the symmetry group describing the electroweak interaction. The theory describes two general classes of particles: spin- $\frac{1}{2}$ particles known as fermions and spin-1 gauge vector particles known as bosons. The fermions can be subdivided in leptons and quarks, each of which can be grouped into three families with two members for a total of 6 leptons and 6 quarks. The properties of the leptons and quarks are summarized in tables 2.1 and 2.2. The vector gauge bosons that mediate the forces between these particles are required by the local gauge invariance to be massless. The bosons that carry the electroweak force - namely, two charged particles, W^+ and W^- and one neutral particle Z^0 - acquire a non-zero mass by spontaneously symmetry breaking of the $SU(2)_L \times SU(1)_Y$ symmetry group, which is implemented through the Higgs mechanism. Even though the former bosons have been discovered, the Higgs boson itself has eluded detection so far.

The quarks interact via the gauge bosons of the $SU(3)_C$ group, called gluons. There are eight gluons in total, which are allowed to interact with themselves due to the non-abelian nature of the $SU(3)_C$ group. The observed strongly interacting particles in nature are called hadrons, which can be classified into mesons ($q\bar{q}$ pairs) and baryons (qqq , or in the case of anti-baryons, $\bar{q}\bar{q}\bar{q}$). No free quarks have been observed up to now, which leads to the theory that particles in nature have an extra internal degree of freedom, namely color, and have to consist of either a colored and an anti-colored particle, or three different colored particles. Thus, only color singlets exist in nature and no bare color states can exist. The strength of the strong interaction is specified

Lepton	Mass (MeV/ c^2)	Charge
Electron (e)	0.511	-1
Electron Neutrino (ν_e)	0	0
Muon (μ)	105.7	-1
Muon Neutrino (ν_μ)	0	0
Tau (τ)	1784	-1
Tau Neutrino (ν_τ)	0	0

Table 2.1: *Lepton properties*

Quark	Mass (GeV/ c^2)	Charge
Down (d)	0.005–0.015	$-\frac{1}{3}$
Up (u)	0.002–0.008	$\frac{2}{3}$
Strange (s)	0.1–1.7	$-\frac{1}{3}$
Charm (c)	1.3–1.7	$\frac{2}{3}$
Bottom (b)	4.7–5.3	$-\frac{1}{3}$
Top (t)	166–184	$\frac{2}{3}$

Table 2.2: *Quark properties*

by the strong coupling constant α_s . This constant decreases with increasing Q^2 , the four-momentum transfer in the collision. Cross sections in QCD can be approximated by expansions in α_s , but cannot be calculated exactly. If α_s is sufficiently small, which is the case for Q^2 higher than a few GeV, these expansions converge, and the cross sections predicted by QCD can be calculated reliably (so called asymptotic freedom). For smaller Q^2 values, these cross sections cannot be calculated as reliable. At the center of mass energy at the Tevatron, $\sqrt{s} = 1.98$ TeV, the cross section for high Q^2 processes are large enough to allow precise measurements of the QCD predictions, especially for the production of bottom and charm quarks.

2.1 Asymptotic Freedom

In QCD the leading order quark production process, as is shown in figure 2.1, is modified by higher order loop diagrams in which the loops consist of quarks or gluons (figure 2.2). The effect of these loops causes the bare color charge of the quark to be screened, which affects the coupling α_s of other quarks and gluons to the bare color charge:

$$\alpha_s(|q^2|) = \frac{\alpha_s(\mu^2)}{1 + (\alpha_s(\mu^2)/12\pi)(11n - 2f) \ln(|q^2|/\mu^2)} \quad (|q^2| \gg \mu^2) \quad (2.1)$$

Here, n is the number of colors, and f is the number of flavors. Since in the Standard Model $n = 3$ and $f = 6$, $11n - 2f$ is positive, and the loops consequently have an anti-screening effect on the bare color charge: with increasing $|q^2|$, the effective coupling decreases. This is called “asymptotic freedom”. When $|q^2|$ gets large, the quarks and gluons decouple and behave like free particles.

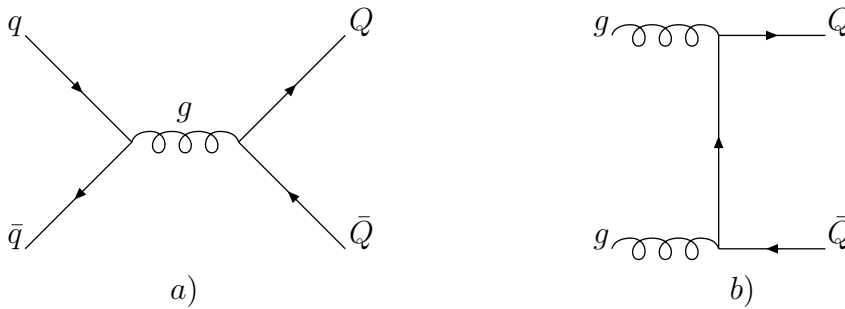


Figure 2.1: *Leading order heavy quark production.*

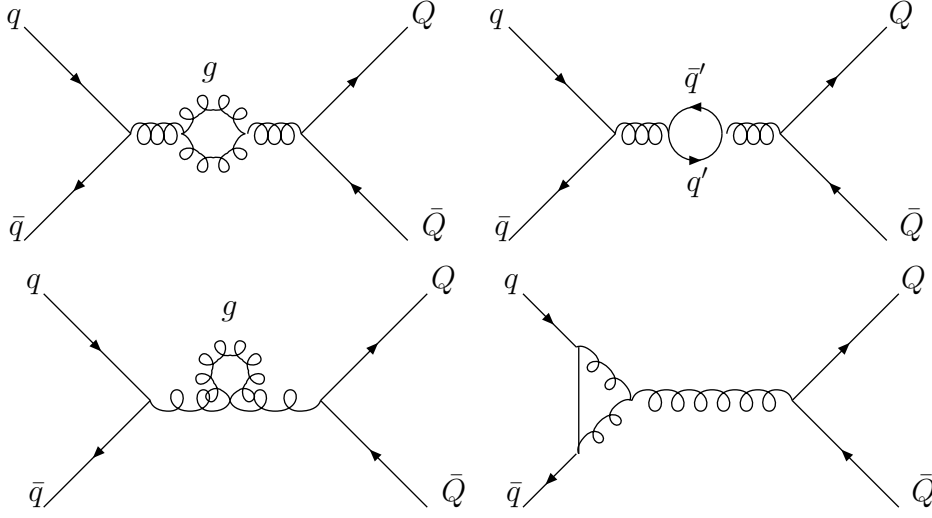


Figure 2.2: Higher order diagrams for heavy quark production with loops in the gluon propator.

The parameter μ in equation 2.1 is a cut-off parameters in the theory. This parameter is needed because the perturbation theory on which QCD is based breaks down at $|q^2| = 0$, where α_s becomes large (> 1). Therefore, we need to reference some point μ where α_s is small enough to justify the perturbation expansion. In the regime where $\alpha_s(\mu^2) < 1$ we can introduce a new variable, Λ , which is defined by:

$$\ln \Lambda^2 = \ln \mu^2 - 12\pi / ((11n - 2f)\alpha_s(\mu^2)) \quad (2.2)$$

With this variable, $\alpha_s(\mu^2)$ can be written as:

$$\alpha_s(|q^2|) = \frac{12\pi}{(11n - 2f) \ln(|q^2|/\Lambda^2)} \quad (|q^2| \gg \mu^2) \quad (2.3)$$

This allows us to express the running coupling constant $\alpha_s(\mu^2)$ in terms on only one constant, Λ . Experimentally, this variable has been measured to have a value between 100 and 250 MeV.

2.2 Heavy quark production

In the regime of asymptotic freedom, we can decompose the proton-antiproton interaction into a parton-parton interaction. The cross section for a certain interaction can be written as:

$$\sigma = \sum_{ij} \int dx_i dx_j \hat{\sigma}_{ij}(x_i p_A, x_j p_B, \mu, \Lambda) F_i^A(x_i, \mu) F_j^B(x_j, \mu) \quad (2.4)$$

where $\hat{\sigma}_{ij}$ is the parton level cross section between the partons in each hadron, x_i and x_j are the fractions of the proton momentum p_A and anti-proton momentum p_B that the partons i and j carry. F_i^A and F_j^B are the structure functions describing the density of the partons inside the proton and anti-proton. The parton level cross sections $\hat{\sigma}_{ij}$ depend on the two scale parameters, μ and Λ . In heavy quark production, μ is normally chosen to be a function of p_T^Q , the transverse momentum of the heavy quark, and m_b , the mass of the quark. Due to the fact that quarks are only observed in mesons and hadrons, it is not possible to measure the mass of these quarks directly (hence the errors on the quark masses in table 2.2). Experimentally, the mass of the bottom quark is determined to be $m_b = 4.74 \pm 0.14 \text{ GeV}/c^2$.

In QCD, the cross section of b -quark production in the regime of asymptotic freedom can be written as an expansion in α_s :

$$\hat{\sigma}_{ij} = \alpha_s^2(\mu) G_{ij}^{LO}(\hat{s}, m_Q) + \alpha_s^3(\mu) G_{ij}^{NLO}(\hat{s}, m_Q) + \dots \quad (2.5)$$

where G^{LO} and G^{NLO} are dependent on the quark mass m_b and the center of mass energy \hat{s} . The total cross section for b -quark production results from the sum of all contributing processes. The Feynmann diagrams for the leading order processes are shown in figure 2.1. The experimental signature for such an event is two jets in the detector, with a transverse energy balance. Next to leading order Feynmann diagrams are shown in figure 2.3. These processes have three partons in the final state, and are either radiative corrections to the leading order processes (where we have two quarks or two gluons in the initial state), or a new class of processes in which a quark and a gluon are in the initial state.

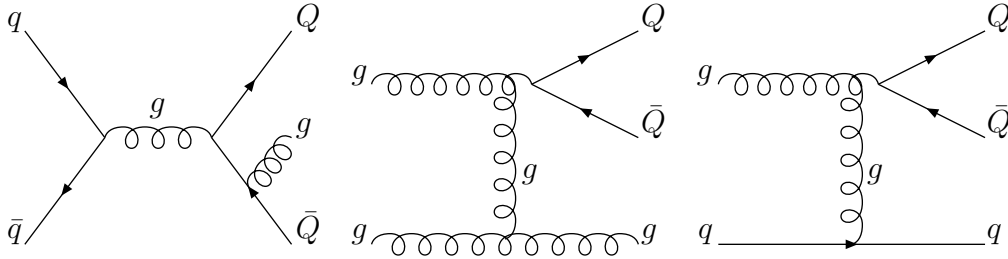


Figure 2.3: Next to leading order heavy quark production.

In the following, we will study the production of b -jets instead of the production of b -quarks. The main difference between these studies is that in the case of production of b -quarks, one is interested in the properties of the heavy quark itself, regardless of the event structure in which the b -quark is produced, while for a jet one is interested in

the energy of the jet that contains one or more heavy quarks, and not in the fraction of the energy carries by these quarks. Calculating the properties of the quark brings with it the difficulty of the emission of collinear gluons, which at high momentum cause large logarithms to appear. These logarithms need to be resummed, using for example fragmentation functions. In the calculation of jet properties, these logarithms do not appear, since the jet contains both the quarks and the collinear gluons. The experimental measurement of e.g. the E_T^{jet} distribution therefore does not depend on the knowledge of the fragmentation functions, contrary to the p_T distribution of b -quarks.

To calculate the cross sections for b -jet producing processes in this analysis, we use a next to leading order Monte Carlo calculation written by Mangano, Nason and Ridolfi [28]. This calculation provides the 4-momenta of the b -quark, \bar{b} -quark and a possible gluon, with the appropriate event weight. Our goal is now to measure the production rate for b -quark jets. In general, the definition of a jet can be freely chosen, except for the fact that it must be infrared safe. In this analysis, we adopt the Snowmass convention, where the particles are clustered in $\eta - \phi$ space in a cone of radius R , with $R = 0.5$ throughout the analysis. We only consider jets that contain a b or \bar{b} -quark, or both; the gluon jet is disregarded if the gluon does not end up in the same jet with a heavy quark.

We calculate the cross section for heavy quark jets with $|\eta_{jet}| < 0.6$, to reflect a realistic geometrical acceptance of the DØ detector, during the start of Run II. The factorization scale μ_F and renormalization scale μ_R are chosen as:

$$\mu_F^2 = \mu_R^2 = \mu_0^2 = \frac{(p_T^b)^2 + (p_T^{\bar{b}})^2}{2} + m_b^2 \quad (2.6)$$

and we vary these scales between $\mu_0/2$ and $2\mu_0$ to account for theoretical uncertainties. The parton distribution function adopted is CTEQ6M [21]. For the b -quark mass, we use 4.8 ± 0.2 GeV, with the errors reflecting the uncertainty on the mass measurement. This results in the total b -jet cross section as a function of E_T^{jet} , shown in figure 2.4. The dotted lines show the error resulting from floating μ_F and μ_R , and varying the b -quark mass.

Figure 2.5 shows the theoretical cross section subdivided in the contributions of the different initial states. At high E_T^{jet} , the gluon splitting processes become dominant. Quark fusion of valence quarks only becomes dominant at much higher E_T^{jet} , which is not visible in the figure.

The contribution of gluon splitting is demonstrated in figure 2.6, which shows the cross section of jets containing only one b -quark (or \bar{b} -quark) and those containing both a b - and a \bar{b} -quark. Here as well the relative contribution of $b\bar{b}$ -jets increases with higher E_T^{jet} .

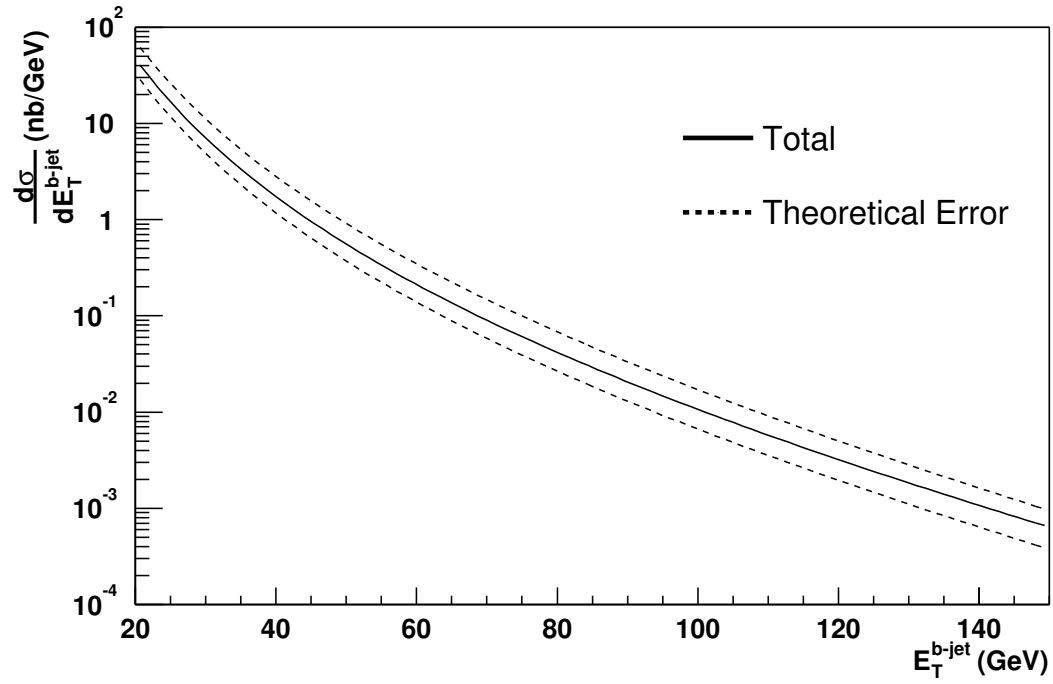


Figure 2.4: Theoretical b -jet production cross section with the theoretical errors resulting from floating μ_F and μ_R , as well as the b -quark mass.

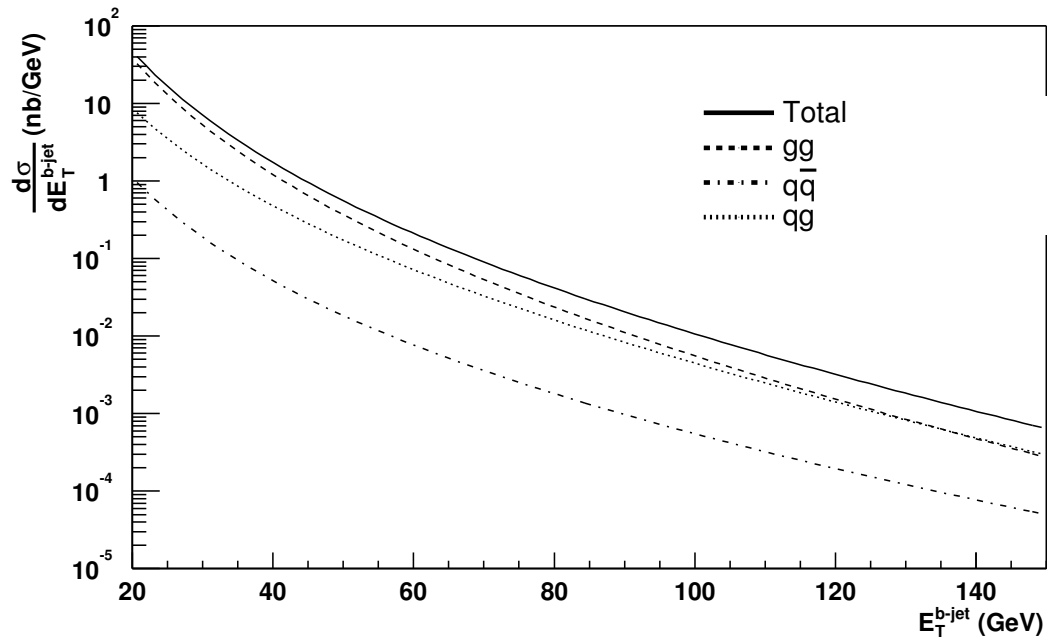


Figure 2.5: Theoretical b -jet production cross section, separated in the contributions of the different initial states.

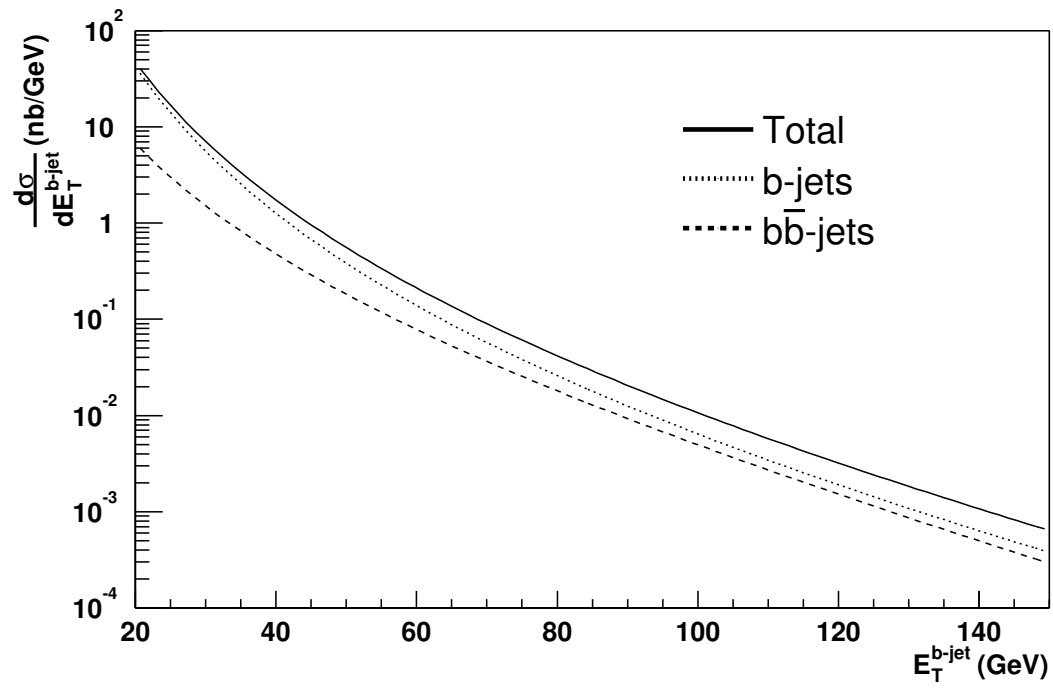


Figure 2.6: Theoretical b -jet production cross section, separated in the contributions of jets with one b - or \bar{b} -quark present, or with both a b - and a \bar{b} -quark present.

Chapter 3

The Apparatus

The DØ experiment was originally designed to study $\bar{p}p$ collisions at a center of mass energy of 1.8 TeV at the Fermilab Tevatron Collider. During Run I, from July 1990 until August 1995, the Tevatron delivered 125 pb^{-1} of integrated luminosity, which allowed a wide range of high mass and high p_T physics phenomena to be investigated. During a shutdown period from 1995 until 2001 the Tevatron was upgraded to run with a luminosity increased by one order of magnitude, at a center of mass energy of 1.96 TeV. In this period, the DØ detector was upgraded to handle the increased luminosity at this new high-energy frontier.

3.1 The Tevatron

The Tevatron is a $\bar{p}p$ collider that accelerates both the protons and anti-protons to an energy of 980 GeV, providing the center of mass energy of 1.96 TeV. Until the Large Hadron Collider at CERN starts in 2007, the Tevatron will be the highest energy collider in the world.

As is the case in all current day high-energy accelerators, the Tevatron is only the last accelerator in a long chain of accelerators, as is illustrated in figure 3.1. The proton beam originates from the pre-accelerator, where negatively charged hydrogen ions are accelerated to 750 keV in a Cockroft-Walton accelerator. From there, the hydrogen ions are bunched and led into a 150 meter long linear accelerator (LINAC), which accelerates the ions to an energy of 400 MeV, after which the ions are led through a carbon foil. This foil strips both electrons from the hydrogen nucleus, leaving the proton. The protons are then fed into a circular accelerator, called the booster, in which they are accelerated to an energy of 8 GeV. After this stage, they enter the Main Injector. This circular accelerator serves two purposes: it accelerates protons and anti-protons from 8 GeV to 150 GeV for insertion in the Tevatron, and it accelerates protons from 8 GeV to 120 GeV for the production of anti-protons. The anti-protons are produced by colliding

the protons that have been accelerated in the Main Injector to an energy of 120 GeV on a nickel target. These collisions produce many secondary particles, among which are anti-protons, approximately one for every 10^5 protons. The anti-protons produced are temporarily stored in a circular ring, called the Accumulator. When approximately 10^{11} anti-protons have been produced, they are assembled, bunched and inserted in the Main Injector to be accelerated to an energy of 150 GeV for injection in the Tevatron. The tunnel of the Main Injector also holds the Antiproton Recycler, which decelerates anti-protons coming from the previous run in the Tevatron and stores them for future use. After acceleration of the protons and anti-protons in the Main Injector to an energy of 150 GeV, both beams are inserted in the Tevatron, where they are further accelerated to an energy of 980 GeV.

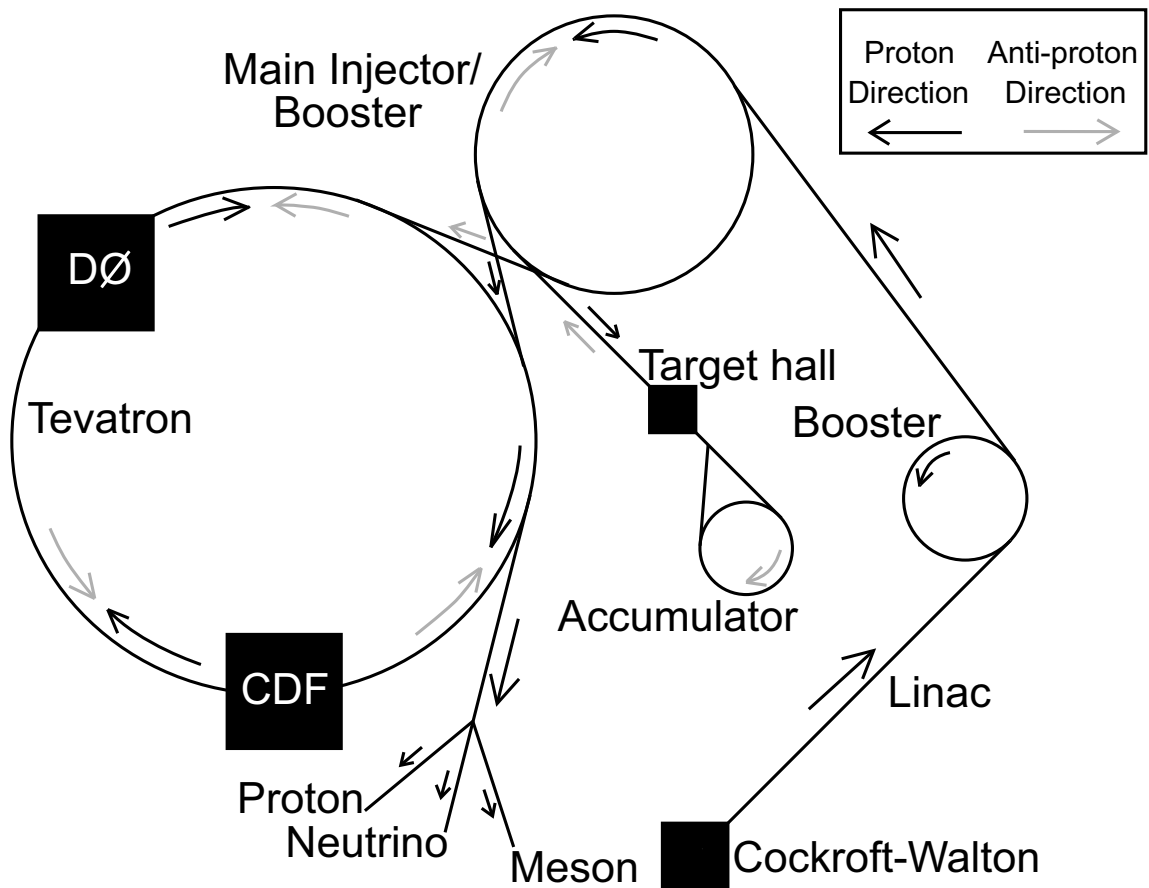


Figure 3.1: *The Fermilab accelerator chain, showing the DØ collider region and the fixed target lines.*

The Tevatron uses superconducting magnets with a field strength of 4.2 Tesla (at a beam energy of 980 GeV) to bend the protons and anti-protons through the 1000-meter

Parameter	Run IIa beam parameter
Energy	980 GeV
Protons / bunch	27×10^{10}
Antiprotons / bunch	7.5×10^{10}
Bunches	36
Antiproton stacking	20×10^{10} /hour
Luminosity	$2.1 \times 10^{32} \text{ cm}^{-2}\text{s}^{-1}$
Bunch spacing	396 ns
Interactions per crossing	5.8

Table 3.1: *Beam parameters for the Tevatron Run IIa.*

radius tunnel. The proton beam traverses the Tevatron clockwise, with the anti-proton beam moving in the opposite direction. The beams meet at the two interaction points, at BØ, where the CDF detector is located, and at DØ, where the DØ detector is located. The longitudinal position of the interaction point has a Gaussian shaped distribution around the center of the DØ detector with a width of approximately 25 cm. In the transverse plane the position distribution also has a Gaussian shape but with a width of 30 μm . Some parameters for the Tevatron for Run IIa are given in table 3.1.

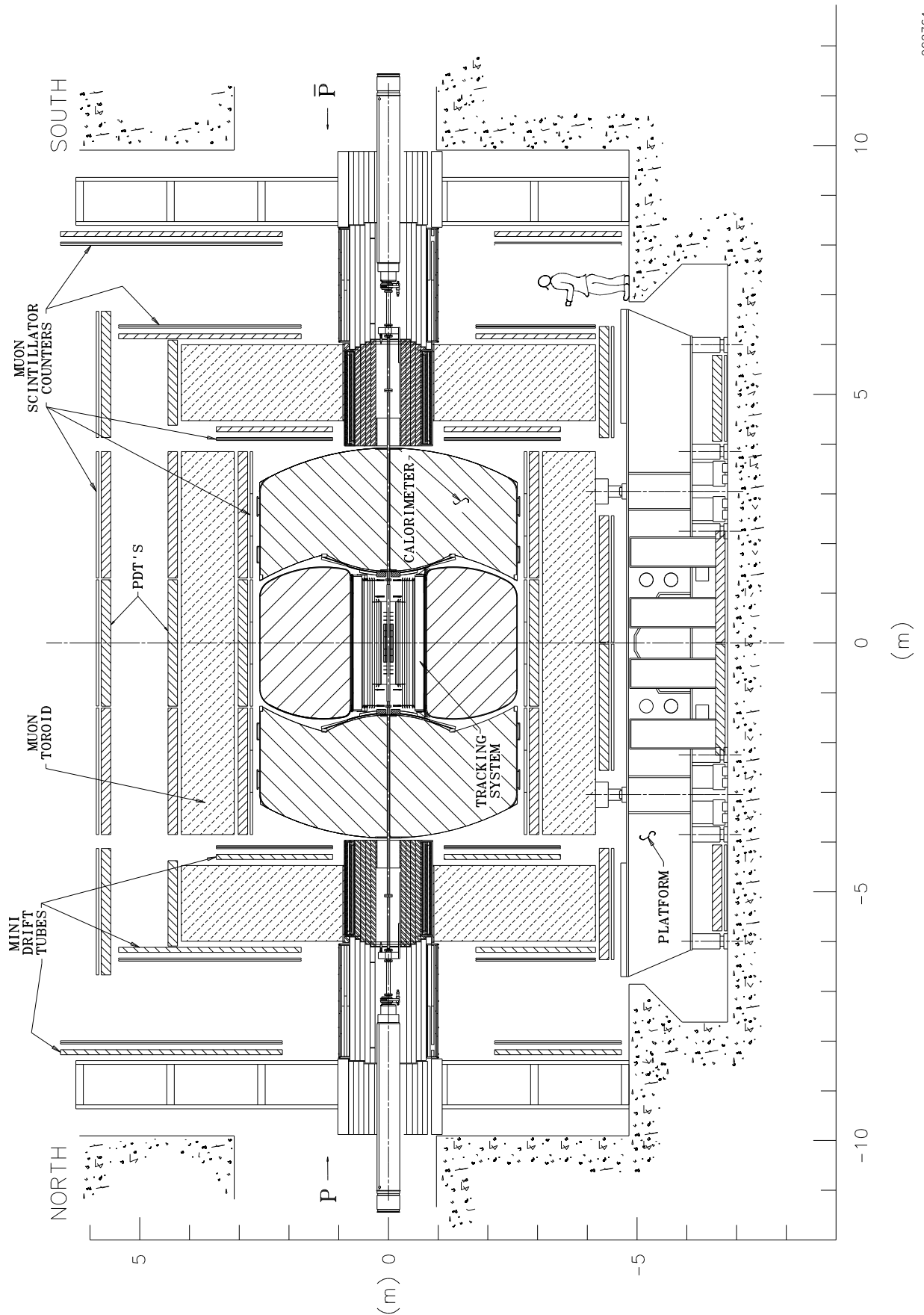
These parameters have changed significantly from the previous run, Run I, to maximize the physics output of Run II. Most notably, the luminosity is increased tenfold to $2.1 \times 10^{32} \text{ cm}^{-2}\text{s}^{-1}$ by:

- Increasing the number of bunches from 6 to 36, while simultaneously lowering the bunch crossing time from 3.6 μs to 396 ns;
- Increasing the number of protons and anti-protons per bunch, using the Main Injector and the Recycler;

3.2 The DØ Detector

The DØ detector design was optimized for efficient identification of leptons and jets over a wide rapidity region. This was achieved by using finely segmented, hermetic electromagnetic and hadronic calorimetry, muon detection using magnetized iron, and non-magnetic inner tracking. The data collected in Run I has allowed the DØ collaboration to study a multitude of interesting physics topics, resulting in 118 publications. Most notably is the discovery of the top quark in 1995 [22]. For Run II, the

DØ upgrade has extended the capability of the detector to include track momentum determination and vertexing, while maintaining an angular coverage to $|\eta| \approx 3$, where $\eta = -\ln(\tan \theta/2)$ and θ is the angle with respect to the beam.

Figure 3.2: *Elevated view of the DØ detector.*

3.2.1 Inner Tracker

The inner tracker consists of two major subsystems: a high precision silicon microstrip tracker, and a scintillating fiber tracker, which provides a trigger. The entire inner tracker is encased in a 2.7 meter long superconducting solenoidal magnet, which provides a field of 2 Tesla.

Silicon Tracker

The silicon tracker consists of silicon disks and barrels formed into 6 disk/barrel modules [9]. Each barrel module consists of 4 (radial) layers of detector ladder assemblies. The outer barrel on each side has single sided silicon in layers one and three with a pitch size of $50\ \mu\text{m}$, while the inner four barrels have double sided silicon in these two layers, with a 90° stereo angle and a pitch size of $50\ \mu\text{m}$ on the p-side and $156\ \mu\text{m}$ pitch on the n-side. Layers two and four are double sided with a 2° stereo angle in all barrels, and a pitch size of $50\ \mu\text{m}$ on the p-side and $62.5\ \mu\text{m}$ on the n-side. Each disk module has 12 wedge shaped double-sided detectors with an effective 30° stereo angle. The readout strips run parallel to one edge of the wedge, at an angle of 15° with respect to the symmetry axis of the wedge. Thus, the readout strips on each side have an effective 30° stereo angle. Three sets of end disks, named F-disks, are placed on each end side of the detector. The detectors in these disks have a pitch size of $52\ \mu\text{m}$ on the p-side and $65\ \mu\text{m}$ on the n-side. Further along the beam pipe, on each side of the detector, are two bigger disks (called H-disks) of single sided silicon wedges with a pitch size of $81\ \mu\text{m}$, used for forward tracking. This detector setup allows a measurement of single hit positions with a resolution of approximately $10\ \mu\text{m}$. The complete detector consists of approximately $8 \cdot 10^5$ channels.

Silicon detector element	Pitch (μm)
Axial strips	50
2° stereo strips, n-side	62.5
90° stereo strips, n-side	156
F-disks, p-side	52
F-disks, n-side	65
H-disks	81

Table 3.2: *Pitch size for each silicon detector element.*

Central Fiber Tracker

The Central Fiber Tracker consists of scintillating fibers mounted on eight concentric cylinders [32]. The fibers are double clad and are $835\ \mu\text{m}$ in diameter. The fibers are constructed in ribbons each 128 fibers wide composed of two 'singlet' layers. These singlet layers are formed into the 'doublet' layers, which form the ribbon by placing the fiber centers of one of the singlet layers in the space between the fibers of the other singlet layer. The tracker consists of eight of these doublet layers with the fibers aligned along the beam axis. An additional doublet layer with a 3° u- or v-type stereo angle¹ is mounted on each axial doublet layer, with the stereo angles alternating with each consecutive doublet layer. The detector is divided into 80 sectors in ϕ , where ϕ is the azimuthal angle. Each pie shaped slice has 896 fibers and the entire detector has

¹A u-v geometry has one layer of active material aligned along $+\alpha$ from the symmetry axis, and another layer aligned along $-\alpha$ from the symmetry axis, where α is the stereo angle.

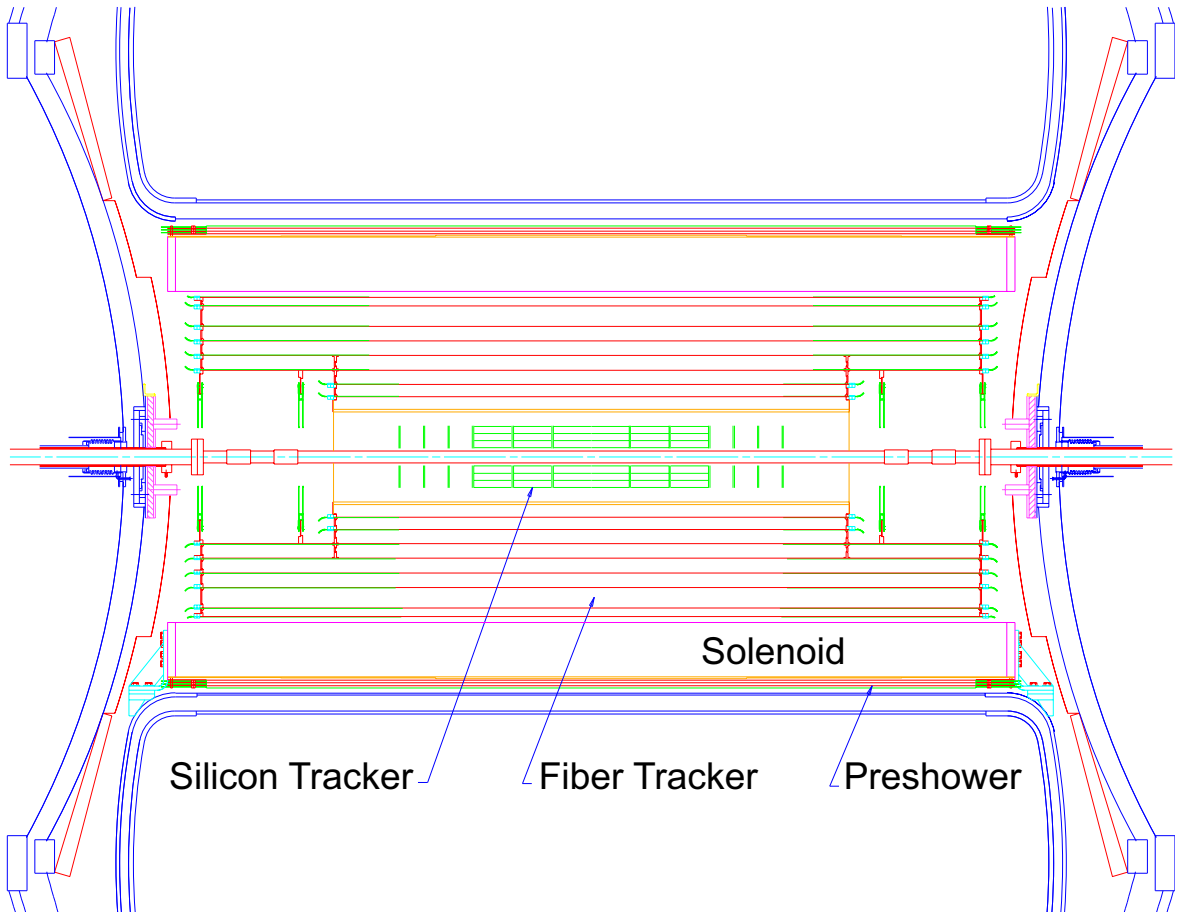


Figure 3.3: *Schematic view of the inner tracker.*

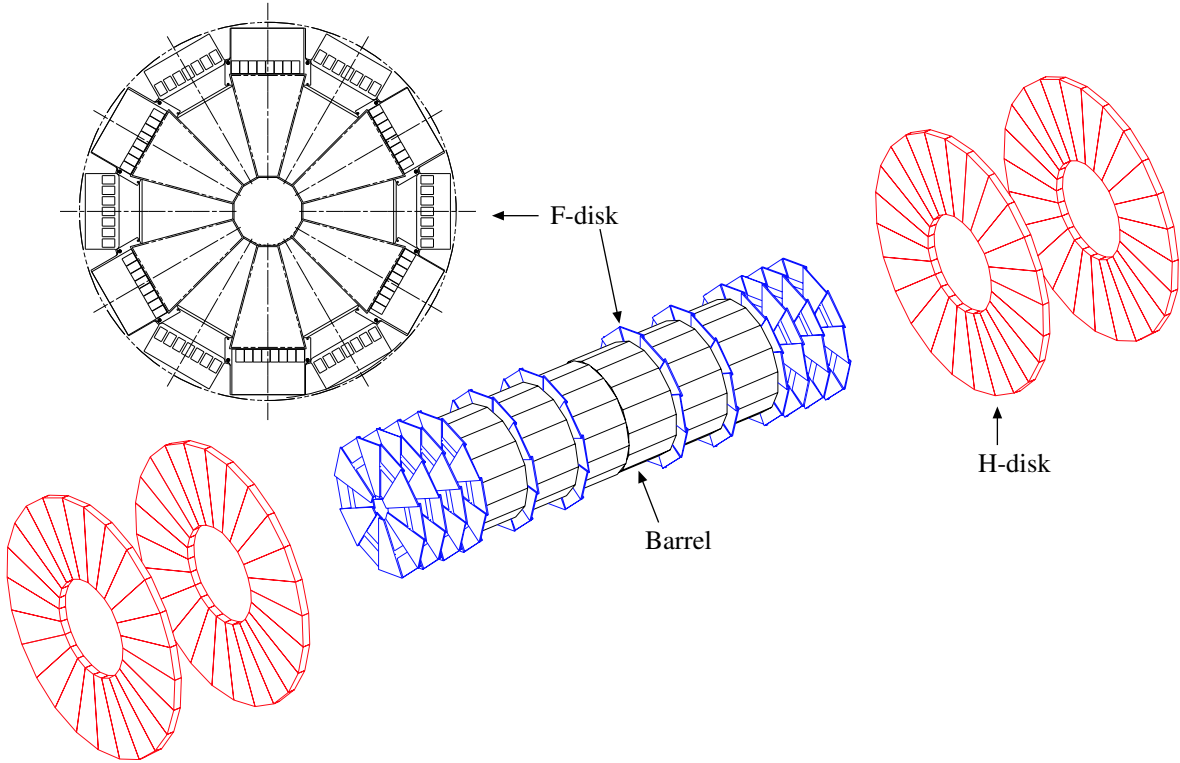


Figure 3.4: *Schematic view of the silicon tracker, showing the 6 barrels, 12 F-disks and 4 H-disks.*

71,680 channels. The light from the fibers is converted into electrical pulses by visible light photon counters, VLPC's.

The entire inner tracker is encased in a The resolution with which the inner tracker can measure the transverse momentum of particles is shown in figure 3.5.

3.2.2 Calorimeter

The DØ calorimeter is a sampling calorimeter using depleted uranium, lead and copper as absorber materials, and liquid argon as sampling material. It consists of three cryostats: the Center Calorimeter (CC), which covers the area $|\eta| < 1$, and the two Endcap Calorimeters (EC), which extend the covered area up to $|\eta| \approx 4$. In addition, preshowers are placed in front of the calorimeters in the central and forward regions.

Central and endcap calorimeters

Each of the calorimeters is split up in three sections: an electromagnetic section (EM) of approximately 20 radiation lengths, closest to the beam pipe, with relatively thin

uranium absorber plates, followed by a fine hadronic section further out, using thick uranium plates as absorber. The outer part of the calorimeter is made up of the coarse hadronic section, using thick copper or stainless steel plates as absorber material. The hadronic section has a thickness of around 6 interaction lengths in the central calorimeter, and around 9 interaction lengths in the forward calorimeter. The calorimeter is pseudo-projective, meaning that the towers in the calorimeter are pointing to the interaction point, but that the cells that the towers are made of are not projective. The cells in the central region have a typical size of $\Delta\eta \times \Delta\phi = 0.1 \times 0.1$; exceptions to this are the cells in the third layer or the EM section, where $\Delta\eta \times \Delta\phi = 0.05 \times 0.05$. This is the area in which electromagnetic showers deposit most of their energy, and a higher segmentation is desired for better resolution of the direction of electrons and photons. In the very forward region with $3.2 < |\eta| < 4.0$, where the physical size of the cells would become tiny, the cells have a size of 0.2×0.2 in (η, ϕ) . The energy resolution of the calorimeter as it has been reached in Run I is $\Delta_E/E = 15\%/\sqrt{E} \oplus 0.4\%$ for electrons and photons (with E in GeV). For charged pions and jets, these resolutions are $50\%/\sqrt{E}$ and $80\%/\sqrt{E}$ respectively.

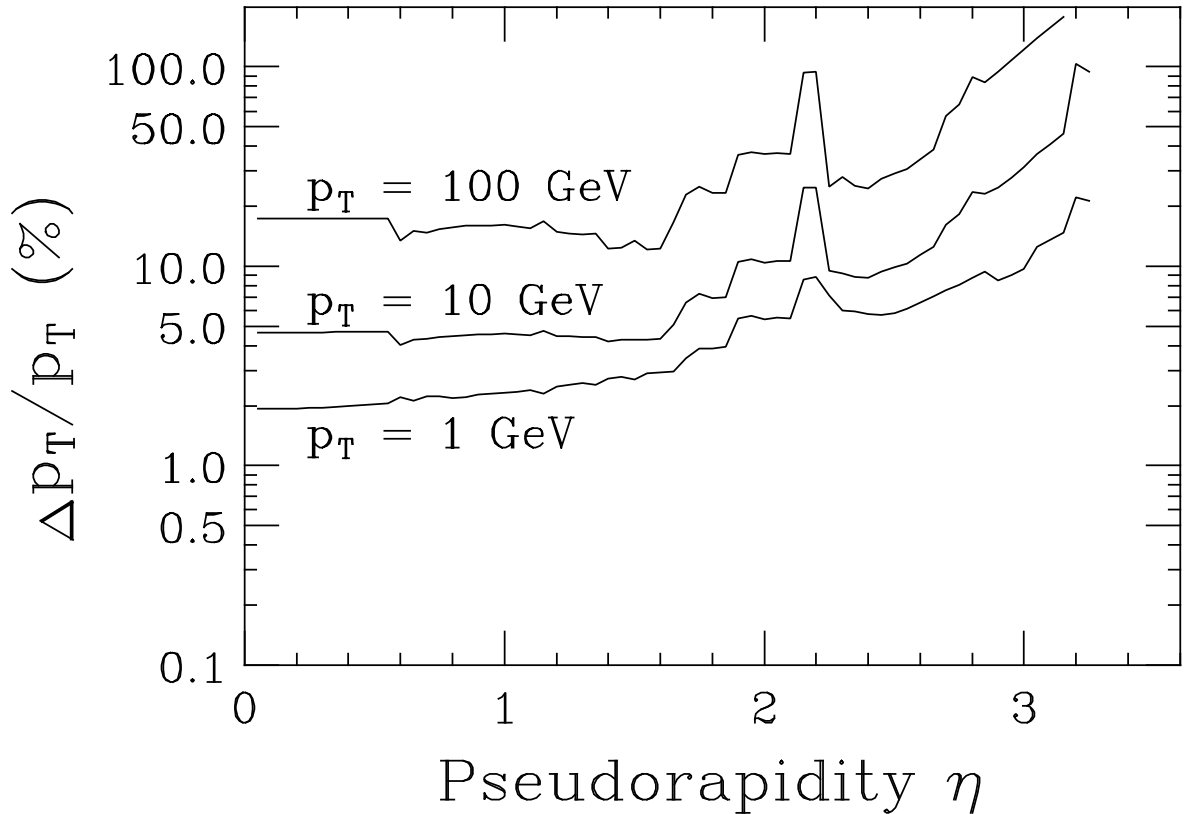


Figure 3.5: Measurement of $\frac{\Delta p_T}{p_T}$ by the inner tracker as a function of η .

To augment the energy measurement in the intercryostat space between the central and forward calorimeters, intercryostat detectors (ICD's) are placed in this region (see figure 3.6). They consist of an annular ring of 1.25 cm thick scintillating material, segmented in 16 pieces and covering $1.1 < |\eta| < 1.4$. The 16 pieces are further divided in parts of $\Delta\eta \times \Delta\phi = 0.1 \times 0.1$ which are read out by photomultipliers through embedded wavelength shifting fibers that collect and transport the light.

Preshowers

The preshowers consist of two systems: a central system covering $|\eta| < 1.3$ (CPS), and a forward system covering $1.5 < |\eta| < 2.5$ (FPS) (shown in figure 3.6). Both are designed to improve the electron identification efficiency. The central system consists of a lead radiator of 2 radiation lengths thickness at $\eta = 0$, followed by three layers of scintillating material arranged in an axial u-v geometry with a 22.5° stereo angle. Electrons are recognized based on the fact that muons and charged pions traversing the radiator will only deposit energy due to ionization, while electromagnetic particles will shower in the radiator.

The forward preshower also consists of a lead radiator with a thickness of 2 radiation lengths [13], sandwiched between two layers of scintillating material. Each layer is made from 2 thinner layers of scintillating fibers, arranged in an axial u-v geometry with a 22.5° stereo angle. When a charged particle traverses the layer before the radiator, its position can be measured with the scintillating fibers. Whereas a muon and a charged pion will not shower in the radiator, and only deposit the equivalent of 1 MIP² in the layer behind the lead, photons and electrons will create a shower and deposit most of their energy in the layer behind the lead. A photon will not deposit energy in the first layer of fibers, thus allowing a separation of electrons and photons.

In both systems, light collected by the scintillating fibers is transported by embedded wavelength-shifting fibers, and read out by visible light photon counters.

3.2.3 Muon Detector

The muon detector consists of three major parts, as is shown in figure 3.2:

- The Wide Angle Muon Spectrometer (WAMUS), covering $|\eta| < 1$;
- The Forward Angle Muon Spectrometer (FAMUS), covering $1 < |\eta| < 2$;
- A solid-iron magnet creating a toroidal field of 1.8 Tesla.

²A minimum ionizing particle (MIP) deposits a few MeV/cm in the material it passes through due to ionization.

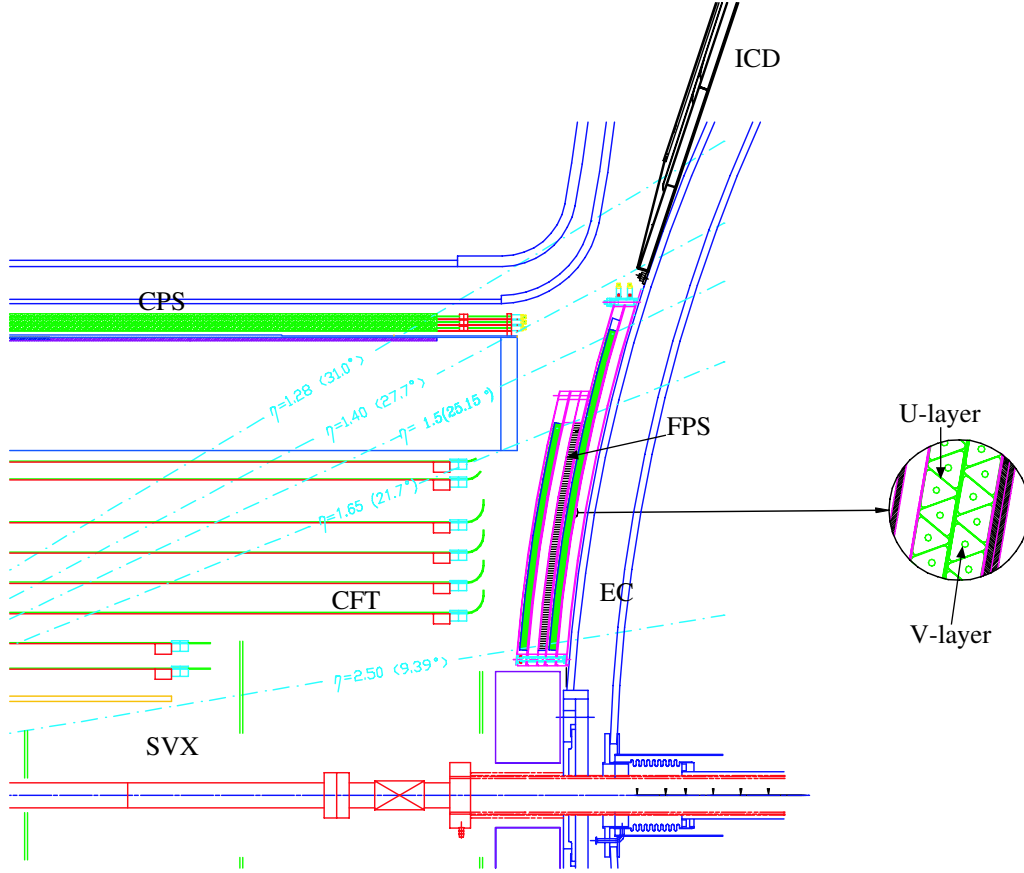


Figure 3.6: View of the forward preshower, with an inset showing the geometry of the fiber system.

Toroid Magnet

The toroid magnet is a square iron annulus 109 cm thick, weighing 1973 tons. Running the coils of the magnet at 1500 Ampères, the magnet generates a magnetic field of 1.8 Tesla, with the field lines running in a plane perpendicular to the beam axis, vertically in the side parts of the magnet and horizontally in the top and bottom of the magnet. The iron of the central magnet also serves as the return yoke for the solenoid magnetic field. The magnet is split in a central system, covering the WAMUS region, and two forward systems, covering the FAMUS region.

WAMUS

The WAMUS consists of three detector systems: three layers of drift chambers with proportional drift tubes (PDT's), one inner layer of scintillators ($A - \phi$ counters) and outer layers of scintillator (Cosmic Cap) [24]. The three layers of proportional drift

tubes are arranged in a barrel geometry with one layer inside the toroid, normally called the A-layer, and two layers outside the toroid with one meter separation, called the B- and C-layer. Their purpose is to provide muon identification, and a momentum measurement independent of the central tracker. The chambers are constructed of extruded aluminum tubes and are of varying size, with the largest being approximately $250 \times 575 \text{ cm}^2$. The (B- and C-) layers outside the toroid each consist of 3 planes of tubes; the (A-) layer inside the toroid consists of 4 planes, with the exception of the A-layer bottom PDT's, which have 3 planes of tubes. The tubes are 10.1 cm across and 5 cm high, with around 24 tubes per chamber. The wires in each tube are oriented along the field lines of the magnetic field, in order to provide the position of the bend coordinate for the muon momentum measurement. Besides the anode wire, each tube also contains a vernier pad used as a cathode. This vernier pad consists of two metal strips that run along the length of the tube, of which the width follows a self-repeating see-saw pattern with a cycle of 60 cm. The relative amounts of the charge deposited on each of the strips indicate the position of the passing particle. The tubes are filled with a non-flammable gas mixture of 80% argon, 10% CH_4 and 10% CF_4 . When operated at a voltage of 2.5 kV for the pads, and 5.0 kV for the wires, the drift velocity in this gas is around $10 \text{ cm}/\mu\text{s}$, with a maximum drifttime of 600 ns. The uncertainty in the hit position due to diffusion in this gas is around $375 \mu\text{m}$. Each wire has a time readout with a resolution of 0.1 ns on one side, and is connected to a neighboring wire through a 20 ns delay jumper (see figure 3.7).

When a hit occurs on the wire, this setup enables the measurement of the drift time T_d , and the axial time T_a according to:

$$T_d = T_1 - T_2 \quad (3.1)$$

$$T_a = T_w + \frac{T_j + T_2 - T_1}{2} \quad (3.2)$$

where T_w is the time it takes the signal to propagate from the jumper to the time readout.

The resolution of the time measurement is dependent on the position along the wire of the hit. If the track passed the wire far from the electronics (near the jumper), the signal has to travel a maximum of one wire length, and the dispersion of the signal creates an effect that is equivalent to an axial resolution of 10 cm. If the track passes the wire close to the electronics, the signal to the neighboring wire has to travel two wire lengths, and the dispersion causes the axial resolution to degrade to 50 cm.

The $A - \phi$ counters are scintillators that cover the WAMUS PDT's in the A-layer between the calorimeter and the PDT tubes. They are segmented in ϕ -slices of 4.5° , and

have a length along the beam axis of about 85 cm. A photomultiplier tube, connected to the scintillator through multiple scintillating fibers, reads out the scintillators. The scintillators have a timing resolution of 4 ns and provide a fast signal for triggering on muons and for rejecting out-of-time cosmics and backscatter particles from the forward region.

The Cosmic Caps cover the top and sides of the muon detector, as well as part of the bottom, and are located outside the toroid. They are located outside the C-layer, and at the bottom also partly on the outside of the B-layer. Their purpose is to provide a fast signal to identify cosmic rays and, together with the $A - \phi$ counters, to give a timestamp on a muon to determine in which beam crossing the muon was produced. The time resolution of the scintillators is 5 ns, which can be improved by offline corrections to 2.5 ns. The relative momentum resolution with which the WAMUS system measures the tracks is shown in figure 3.10.

FAMUS

The FAMUS consists of three major systems: 3 layers of mini drift tubes (MDT's), 3 layers of scintillating material, also known as pixels, and shielding around the beam pipe to reduce trigger rates, fake track reconstruction and aging of the detectors [19].

The forward muon spectrometer is build from three layers of drift tubes, which have a position resolution in the drift plane of $\sigma_x \approx 0.7$ mm. The A layer, which is mounted on the inside face of the toroid, consists of 4 planes, while the B and C layers (mounted on the outside of the toroid, with one meter separation) consist of 3 planes. Each plane consists of tubes, each having 8 cells, and each plane is divided in 8 octants (see figure 3.11). The individual cells have an internal cross section of 9.4×9.4 mm², and have a 50 μ m tungsten-gold wire as the anode. The gas mixture in the cells is a mixture of 90% CF₄ and 10% CH₄, which at a voltage on the cathode of 3.1 kV gives a maximum drift time in the cells of around 60 ns, which is well within the 396

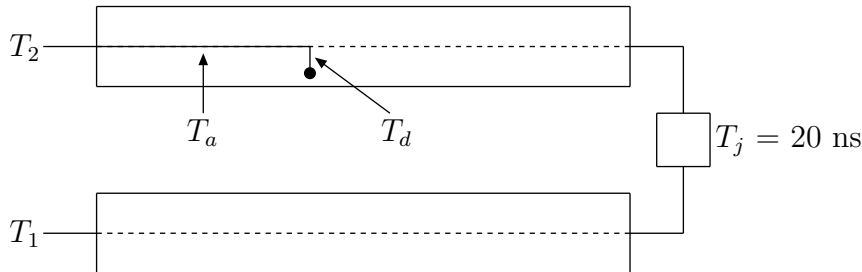


Figure 3.7: Schematic overview of the PDT readout system. The black dot represents a hit, which propagates to both time readouts T_1 and T_2 . This enables the calculation of the drift time T_d and the axial time T_a using the 20 ns delay jumper.

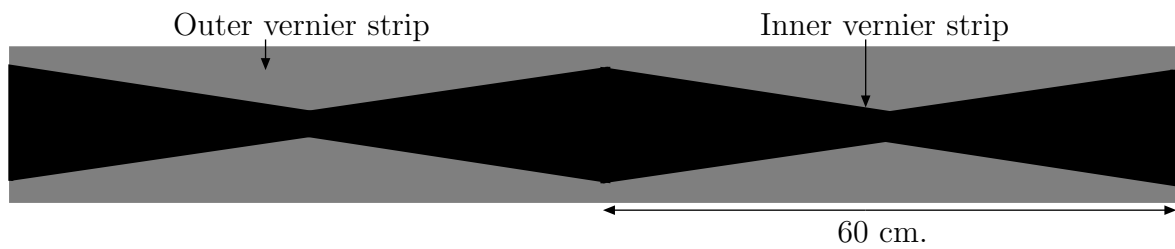


Figure 3.8: Schematic view of part of a vernier pad, showing two 60 cm. cycles. The black part represents the inner vernier strip, the gray represents the outer vernier strip.

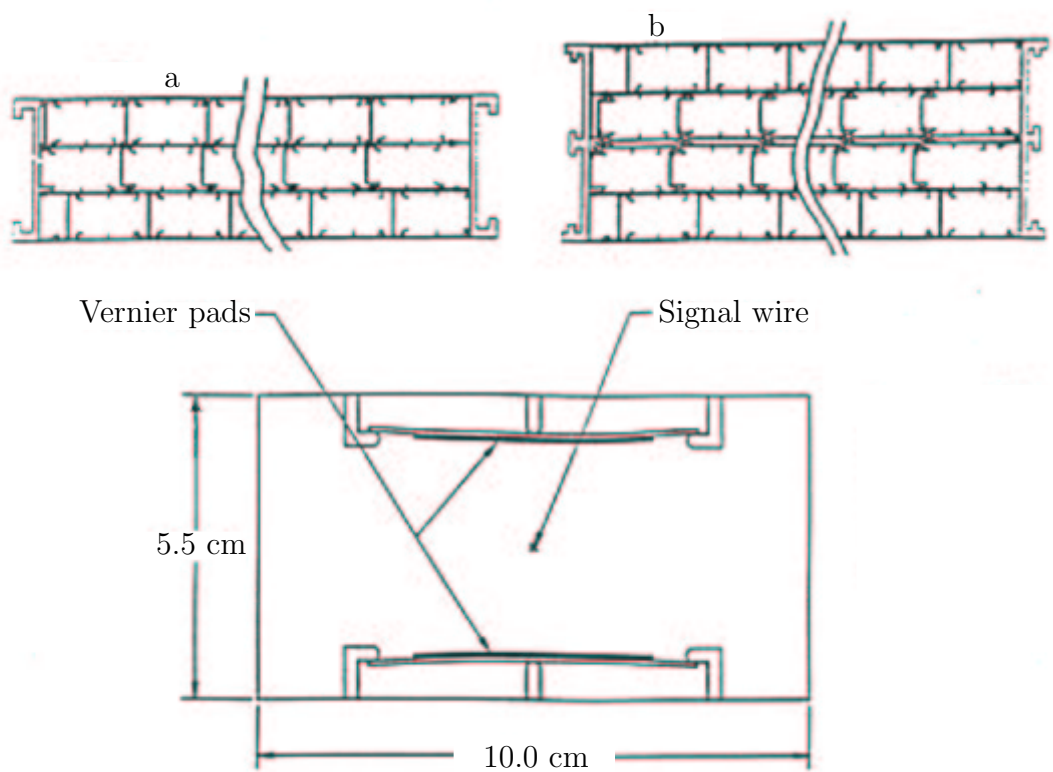


Figure 3.9: Schematic cut-away view of an A-layer PDT assembly (b) and a B- or C-layer assembly (a). The bottom figure shows a detailed view of one PDT tube, including the vernier pads.

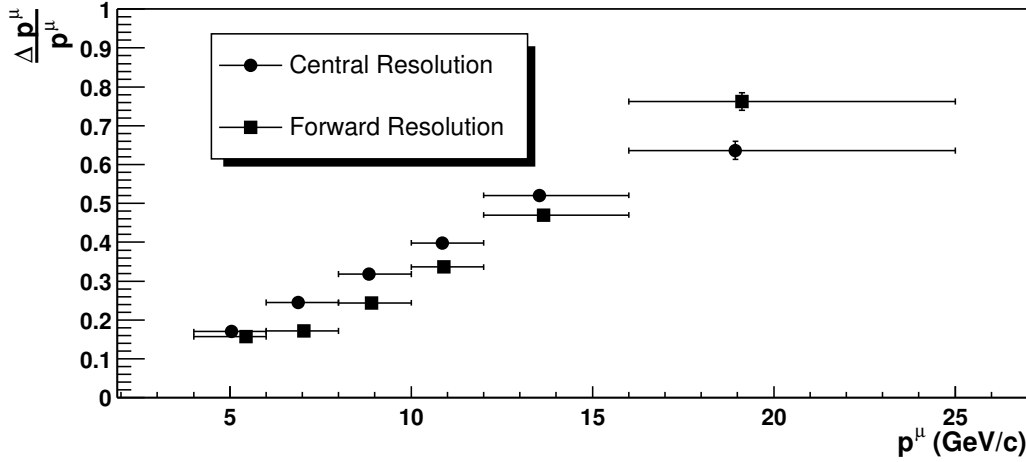


Figure 3.10: *Relative momentum resolution of the stand-alone central (circles) and forward (squares) muon system, measured using tracks reconstructed in the central tracker and extrapolated to the muon system.*

ns beam crossing time. The cells are read out on one side of the wire with a 5.4 ns resolution. Because the cell is only read out on one side, the position of a hit in a pixel detector along the wire is needed to determine the axial position of the hit, thus allowing the measurement of the drift time. The efficiency of a single tube is measured in a test setup to be close to 100%, but this is degraded by the thickness of the tube wall to an efficiency of 94% for tracks perpendicular to the MDT plane. For tracks with an inclination to the MDT plane, the thickness of the wall has less impact, and the efficiency approaches 100%.

Mounted on the face of each layer of MDT tubes are single planes of scintillating material, divided in 8 octants of each 96 slabs of scintillating material (see figure 3.12) [26]. The ϕ segmentation is 4.5 degrees; the η segmentation for the outer nine rows of counters is 0.12, for the inner three it is 0.07. The scintillators are read out by phototubes with an operating voltage of 1.8 kV. When the threshold for passing particles is set at 10 mV, the efficiency for detecting single particles in a test setup is 99.9%, with a time resolution better than 1 ns. The relative momentum resolution with which the FAMUS system measures the tracks is shown in figure 3.10

3.2.4 Forward Proton Detector

The Forward Proton Detector (FPD) is designed to study diffractive processes, and measures protons and anti-protons that are scattered at small angles [10]. The de-

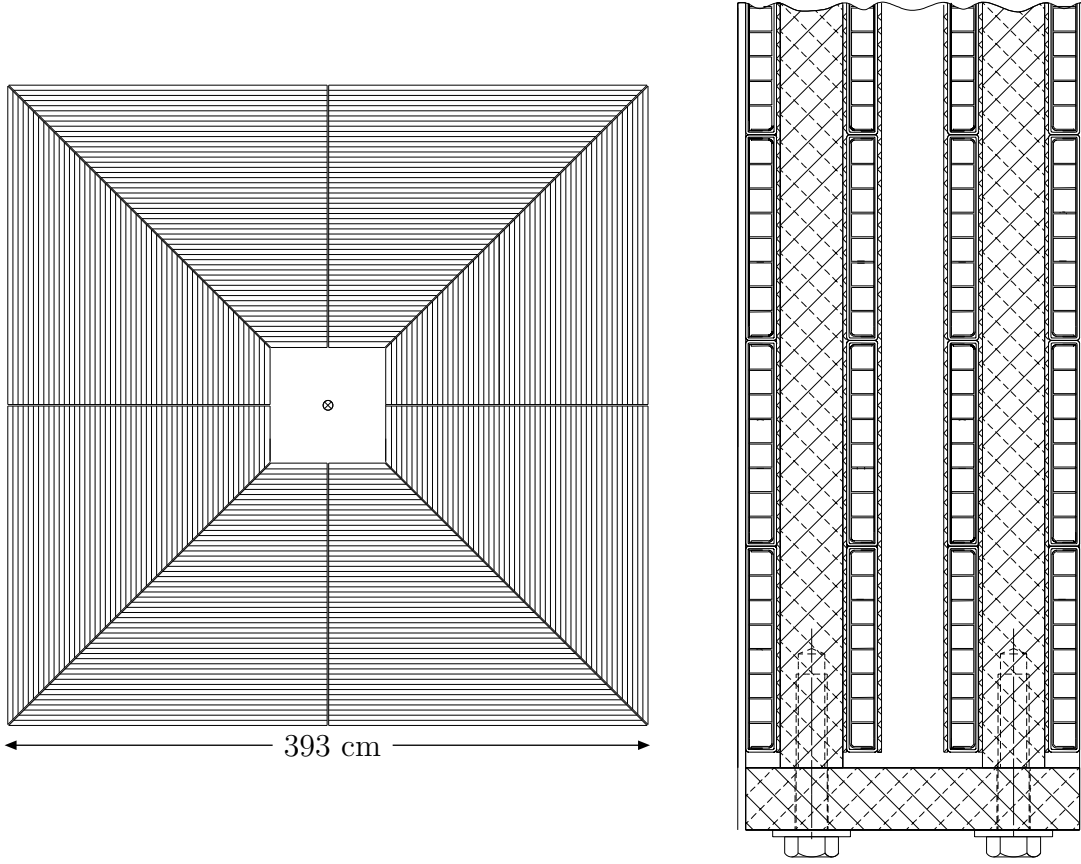


Figure 3.11: *One plane of MDT tubes, showing the division in octants (left) and a schematic cut-away view of an A-layer MDT assembly (right).*

tector is located around 30 meters away from the interaction point. It consists of 9 spectrometers, formed by 18 Roman Pots and the magnets of the Tevatron. The Roman Pots are stainless steel containers that allow a piece of scintillating material to be inserted close to the beam, but outside of the machine vacuum. Each piece of scintillator measures the (x, y) -position of the (anti-) proton passing through with a spatial resolution of $80 \mu\text{m}$, thus providing a 3-dimensional measurement of the position of the particle, which is used in the reconstruction of the particle trajectory.

3.2.5 Luminosity Monitor

The luminosity is measured by identifying beam crossings containing non-diffractive inelastic interactions [20]. This system distinguishes between beam-gas interactions and beam-beam interactions, and whether there have been multiple interactions in the crossing. To reach this goal, two hodoscopes are used, located on the inside face of the

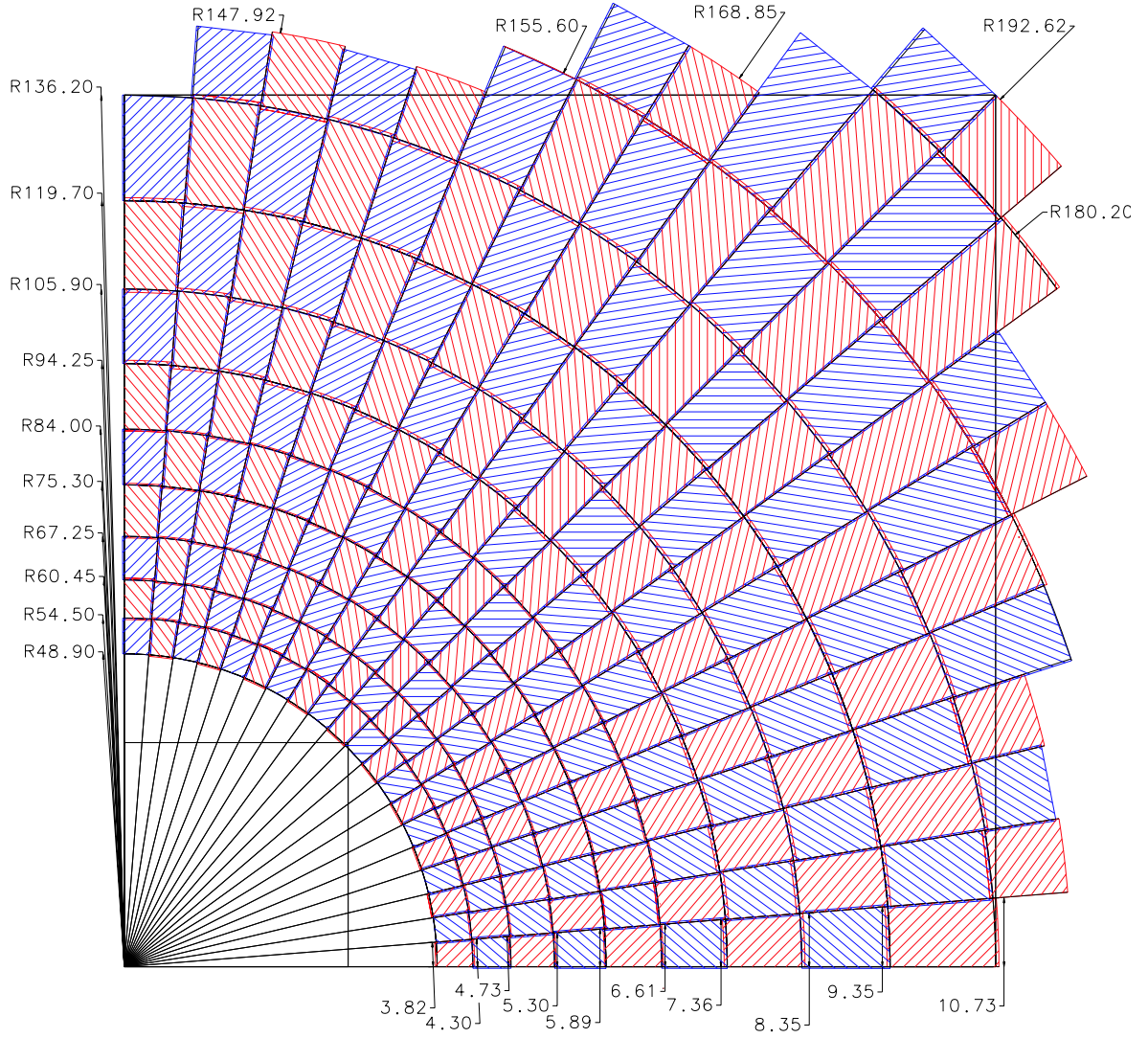


Figure 3.12: One plane of 2 octants of pixels, showing the segmentation in η and ϕ . The units are in cm.

end calorimeters, 135 cm from the center of the detector. Each of these hodoscopes is made of 24 wedge shaped scintillators, with fine mesh photo-multiplier tubes mounted on the face of each wedge. The hodoscopes cover the pseudo-rapidity region $2.7 < |\eta| < 4.4$, providing an acceptance of $(98 \pm 1)\%$ of all the non-diffractive inelastic collisions. In case of a single interaction in the beam crossing, the system provides a fast measurement of the position of the interaction along the beam axis, as well as a measurement of the luminosity. The vertex position of the interaction is calculated by measuring the difference in arrival time of particles in the opposing beam jets.

The resolution with which the detector measures both times is 194 ps, and accord-

ingly the resolution in the measured z -position of the interaction vertex is 10 cm. The trigger rejects events with a vertex position $|z| > 97$ cm, which causes an inefficiency of $< 1\%$ due to the width in the vertex distribution. The luminosity is obtained by measuring the rate of non-diffractive, inelastic collisions with a z -vertex within 97 centimeters of the origin of the detector and dividing it by the total non-diffractive inelastic cross section as it has been measured by E710, E811 and CDF [33]. It is crucial for this measurement to have an accurate correction for multiple interactions in one beam crossing. The design is optimized to have high efficiency in detecting single interaction crossings, while rejecting as many multiple interaction crossings as possible. A rejection factor (defined as the ratio of the number of single to multiple interactions that passed the algorithm) of 12 has been reached, with an efficiency for single interactions of 90%. The measurement of the luminosity has an uncertainty of 10%, mainly caused by the cross section measurement and the uncertainty in the efficiency of the system.

Chapter 4

DØ Trigger System

The frequency of beam crossings at the center of the DØ detector is 4.7 MHz. At the design luminosity of $2.1 \cdot 10^{32} \text{ cm}^{-2}\text{s}^{-1}$, this results in an event rate of 7.8 MHz¹, and a trigger rate of 4.7 MHz. This rate, combined with the average event size of 250 kilobytes, makes it impossible to write all the events to tape without filtering. A dedicated system of filters, called triggers, is thus needed to keep interesting physics events and reject background events. Three levels of triggers have been designed to reach this goal:

- Level 1: A pipelined hardware stage using CFT fibers, preshowers, calorimetry and the muon system to reduce the 4.7 MHz input rate to 10 kHz;
- Level 2: A second hardware stage refining and combining the Level 1 output with multiple preprocessors and a global processor to reduce the 10 kHz rate to an output rate of 1 kHz;
- Level 3: Partial event reconstruction using high level software algorithms running on multiple PC's, delivering a final event rate of 50 Hz to tape.

These trigger levels are explained in more detail below. Special emphasis is placed on the Level 1 muon and jet triggers, since those triggers have been used to select the data for this analysis. The Level 2 and Level 3 trigger systems are discussed in a more general fashion.

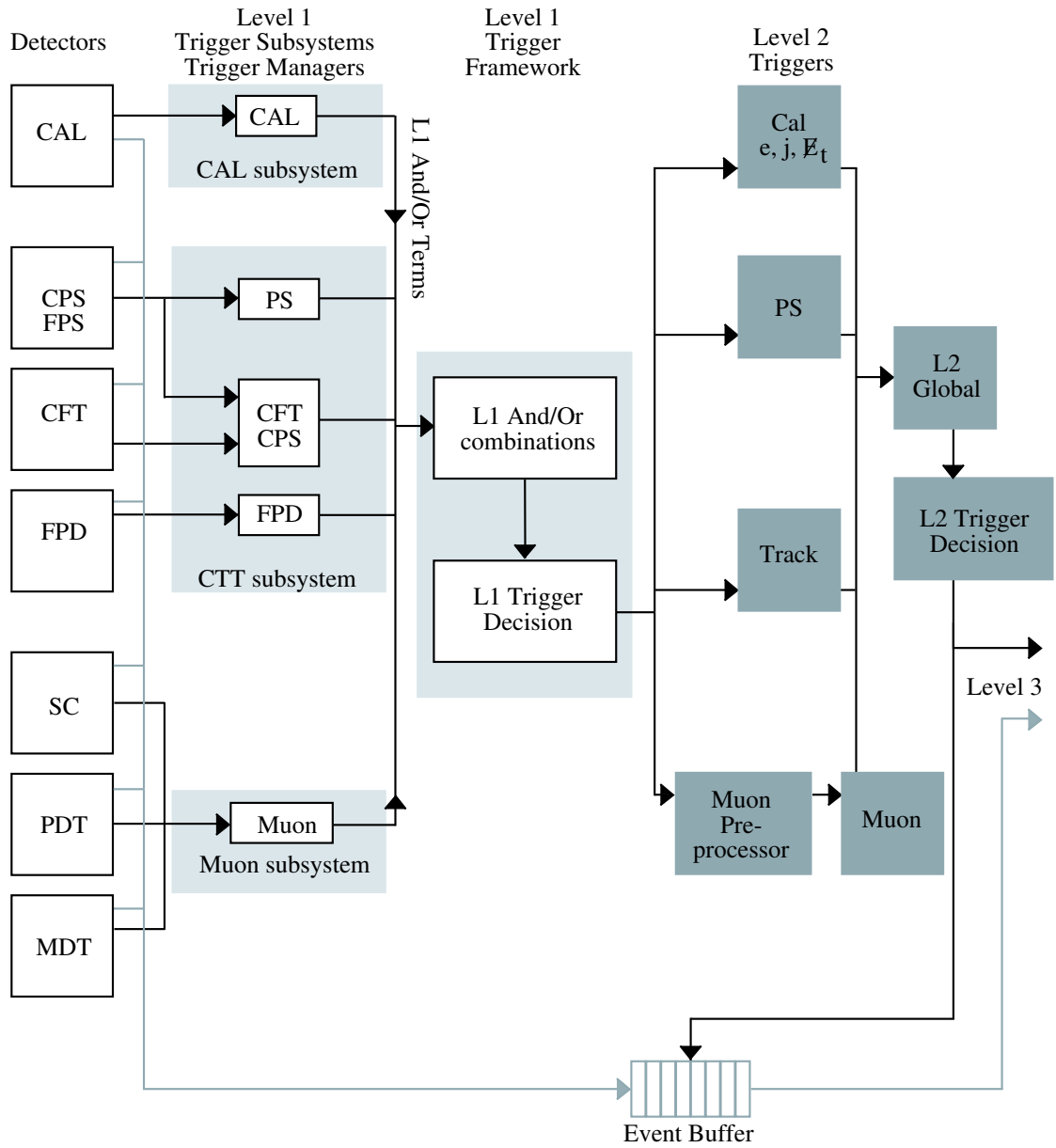
¹The typical luminosity at the time of data taking was approximately $10^{31} \text{ cm}^{-2}\text{s}^{-1}$, resulting in an event rate of 334 kHz.

4.1 Level 1

The Level 1 trigger is a hardware based system filtering the 4.7 MHz trigger rate to an output rate of 10 kHz as input to Level 2, with no dead time. The time available for the Level 1 trigger decision is $4.2\ \mu\text{s}$. The system consists of a number of hardware components:

- Trigger Subsystems;
- Trigger Managers;
- Trigger Framework.

These components are made out of Field Programmable Gate Arrays (FPGA), embedded on electronics boards, in which the trigger logic is implemented. Each of the Trigger Subsystems processes the data for each detector subsystem. The preshower and CFT are combined in the Central Track Trigger (CTT), as shown in figure 4.1. The Trigger Subsystem reports the physics results to a subsystem-specific Trigger Manager. This Trigger Manager evaluates these results, and produces And-Or Input Terms which are sent to the Trigger Framework. These input terms are flags which represent information about the event. This can be physics information, e.g. a found muon, but it can also be beam indicator signals, cosmic background vetoes or any information about the event that is required for a L1 Trigger decision. The entire trigger system contains a maximum of 256 of these And-Or Input Terms, which are combined in And-Or combinations in the Trigger Framework (e.g. a found muon in the muon Trigger Subsystem with a matching track in the CTT Trigger Subsystem). For every beam crossing, the Trigger Framework can evaluate 128 of these And-Or combinations. When at least one of these 128 combinations is positive, and the DAQ system is ready for acquisition of data, the Level 1 Trigger Framework issues an accept, and the event data is digitized and moved into a series of 16 event buffers to await a Level 2 trigger decision. Each of the Trigger Subsystems is discussed in more detail in the following sections.

Figure 4.1: *Level 1 and Level 2 trigger system overview.*

4.1.1 Level 1 Central Track Trigger

The Level 1 Central Track Trigger (CTT) uses the following detector elements [17]:

- Axial fibers of the Central Fiber Tracker;
- Axial strips of the Central Preshower;
- Forward Preshowers strips;
- Forward Proton Detectors.

At Level 1, no information is available from the CFT stereo fibers and the CPS stereo strips. The trigger is split up in a central part, using the Central Fiber Tracker and the Central Preshower, and a forward part, consisting of the Forward Preshower strips and the Forward Proton Detectors.

The central trigger is divided in 80 sectors in ϕ . For each of these sectors, the central trigger determines the number of tracks per p_T interval, as well as the number of fibers hit. There are 4 p_T intervals available:

- 1.5 - 3 GeV/c;
- 3 - 5 GeV/c;
- 5 - 11 GeV/c;
- 11 - 1000 GeV/c.

In addition, the trigger also reports the number of these tracks that have been successfully matched with a cluster in the central preshower. The tracks found are reported to the Trigger Manager, the L1 Muon Trigger and L2 pre-processors. A typical Level 1 trigger that uses a CTT term will fire on the presence of a track that matches with a muon object, on a single high p_T track or multiple low p_T tracks.

The forward trigger combines clusters in the backward u- and v-layers of the FPS with hits in the forward layer of the FPS to tag the clusters as electron- or photon-like. The number of electron and photon candidates per quadrant is reported to the L1 FPS Trigger Manager. In each of the FPD detectors, track segments are reconstructed and matched to form tracks [5]. The number of tracks found is reported to the L1 FPD Trigger Manager. Typically, a Level 1 FPD trigger will require one or two diagonally opposed tracks found in the FPD detectors in combination with one or two trigger towers found by the calorimeter trigger.

4.1.2 Level 1 Calorimeter Trigger

From the viewpoint of the L1 calorimeter trigger, the calorimeter is divided in 1280 projective towers, with 32 divisions in ϕ and 40 in η , resulting in a segmentation of 0.2×0.2 in $\eta \times \phi$ for each tower. In depth, these towers are divided in three sections: an inner electromagnetic section, followed by a hadronic section and a coarse hadronic section. The electromagnetic section is divided in 7 segments in depth, while the hadronic section is divided in 3 segments with some variation depending on the position of the tower. Only the electromagnetic and hadronic sections are used for the L1 trigger decision since the coarse hadronic section typically generates too much noise at L1. The inputs for the trigger are the transverse energies deposited in each of the 1280 electromagnetic and 1280 hadronic sections. These transverse energies are combined in the trigger manager into quantities, which consequently are compared to the trigger criteria to pass or reject the event. Typically the trigger criteria require one or more towers with an energy higher than a certain threshold energy (generally 3, 5, or 7 GeV per tower).

4.1.3 Level 1 Muon Trigger

The Level 1 muon trigger uses both the wires and the scintillators, with additional information from the Level 1 CTT, to base a trigger decision on. The detector information is used in two different trigger algorithms to detect muon tracks. The first combines tracks that are found by the CTT with hits in the scintillators of the muon system. The segmentation of the scintillators matches the segmentation of the CTT in ϕ , and tracks that are found in a ϕ slice of the CFT are matched with hits in the scintillators in the same ϕ slice. A timing gate of 25 ns is used in the scintillators to reject background hits, while a 50 ns timing gate defines cosmic ray veto hits. In the central system, high p_T CFT tracks are matched with an A-layer scintillator hit, as well as with a B- or C-layer scintillator hit, since these tracks penetrate the iron core of the magnet between the A- and the B- and C-layers. In the forward system, all three planes of scintillating counters are used to match the CTT track with scintillator hits.

The other algorithm uses a binary readout (i.e. no drift time information, but solely hit/not-hit information) of the wires to find combinations of hits in different planes, compatible with a straight line track (centroids), and verifies these with matching hits in the scintillating counters. In the central system, the timing information of the scintillating counter hit is needed because the maximum drift time in the PDT's (500 ns) is greater than the bunch crossing time (396 ns). This is not needed in the forward system, where the maximum drift time is 60 ns. A low p_T trigger is defined using only centroids found in the A-layer, while a high p_T trigger is defined using correlations between centroids found in the A-layer and the B- or C-layer. For both algorithms,

four p_T thresholds (2, 4, 7 and 11 GeV/c) are defined.

The information for each octant in each region is combined in the muon Trigger Manager, which produces global muon trigger information. The muon trigger manager makes a trigger decision based on the p_T threshold (2, 4, 7 and 11 GeV/c), pseudo-rapidity region ($|\eta| < 1.0$, $|\eta| < 1.5$ and $|\eta| < 2$), quality (Loose, Medium and Tight) and multiplicity information. This trigger decision is sent to the L1 Trigger Framework where it is included in the global physics trigger decision. Depending on the trigger list, the trigger will fire on a single high p_T muon, multiple low p_T muons, or muons in association with other physics objects (jets, electrons etc.). In case of an accept, the L1 Muon Trigger reports the results to the L2 Muon Trigger, and on a L2 Accept, to the L3 Muon Trigger.

4.2 Level 2

The Level 2 trigger reduces the 10 kHz Level 1 accept rate by an order of magnitude to 1 kHz as an input to Level 3, in an average time budget of 100 μ s [15]. This is done using multi-subdetector correlations of objects found in the event. The Level 2 trigger is running on alpha-processors, and consists of two stages: a preprocessor stage, which processes data from each Level 1 trigger for use in the second stage, which is a global processor that combines this data to make a trigger decision. There is a one-on-one mapping between Level 1 trigger bits and Level 2 trigger bits (see figure 4.1). In the preprocessor phase, each detector system builds a list of trigger information. There are preprocessors for the following subsystems:

- Central tracker;
- Preshower detectors;
- Calorimeter;
- Muon tracker.

Each of these preprocessors will be briefly discussed below. For each subsystem, the Level 1 information is collected and transformed into physical objects like hits, clusters and tracks. The maximum time budget for this preprocessing is 50 μ s. After the physical objects are formed, they are transmitted to the global processor. The global processor correlates the information from the different detector systems to make physics objects like jets, electrons and muons, and makes a trigger decision within maximally 75 μ s. The total deadtime for this Level 2 system is 5%.

4.2.1 Central Track Preprocessor

The Central Tracker preprocessor collects the tracks found by the Level 1 CFT trigger and creates Level 2 tracks [14]. It performs the following tasks for each track:

- It converts the Level 1 binned p_T information into a real p_T value;
- Using the ϕ position at the innermost CFT layer and the measured p_T , the ϕ direction at the vertex is calculated;
- Using the above, the ϕ direction at the third layer of the electromagnetic calorimeter is calculated;
- The isolation of the track is measured.

The tracks are then ordered in p_T and sent to the L2 global processor. The tracks are maintained in memory for Level 3 readout in case of a positive Level 2 trigger decision.

4.2.2 Preshower Preprocessor

At Level 1, the central tracks found by the central track trigger are matched to preshower clusters in ϕ only. The larger time budget at Level 2 allows the preshower preprocessor to improve this match [4]. To this avail, it uses the stereo information from the u- and v-layers of the preshower to calculate the global η - and ϕ -positions of the clusters. These clusters can then be matched with the tracks found by the Level 2 Central Track preprocessor and with calorimeter objects found by the calorimeter preprocessor, to identify different physics objects.

4.2.3 Calorimeter Preprocessor

The calorimeter preprocessor runs three algorithms in parallel [7]:

- Jet reconstruction;
- Photon and electron reconstruction;
- Calculation of missing transverse energy.

From the viewpoint of the Level 2 jet reconstruction algorithm, the calorimeter is divided in towers, which are groups of calorimeter cells with the same η - and ϕ -position, at increasing radial distance from the beam pipe. Towers that fired the Level 1 calorimeter trigger are used as seeds to cluster 5x5 groups of towers around. The total E_T of all the towers in the clustered group must pass a minimum E_T cut to be considered a jet candidate. The E_T of the clusters is calculated assuming that the interaction point is

at $z = 0$. Jets that pass a minimum E_T cut, as defined in the trigger list, are passed to the L2 global processor. The photon and electron reconstruction algorithm processes the electromagnetic towers given by the L1 calorimeter trigger and turns them into seed towers. For each seed tower, it determines which of its nearest four neighbours contains the largest E_T , and the total electromagnetic and hadronic energy in the seed tower and the nearest neighbour is calculated. Based on the total electromagnetic energy, and the ratio of electromagnetic energy compared to hadronic energy, the electromagnetic tower is considered an electromagnetic candidate and passed to the L2 global processor. The missing transverse energy algorithm calculates the vector sum of the E_T in individual trigger towers, passed to it from the L1 calorimeter trigger, and reports it to the L2 global processor if it exceeds a certain value.

4.2.4 Muon Preprocessor

The Level 2 Muon Trigger uses all the wire hits and scintillator hits of the muon system to detect muon tracks. It starts with a pattern recognition step in which straight track segments are reconstructed in each layer of the muon detector. The pattern recognition is done by shifting a 3-tube wide window over all the cells in an octant, looking for wire triplets with a matching scintillator hit (if a scintillator layer is present), see figure 4.2. Combinations of hits are compared with a hit-map to determine which 3-tube combinations are compatible with a straight track segment. This hit-map is created offline using Monte Carlo samples. After this pattern recognition step, found track segments in the A-layer are then combined with track segments found in the B- and C-layers to form Level 2 objects which contain η , ϕ and p_T information.

The pattern recognition step is implemented in a Level 2 sub-level, which runs before the actual Level 2 Muon Trigger. This sub-level incorporates 80 Digital Signal Processors (DSPs) running in a parallel scheme, in which each DSP finds track segments in a small region of the muon detector. The combination of the track segments into tracks is performed in the Level 2 Muon Preprocessor, which reports the found tracks to the Level 2 global processor. Upon a Level 2 Accept, the Level 2 objects are sent to Level 3 to serve as seeds for a more precise muon track reconstruction.

4.3 Level 3

The Level 3 trigger is a software based system characterized by parallel data-paths which transfer data from the detector front-ends to a group of Personal Computers, known as nodes. It reduces the input rate of 1 kHz to an output rate of 50 Hz in an available time of 100 ms. The data that is coming from each detector front-end moves, upon a L2 accept, independently through the data system over the data pathway, and

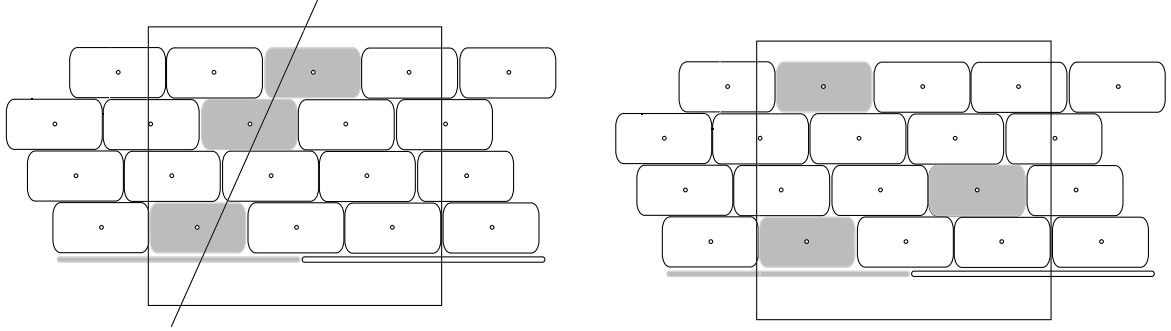


Figure 4.2: *The Level 2 muon pattern recognition uses a three-tube wide window to find track segments. The left plot shows a situation in which the trigger fires: three wire hits and a scintillator hit (grey), compatible with a straight line track. The right plot shows a situation incompatible with a straight line track, which therefore does not pass the trigger.*

is assembled at the assigned Level 3 processor node. A software program, called the Event Tag Generator, then uses the Level 1 and Level 2 trigger bits to assign the event to a certain event class, for example having a high p_T muon, or two jets. The nodes are running high level software algorithms to reconstruct those parts of the event that are interesting for that particular event class, such as electrons, muons and jet candidates, or interesting event topologies. Because of the increased time budget with respect to Level 2, this reconstruction can use more granular information, e.g. drift distances for the wire hits in the muon system, instead of mere binary information, and can use calibrated data, to improve the quality of the reconstructed physics objects. In addition, the SMT information can be used at this stage to improve the central track reconstruction. The event is then accepted or rejected, based on this reconstructed information.

4.4 Triggers used for data selection

The measurement of the b-jet cross section with a muon tag requires the presence of both a reconstructed muon and a jet in the event. A trigger that requires both a muon and a jet will therefore give the highest purity at the highest rate. Single muon or jet triggers give a lower purity, and due to the fact that they were prescaled, they also give a lower rate.

At the time of data taking, only a part of the Level 1 Trigger System was working reliable enough to select muons and jets. Level 2 and Level 3 filters were either inactive, or were running in Mark & Pass mode, which means that the filters were run on the

events that passed the Level 1 trigger, marked it if the event would pass the filter, but irrespective of the Level 2 and Level 3 trigger decision the event was accepted. The Level 1 Trigger System included the calorimeter trigger covering the $|\eta| < 0.8$ region, as well as the muon scintillator trigger, albeit without the matching of tracks from the CTT. Therefore, the trigger used to select the data requires:

- An A+C scintillator coincidence in the muon detector with $|\eta| < 2.0$, with no requirement on the presence of a central track in the CTT;
- A 5 GeV energy deposit in the calorimeter with $|\eta| < 0.8$.

This trigger is combined under the name *mulptxatxx_CJT5*, where the first part, *mulptxatxx*, corresponds to the muon part while the second part, *CJT5*, refers to the calorimeter part of the trigger.

4.5 Efficiency for Jet+ μ Trigger

To calculate the efficiency of this trigger, we split it in two parts: the Level 1 muon trigger efficiency, ϵ_{L1}^{μ} , and the Level 1 calorimeter trigger efficiency, ϵ_{L1}^{cal} , and we calculate both efficiencies separately. If we ignore the correlation between those two triggers for now, we can state for the combined Level 1 efficiency:

$$\epsilon_{L1} = \epsilon_{L1}^{\mu} \cdot \epsilon_{L1}^{cal} \quad (4.1)$$

In section 4.5.3 we will discuss the possible correlation, which turns out to be small.

The strategy to measure ϵ_{L1}^{μ} and ϵ_{L1}^{cal} is based on the use of independent reference triggers. Events that are triggered by these reference triggers are fully reconstructed. In the case that a jet or muon is present, it is checked if the corresponding trigger bit is set. This allows the calculation of the trigger efficiency, as explained in the following sections.

4.5.1 Level 1 Calorimeter Trigger Efficiency

The calorimeter trigger efficiency for the *CJT5* trigger is calculated by selecting events that are triggered by a muon trigger, akin to the *mulptxatxx* trigger explained above, with the additional requirement of a hit coincidence in the luminosity counters, which signals the presence of a hard scattering. In addition, the presence of a reconstructed jet passing quality and kinematic cuts (see section 6.2) is required. The *CJT5* trigger efficiency is calculated by selecting those events in which the *mulptxatxx_CJT5* trigger fired, divided by the number of events in the selected sample, according to:

$$\epsilon_{L1}^{cal} = \frac{\text{Reconstructed jet and mulptxatxx_CJT5 set}}{\text{Reconstructed jet and mulptxatxx set}} \quad (4.2)$$

Figure 4.3a shows the efficiency of the $CJT5$ trigger as a function of reconstructed jet E_T (uncorrected). Correcting the jet energy with the Jet Energy Scale (see section 5.2) results in figure 4.3b. The statistical errors on the trigger efficiency are shown as the vertical lines on the data points.

The dominating systematic error originates from the uncertainty on the Jet Energy Scale correction, which is of the order of 7% (see figure 5.3b). To evaluate the systematic error we first add the error on the Jet Energy Scale correction to the correction for each separate jet, and the Level 1 efficiency is calculated. Then, the same is done but by subtracting the error on the Jet Energy Scale correction. The maximum difference of these two efficiencies with respect to the efficiency calculated with no error on the Jet Energy Scale correction is taken as the systematic error, which is illustrated by the gray band on the bottom of figure 4.3b.

The Level 1 trigger efficiency shows a turn-on curve for jet energies below 40 GeV, reaching 100% efficiency above that energy.

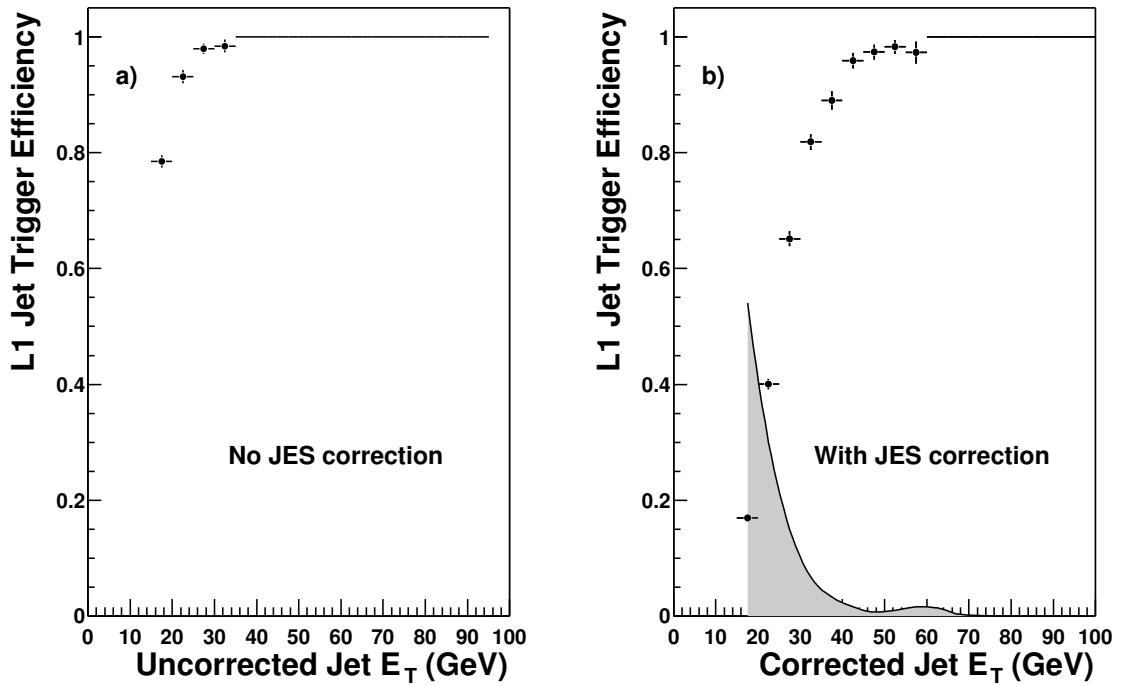


Figure 4.3: *Level 1 Jet Trigger efficiency, uncorrected (top) and corrected (bottom) for the Jet Energy Scale. Data points show statistical error with the gray band showing the relative systematic error.*

4.5.2 Level 1 Muon Trigger efficiency

The Level 1 muon trigger requires a coincidence of a scintillator hit in the A-layer and a scintillator hit in the B- or C-layer. Two reference triggers, which both contain the *CJT5* And-Or Input Term, are used to calculate the efficiency of this trigger, namely:

- *2JT_LO*, requiring two Level 1 calorimeter towers, one with $E_T > 3$ GeV and one with $E_T > 5$ GeV. In addition, at Level 3, two jets reconstructed with a simple cone algorithm and with $E_T > 10$ GeV are required;
- *CEM5_2CJT5*, requiring two Level 1 calorimeter towers with $E_T > 5$ GeV, in addition to a 5 GeV energy deposit in the electromagnetic calorimeter.

For each of these triggers, a sub-sample is extracted from the initial sample for which the reference trigger fired, and an offline reconstructed tight muon that passed modified quality and kinematic cuts was present in the event. These modified quality cuts are the same ones used as described in section 6.1, but with the scintillator hit requirement on the muon tracks removed. This is done to avoid the bias introduced by the fact that the standard quality cuts require both an A- and a B- or C-layer scintillator hit, which is the same requirement that fires the trigger if the times measured on the hits are within the trigger gates.

Normally, requiring the presence of a reconstructed jet close to the muon practically removes all cosmic muons. However, the sample that is extracted here does not have that requirement and therefore still contains cosmic muons. The percentage of present muons that are actually cosmic muons is estimated using two methods: using scintillator times associated with the muon track, and back-to-back muons. The first method selects all muon tracks in the sample that have one or more scintillator hits associated with them. The percentage of these tracks that have a measured time on one of the scintillator hits that is outside the trigger gate is taken as the cosmic muon contamination in the sample. This method results in a cosmic contamination of $(6.3 \pm 0.6(stat) \pm 1.4(sys))\%$, where the systematic error is estimated from the number of tracks that both scintillator hits outside the trigger gate. The second method counts the number of back-to-back muons in the sample, which gives the cosmic muon contamination when divided by the total number of tight muons in the sample. In this scenario a back-to-back muon is defined by a tight muon in the muon system, with another muon at $\delta\phi > 2.5$ radians, at least 2 wire hits in the A-layer and at least 3 hits in the BC-layer of the muon system. This results in a cosmic muon contamination of $(2.8 \pm 0.4(stat) \pm 0.7(sys))\%$, where the systematic error is derived from decreasing the $\delta\phi$ cut to 2.0 radians. We estimate the total cosmic muon contamination by taking the average of these values and assign a systematic uncertainty to cover both methods: $(4.5 \pm 1.8)\%$.

Reference trigger	Efficiency	Statistical Error
<i>2JT_LO</i>	57.8%	1.5%
<i>CEM5_2CJT5</i>	60.7%	1.4%
Combined	59.0%	1.0%

Table 4.1: *Level 1 muon trigger efficiencies measured with different reference triggers.*

The efficiency of the *mulptxatxx* trigger is now calculated by selecting the events in which the *mulptxatxx_CJT5* trigger fired, divided by the number of events which contain a reconstructed muon in the selected sample:

$$\epsilon_{L1}^{\mu} = \frac{\text{Reconstructed muon and mulptxatxx_CJT5 set}}{\text{Reconstructed muon and CJT5 set} - \text{cosmic contamination}} \quad (4.3)$$

Figure 4.4 shows the Level 1 muon trigger efficiency as a function of p_T, η and ϕ of the reconstructed muon for the *2JT_LO* trigger on the left hand side of the plot, and for the *CEM5_2CJT5* trigger on the right hand side. The trigger shows a drop in efficiency for high p_T muons. This is not due to a physics or hardware effect but is shown with later runs using more statistics to be a statistical effect. For the calculation of the μ +jet cross section this effect is taken into account. The drop in efficiency seen in the plot for the Level 1 η efficiency for reference trigger 1 between $0.1 < \eta < 0.5$ can also be attributed to statistics, since this effect is not seen for the second reference trigger. Both the ϕ plots show the effect of the hole in the bottom of the detector in the ϕ region 4.2-5.0, where few muons are reconstructed.

Combining the two data samples, taking into account those events for which both reference triggers fired, results in the final L1 muon efficiency as shown in figure 4.5. The average efficiency of the L1 muon trigger, integrated over η, ϕ and p_T is $59.0^{+2.7}_{-2.4}\%$, where the errors consist of the statistical error of 1.0%, the difference between the combined L1 trigger efficiency and the efficiency of the reference trigger (-1.2%, +1.7%), and an error of 1.8% for the cosmic muon contamination. For the calculation of the cross section we will use the value of the trigger efficiency in each bin separately, with the corresponding error in that bin.

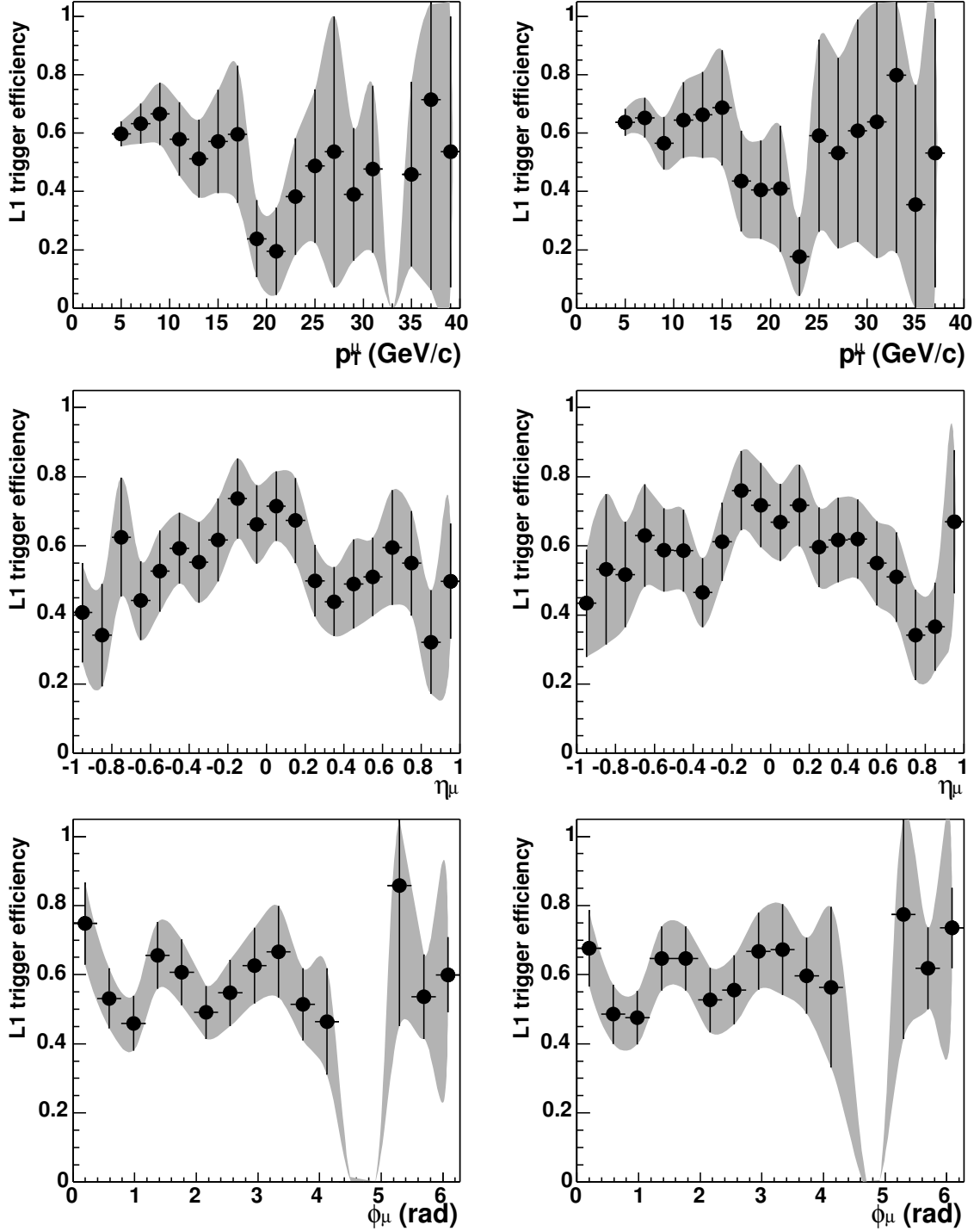


Figure 4.4: Level 1 muon trigger efficiency as a function of p_T , η and ϕ , for the 2JT_LO reference trigger in the left plots and for the CEM5_2CJT5 reference trigger in the right plots. Missing data points (e.g. at $\phi_\mu \approx 4.8$) are due to zero events in the numerator.

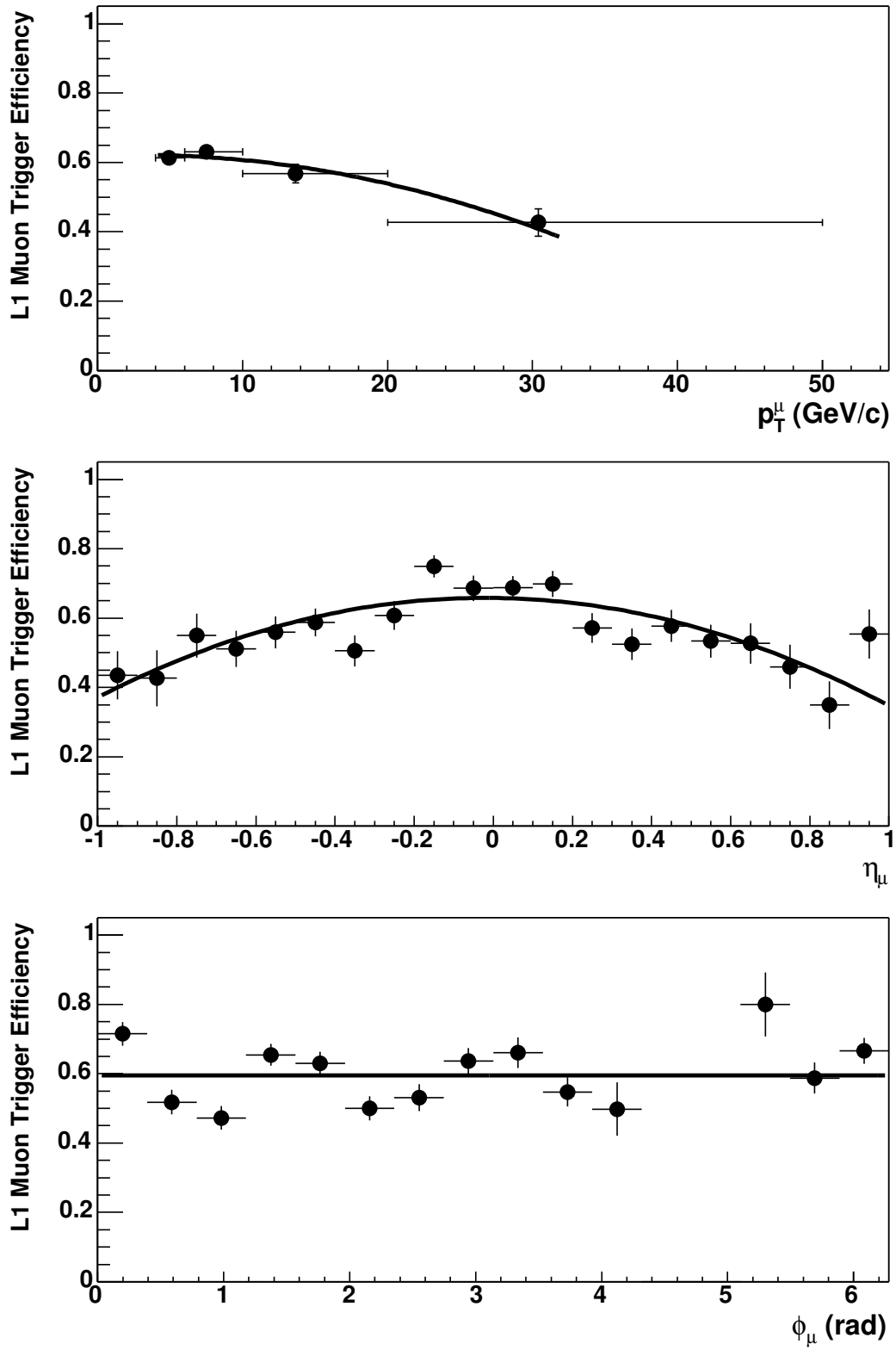


Figure 4.5: Level 1 muon trigger efficiency as a function of p_T, η and ϕ , using both reference triggers

4.5.3 Trigger correlations

Equation 4.1 is only valid if the correlation between the two separate triggers is zero. A priori this is not immediately clear: particles in a jet that fire the jet trigger can punch through the calorimeter, firing the muon trigger as well. Also, a muon, firing the muon trigger, could possibly deposit enough energy in the calorimeter to fire the jet trigger.

The correlation of the muon trigger with the jet trigger due to punch-through particles is zero by construction. The denominator in the efficiency calculation for the muon trigger is a muon with at least two wire hits in the A-layer, and at least three wire hits in the BC-layer. Any punch-through particle that creates such a track is indistinguishable from a real muon, and is treated as a real muon in the trigger efficiency measurements. Only at a later stage is the cross section corrected for the effects of punch-through (see section 6.1.2).

A muon passing through the calorimeter will fire the jet trigger if the muon deposits more than 5 GeV in one trigger tower (0.2×0.2 in $\delta\eta \times \delta\phi$ -space). The extent of this effect on the jet trigger efficiency is investigated in two ways:

- By determining the energy a muon deposits in the calorimeter;
- By calculating the jet trigger efficiency, in the case that a muon is present in the event.

The energy deposited by a muon in the calorimeter is measured by looking at the energy in the calorimeter in a tower of 3 by 3 cells around an isolated muon track. This 3 by 3 tower is 2.25 times as big as the trigger tower, which causes an overestimation of the energy deposited in a trigger tower. The energy deposited by the muon in a 3 by 3 tower is only higher than 5 GeV in $0.23 \pm 0.03\%$ of the cases, which means that the energy deposit of the muon will not fire the trigger by itself. However, it can still bias the jet trigger if this energy deposit is close to a jet, and adds to the energy of the jet. To exclude any possible effect, we also study the jet trigger efficiency in a sample of jets in which a reconstructed muon is present. We again select a sample of events in which the *mulptxatxx* Level 1 trigger fired, a reconstructed jet that passes the quality and kinematic cuts is present, and a reconstructed muon that passes the quality and kinematic cuts is present. Then, we calculate the efficiency as a function of jet E_T according to equation 4.2, with the added requirement of the reconstructed muon in both the numerator and denominator. If we compare the result with figure 4.3, no significant deviation is observed, and we conclude that there is no correlation between the Level 1 muon trigger and the Level 1 jet trigger.

Chapter 5

Offline Event Reconstruction

The events that pass all three levels of trigger criteria are reconstructed offline by the $D\bar{O}$ reconstruction package, named *d0reco*, version p10.15.03. Written entirely in C++, this program uses a modular approach to reconstruct events by identifying physics objects in each subdetector separately. The reconstruction of the two physics objects of interest here, muons and jets, are discussed in detail in this chapter.

5.1 Central Track Reconstruction

The first step in the event reconstruction is the reconstruction of tracks in the SMT and CFT. This is done by TRF++, a package that uses a road-following algorithm followed by a Kalman filter to do pattern recognition in the inner tracker [2]. It takes hit clusters, which represent the observed signals from the detector, as input. It then proceeds by propagating tracks from detector surface to detector surface, picking up hits from these surfaces, or misses in case of inefficiencies, while taking into account the magnetic field and multiple scattering. After this pattern recognition step, the tracks are refitted with a Kalman filter to determine the final parameters.

5.2 Jet Reconstruction

The jet reconstruction algorithm starts with the clustering of energy depositions in the calorimeter into towers, which are then assembled into jets. An energy deposit is added to a jet if its distance to the jet axis in (η, ϕ) -space is less than a cone size R , where R is given by:

$$R = \sqrt{(\Delta\eta)^2 + (\Delta\phi)^2} \quad (5.1)$$

with $\Delta\eta$ and $\Delta\phi$ the distance of the energy deposit to the jet axis in η and ϕ respectively. The definitions for the (η, ϕ) -direction and the transverse energy E_T of the

reconstructed jet are given by the so-called Snowmass accord [30], that defines them as:

$$\eta = \frac{\sum_i E_T^i \eta^i}{\sum_i E_T^i} \quad (5.2)$$

$$\phi = \frac{\sum_i E_T^i \phi^i}{\sum_i E_T^i} \quad (5.3)$$

$$E_T = \sum_i E_T^i = \sum_i E_i \sin(\theta_i) \quad (5.4)$$

where the suffix i denotes the i -th energy deposit in the jet. The reconstruction of the jet proceeds in two stages, clustering and reconstruction of the jet, using the following steps:

1. The energy deposits are segmented in towers with a size of 0.1×0.1 in $\Delta\eta \times \Delta\phi$ space. Towers with $E_T < 0.5$ GeV are ignored to reduce the contamination by noisy cells. Then, starting with the tower with the highest transversal energy as a seed, preclusters are formed in a cone of $R_{precluster} = 0.3$ around this seed. Only preclusters with $E_T > 1$ GeV are kept;
2. Using all preclusters with $E_T > 1$ GeV in a cone of size R , where R is the final cone size, the jet direction and energy are estimated by equations 5.2-5.4, where i then runs over the preclusters. In this analysis, $R = 0.5$ is used, unless stated otherwise.
3. Around this jet direction, all energy deposits within a cone of size R are accumulated, and the new (η, ϕ) -direction of the jet is calculated;
4. Step 3 is repeated until the direction is stable;
5. In the case that two stable reconstructed jets are separated by more than R but by less than $2R$, a new jet axis is defined at the midpoint of the two stable jets. This new axis is then used as a precluster to possibly reconstruct a jet around;
6. If two jets share energy in clusters, they are merged if the shared energy is higher than half of the energy of the lowest energy jet. If the shared energy is lower, each of the shared clusters is assigned to the closest jet;
7. Jets with $E_T < 8$ GeV are rejected.

Jet Reconstruction Efficiency

As explained in step 1 above, the jet reconstruction requires a tower with $E_T > 0.5$ GeV to serve as a starting point from which the jet precluster is formed. This precluster itself is required to have $E_T > 1$ GeV. Absence of such a tower with $E_T > 0.5$ GeV or precluster with $E_T > 1$ GeV will cause the energy that is deposited in the calorimeter not to be assembled into a jet, resulting in an inefficiency. To investigate this possible inefficiency, we study the distributions of transverse energies of towers and preclusters which are used to seed jets. To calculate the inefficiency resulting from not finding the tower, we parametrize the distribution of the energy of the highest energy tower in the jet cone, at different energy ranges, using a gaussian fit F with logarithmic argument. The efficiency to find the 0.5 GeV tower in a particular energy range can then be expressed as:

$$\epsilon = \frac{\int_{0.5}^{\infty} F}{\int_{-\infty}^{\infty} F} \quad (5.5)$$

In other words, the efficiency is the probability for a jet of a given E_T to contain a tower above 0.5 GeV. The energy distributions for two jet energy ranges are shown in figure 5.1, with the gaussian fit applied. For transverse jet energies below 20 GeV, the 0.5 GeV cut causes some inefficiency. With increasing transverse jet energy, the tower energy distribution shifts up, and the cut does not cause any inefficiency. For the jets under consideration in this analysis ($E_T > 20$ GeV), this yields a 100% efficiency.

The inefficiency resulting from not finding a precluster with $E_T > 1$ GeV is found in a similar manner, resulting in the distributions shown in figure 5.2 for the same two energy ranges. Here, a gaussian fit with linear argument is used to fit the data points. The seed energy shifts up with increasing jet transverse energy, also yielding an efficiency close to 100% for jets above 20 GeV.

Jets in the Monte Carlo simulation show a similar behavior as jets in the data.

Jet Energy Scale

The energy of the jet as it is measured by the jet reconstruction algorithm is not exactly equal to the energy that the particles that constitute the jet deposited in the calorimeter, due to a number of effects:

- Offset energy, which consists of:
 - Uranium noise;

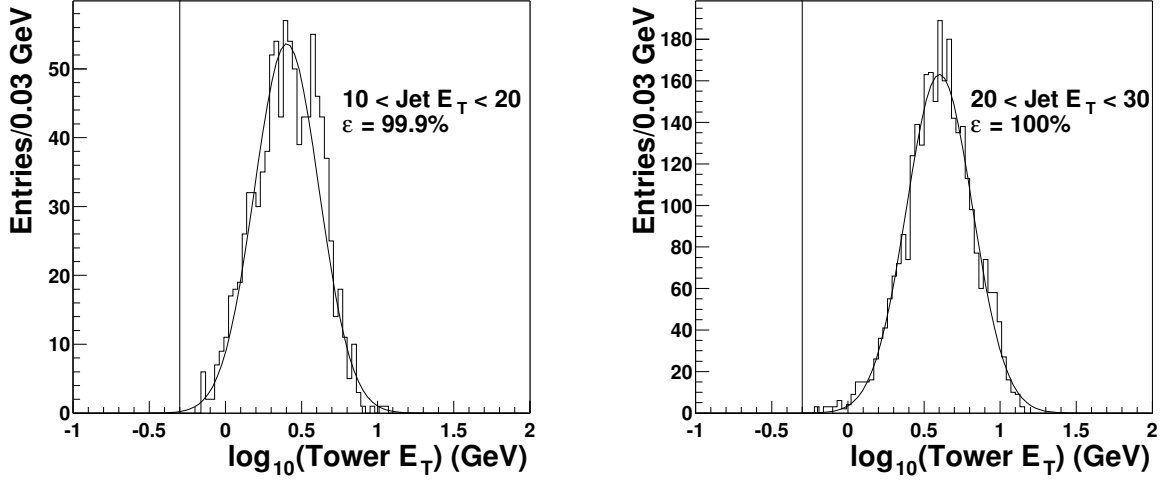


Figure 5.1: Tower transverse energy distributions for jet transverse energies between 10 and 20 GeV (left) and between 20 and 30 GeV (right). The vertical line represents the 0.5 GeV cut on the tower transverse energy, as it is used in the reconstruction algorithm.

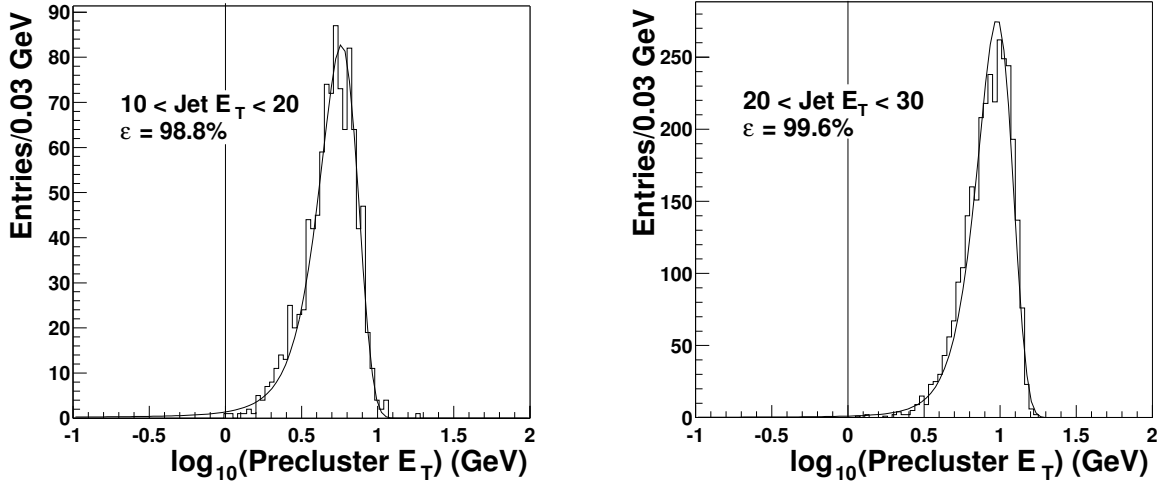


Figure 5.2: Precluster transverse energy distributions for jet transverse energies between 10 and 20 GeV (left) and between 20 and 30 GeV (right). The vertical line represents the 1 GeV cut on the precluster transverse energy, as it is used in the reconstruction algorithm.

- The underlying event, i.e. the interactions of the spectator partons in the proton and anti-proton;

- Pile-up from previous $p\bar{p}$ crossings;
- Multiple $p\bar{p}$ interactions during the same beam crossing.
- The response of the calorimeter to the particles that constitute the jet. The energy measured by the calorimeter needs to be calibrated using a scale factor S_{jet} to provide the exact energy that a particle deposited in the calorimeter;
- Showering of energy inside and outside the jet cone. Particles that belong to the jet can shower outside the defined calorimeter cone, causing their energy to be missed during jet reconstruction. Also, other particles that do not belong to the jet can shower into the defined calorimeter cone, causing their energy to be added to the jet energy.
- Energy carried away by muons and neutrino's. Muons will deposit some energy in the calorimeter due to ionization. Neutrino's in the jet are not measured at all.

If we want to use the jet energy as it is measured in the calorimeter to represent the (true) particle jet energy, we have to apply a procedure that corrects for the above effects. This procedure, the Jet Energy Scale (JES), defines the particle level jet energy as [18]:

$$E_{jet}^{particle} = \frac{E_{jet}^{calor} - E_{offset}}{S_{jet} \cdot F_S} \quad (5.6)$$

where E_{jet}^{calor} is the energy as measured in the calorimeter, E_{offset} is the offset energy, S_{jet} is the response of the calorimeter to the jets, and F_S is the fraction of the jet energy contained within the cone used. In the case of the presence of a muon that is associated with the jet, the Jet Energy Scale needs an additional correction:

$$E_{\mu+jet}^{particle} = E_{jet}^{particle} - E_{\mu}^{calor} + E_{\mu} + E_{\nu} \quad (5.7)$$

where E_{μ}^{calor} is the energy that the muon deposits in the calorimeter, E_{μ} is the energy of the muon itself, and E_{ν} is the energy of the neutrino that is produced conjointly with the muon. This correction is typically extracted from the Monte Carlo simulation.

The effects of the uranium noise and the underlying event on the energy deposited in the calorimeter are measured using dedicated minimum bias runs, from which the correction E_{offset} is deduced. The other two effects affecting the offset energy are both a function of the instantaneous luminosity. During the data taking, the maximum peak luminosity was $1.9 \cdot 10^{31} \text{ cm}^{-2}\text{s}^{-1}$, with the typical luminosity approximately half of that. This results in approximately 0.5 extra minimum bias events per bunch crossing. The calorimeter electronic's baseline subtraction eliminates the effect of these multiple interactions, as well as the effects from pile-up, minimizing the impact of these sources on the total E_T of the jets.

The response of the calorimeter to the jets, S_{jet} , is measured using γ +jet events, in which the photon is back-to-back with the jet. Using the energy of the photon, the calorimeter response is calculated in different jet energy bins.

The out of cone showering of particles in the jet is estimated by comparing the fraction of the energy contained within the jet cone, $R = 0.5$, with the energy in a larger cone, $E_{jet \text{ limit}}$:

$$F_S = \frac{E_{cone}}{E_{jet \text{ limit}}} \quad (5.8)$$

The size of this larger cone is based on Run I studies, and is 1.0 for the jets in the data sample.

The resulting Jet Energy Scale for data jets measured in this way is shown in figure 5.3a. The correction decreases for higher E_T jets, and increases slightly towards higher $|\eta|$, due to the effects of the intercryostat region where there is less calorimeter coverage. The total error on the correction, shown in figure 5.3b, is approximately 7%, independent of jet E_T .

The Jet Energy Scale described above has a dependance on different properties of the jet, like the width of the jet, the number of towers in the jet and the fact that a tower with high energy is present in the jet. It is measured using jets in data that is taken with an electromagnetic trigger. In the data sample used for this analysis, a calorimeter trigger is used which could result in jets which are different from the jets used to measure the Jet Energy Scale. This would then result in an over- or underestimation of the energy correction used. This phenomena is investigated and it has been shown to have no significant effect on the Jet Energy Scale measured.

Hot cell suppression

A hot cell is a calorimeter cell reporting energy which is not due to a particle depositing energy in that cell. These cells are in general isolated, and tend to report energy in multiple subsequent events. This energy is partially suppressed at the hardware level, but additional suppression is performed on an event-by-event basis, by running the NADA (New Anomalous Deposit Algorithm) package over all calorimeter cells prior to the jet reconstruction to remove any cells which appear to be hot [25]. The efficiency of this algorithm is shown in table 5.1 for different values of the parameter E_{cut}^{cell} , which is the energy for which a hot cell is rejected if there is no neighboring cell with that energy. With this parameter, the misidentification rate of genuine energy depositions as hot cells, i.e. the purity of the algorithm, is negligible.

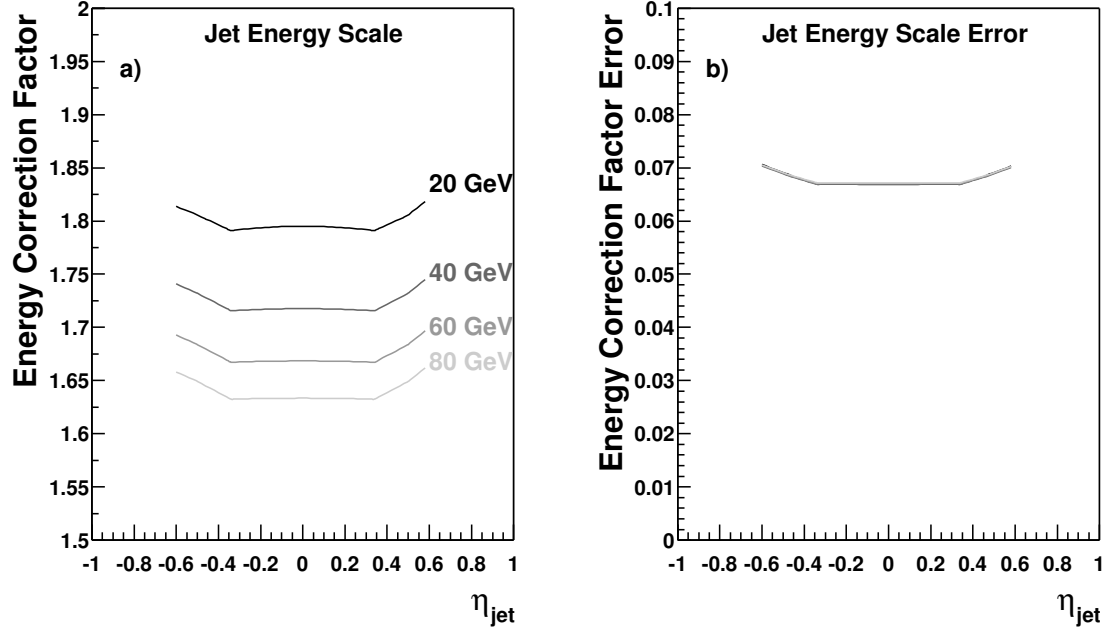


Figure 5.3: *Jet Energy Scale* for different jet transverse energies as a function of η^{jet} . The errors on the *Jet Energy Scale*, shown in plot b) are energy independent, causing the different lines to overlap.

Calorimeter	$E_{\text{cut}}^{\text{cell}} = 100\text{MeV}$	$E_{\text{cut}}^{\text{cell}} = 300\text{MeV}$
CC	64%	93%
ICR	63%	91%
EC	59 %	88%

Table 5.1: *Efficiency of NADA in different regions of the calorimeter.*

Jet Energy Resolution

The resolution of Jet Energy Scale corrected jets is extracted from di-jet events using the asymmetry variable \mathcal{A} , which is defined as:

$$\mathcal{A} = \frac{p_T^{(1)} - p_T^{(2)}}{p_T^{(1)} + p_T^{(2)}} \quad (5.9)$$

where $p_T^{(1),(2)}$ is the p_T of each jet in the event. When plotted in different bins of p_T^{event} , where

$$p_T^{event} = \frac{p_T^{(1)} + p_T^{(2)}}{2} \quad (5.10)$$

the distribution of this asymmetry variable expresses a gaussian shape with width $\sigma_{\mathcal{A}}$ for $p_T^{event} > 30$ GeV/c. The relative resolution of reconstructed jets, $\frac{\sigma_{p_T}}{p_T}$ can now be expressed as:

$$\frac{\sigma_{p_T}}{p_T} = \sqrt{2}\sigma_{\mathcal{A}} \quad (5.11)$$

For events with low values of p_T^{event} , $p_T^{event} < 30$ GeV/c, the resolution cannot be extracted from the data in this fashion. This is due to the fact that the jet reconstruction only reconstructs jets with uncorrected $E_T > 8$ GeV. The Jet Energy Scale correction of approximately 1.8 for low energy jets scales this lower bound up to 14.4 GeV. Therefore, there is no contribution of jets with $E_T < 14.4$ GeV to the resolution. Jets can fluctuate out of the low E_T bins, but due to the lower bound cut-off, no jets can fluctuate into the low E_T bins. This situation is different in the Monte Carlo simulation, where the Jet Energy Scale correction is approximately 1.2, and the lower bound is scaled up to 9.6 GeV. To avoid biases resulting from this effect, events with $p_T^{event} < 30$ GeV/c are not taken into account in the fit for the jet resolution function.

To measure the asymmetry variable, di-jet events are selected in which both jets pass the standard jet quality cuts (see section 6.2), and with the requirement that:

- Both jets have $|\eta| < 0.6$, the same region in which the cross section is later measured;
- The jets are back-to-back to ensure energy balance in the event: $\Delta\phi > 175^\circ$.

In addition, a number of quality cuts are imposed on the event:

- A cut on missing E_T : $\cancel{E}_T < 0.7p_T^{leading\ jet}$, to ensure reasonable energy balance in the event;
- A cut on the total energy deposited in the calorimeter: $E_{tot} < 2$ TeV, to remove events with noisy calorimeter readout.

The resulting distributions for the asymmetry variable are shown in figure 5.4 for different bins of p_T^{event} . The first two plots, 5.4a and 5.4b, show the effects of the low energy cut-off in the data. Figure 5.4a shows an artificially small resolution due to the small energy range (14.4 GeV - 20 GeV) in which the resolution is measured. Figure 5.5 shows the distributions of the asymmetry variable in the Monte Carlo simulation, where the effects of the low energy cut-off have less effect. Figure 5.6 summarizes these plots by showing $\frac{\sigma_{p_T}}{p_T}$ as a function of p_T^{event} for both the data and the Monte Carlo simulation. Both distributions in figure 5.6 are fitted with a function of the form:

$$\frac{\sigma_{p_T}}{p_T} = \sqrt{\frac{N^2}{p_T^2} + \frac{S^2}{p_T} + C^2} \quad (5.12)$$

Noise fluctuations affect the resolution in the low energy range with a N^2/p_T^2 dependence, while the nature of the incident particles and the intrinsic energy resolution contribute to the S^2/p_T term. The C^2 term represents the limited resolution at high energies due to detector imperfections. The shape of the function is based on Run I experience. The fit is performed in the range 30-120 GeV, as shown by the solid lines. The values for the fitted parameters are shown in table 5.2 for both data and Monte Carlo simulation. The difference in resolution between the data and the Monte Carlo simulation is demonstrated with the dotted curved line, which is the squared difference between the fitted data and the Monte Carlo simulation resolution functions. The Monte Carlo simulation underestimates the energy resolution of the jets. This can be attributed to a lack of non-linearity corrections of the energy measured in each calorimeter cell, as well as an incorrect modelling in the simulation of the noise in the calorimeter. The energy resolution of jets in the data compared to that in the Monte Carlo simulation explained above will be used at a later point in the analysis to smear jets in the Monte Carlo simulation, to have the Monte Carlo simulation better represent the data. However, the resolution is also used

to unfold the distribution of jets, and for this purpose the measured jet energy resolution is overestimated, due to two effects:

- Soft radiation resulting in a third jet in the event;
- Particle level imbalance.

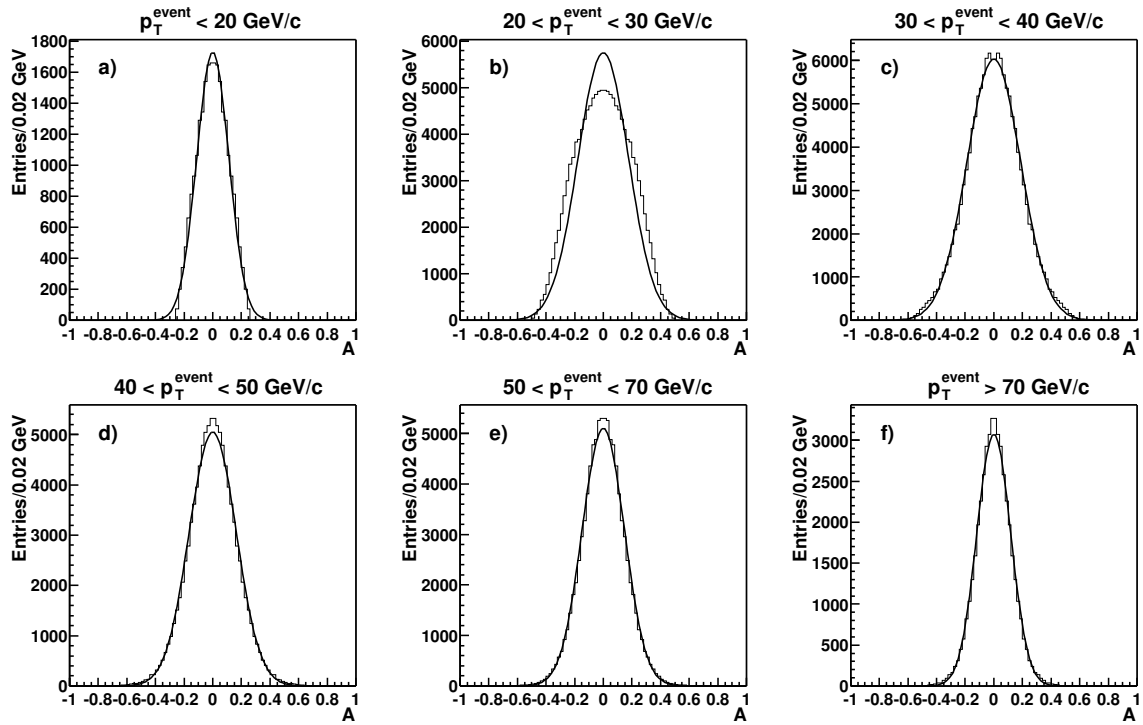


Figure 5.4: Asymmetry distribution for data jets in different bins of p_T^{event} . The first two distributions, a) and b), do not represent the asymmetry variable, since they suffer from a bias due to the cutoff of the jet energy.

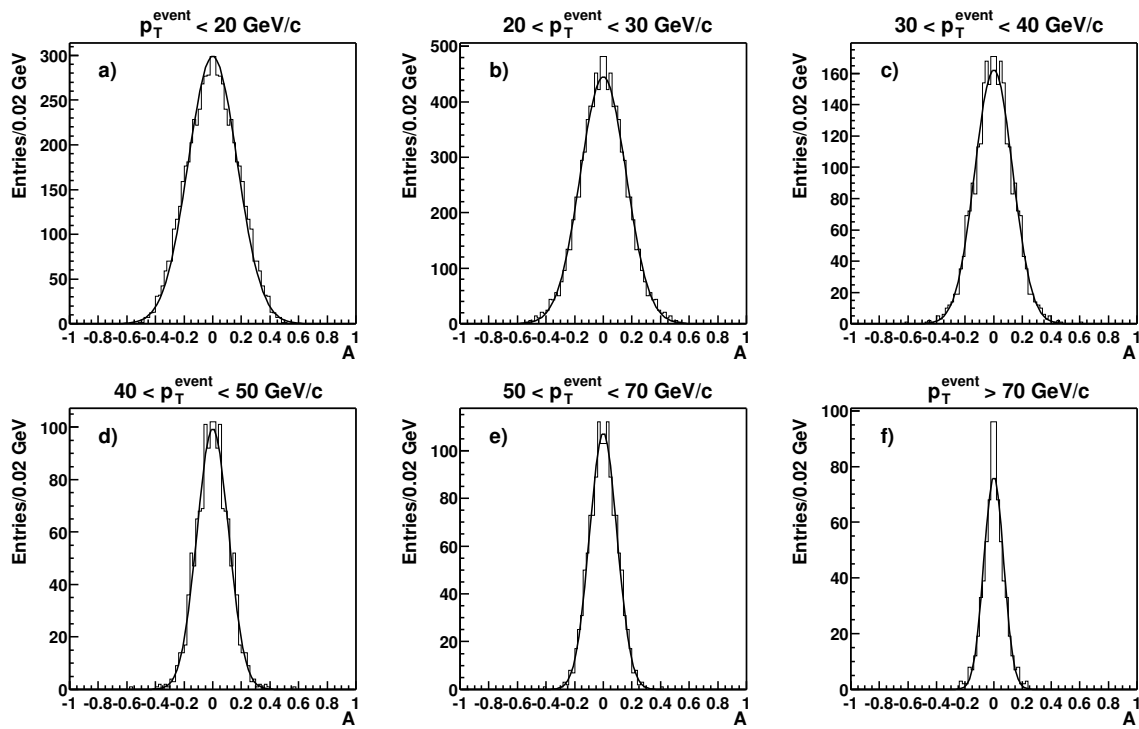


Figure 5.5: Asymmetry distribution for jets in the Monte Carlo simulation in different bins of p_T^{event} .

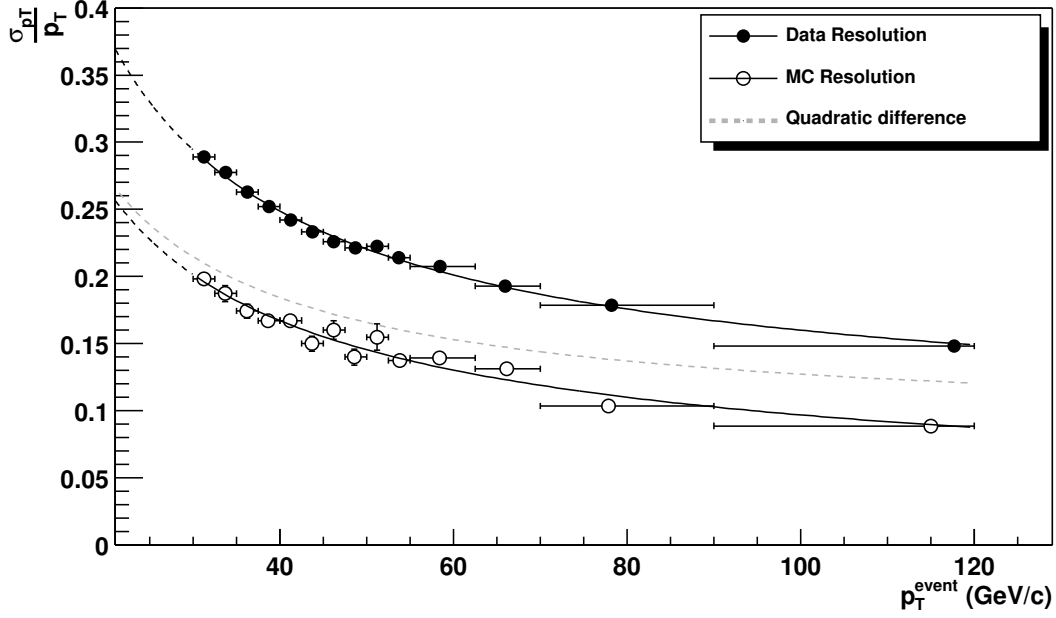


Figure 5.6: Jet resolution as function of p_T^{event} , in the data (solid circles) and in the Monte Carlo simulation (open circles). The curved line represents the squared difference between the resolution in the data and the resolution in the Monte Carlo simulation.

Even though the jets are required to be back to back ($\Delta\phi > 175^\circ$), energy assembled in a possible third jet in the event coming from soft radiation can cause the energy in the event to be less balanced, thereby worsening the resolution of the jet energy measurement. This effect is investigated by looking at the jet energy resolution as a function of the p_T of the third jet in the event [8]. Extrapolating the jet energy resolution to a zero energy of the third jet results in the resolution corrected for soft radiation. Figure 5.7 illustrates the effect of the energy of the third jet in the event. The different lines represent the jet resolutions for different p_T cuts on the third jet, which shows that the resolution gets better with decreasing p_T of the third jet. The

	N	S	C
Data	4.5 ± 1.7	1.3 ± 0.2	0.087 ± 0.034
MC	3.4 ± 0.72	0.91 ± 0.061	0 ± 0.10

Table 5.2: Parameters resulting from the fit to the energy resolutions for jets in the data and the Monte Carlo simulation.

strategy is now to make slices in bins of p_T^{event} , and fit a straight line through the values of the resolution at different values of the transverse momenta of the third jet, p_T^3 . The intercept of the straight line at $p_T^3 = 0$ represents the corrected resolution. This is shown in figure 5.8 for $p_T^{event} = 30$ GeV and $p_T^{event} = 80$ GeV. The point-to-point correlations of the errors on the data points in these graphs are very large due to the fact that each data point is the result of a subset of the data used for the data point to its immediate left. Therefore, we take the systematic error on this method to be the smallest error of all the errors on the data points used in the fit. If the error on the intercept, coming from the straight line fit to the points, is larger than this error, we take that as the systematic error instead. Figure 5.9 shows the jet resolution, updated for this third jet correction, with the dotted lines representing the errors resulting from this method.

The particle level imbalance correction accounts for the fact that a cone algorithm is used to define jets. At particle level, that is, before the particles enter the calorimeter, some of the tracks that should belong to the jet are outside the cone and are not taken into account in the jet properties. When we later unfold the jet cross section, we need to unfold such that we account for this effect. This correction is different than the Jet Energy Scale correction that has been mentioned before, which corrects for the effects of in- and out of cone showering of particles inside the calorimeter. To measure the extent of the effect of the particle imbalance, we extract a sample of particle jets from the Monte Carlo simulation, using the exact same cuts as explained above, and measure the resolution using the same asymmetry variable. The resolution of the particle jets obtained from the Monte Carlo simulation is shown in figure 5.10. We can now write the true resolution that can be used for the unfolding as a convolution of the measured jet resolution, the soft radiation effect and the particle imbalance:

$$\left(\frac{\sigma_{p_T}}{p_T}\right)_{True}^2 = \left(\frac{\sigma_{p_T}}{p_T}\right)_{Cal} \oplus \left(\frac{\sigma_{p_T}}{p_T}\right)_{Soft Rad} \oplus \left(\frac{\sigma_{p_T}}{p_T}\right)_{Part Imb} \quad (5.13)$$

The first convolution represents the third jet correction as explained in the previous paragraph, while the second represents a squared difference:

$$\left(\frac{\sigma_{p_T}}{p_T}\right)_{True}^2 = \left(\left(\frac{\sigma_{p_T}}{p_T}\right)_{Cal} \oplus \left(\frac{\sigma_{p_T}}{p_T}\right)_{Soft Rad} \right)^2 - \left(\frac{\sigma_{p_T}}{p_T}\right)_{Part Imb}^2 \quad (5.14)$$

Figure 5.11 shows the resulting true jet resolution. The dotted lines represent the total systematic error on the jet resolution, resulting from the fits to the data points, the error on the soft radiation correction and the error from the particle imbalance.

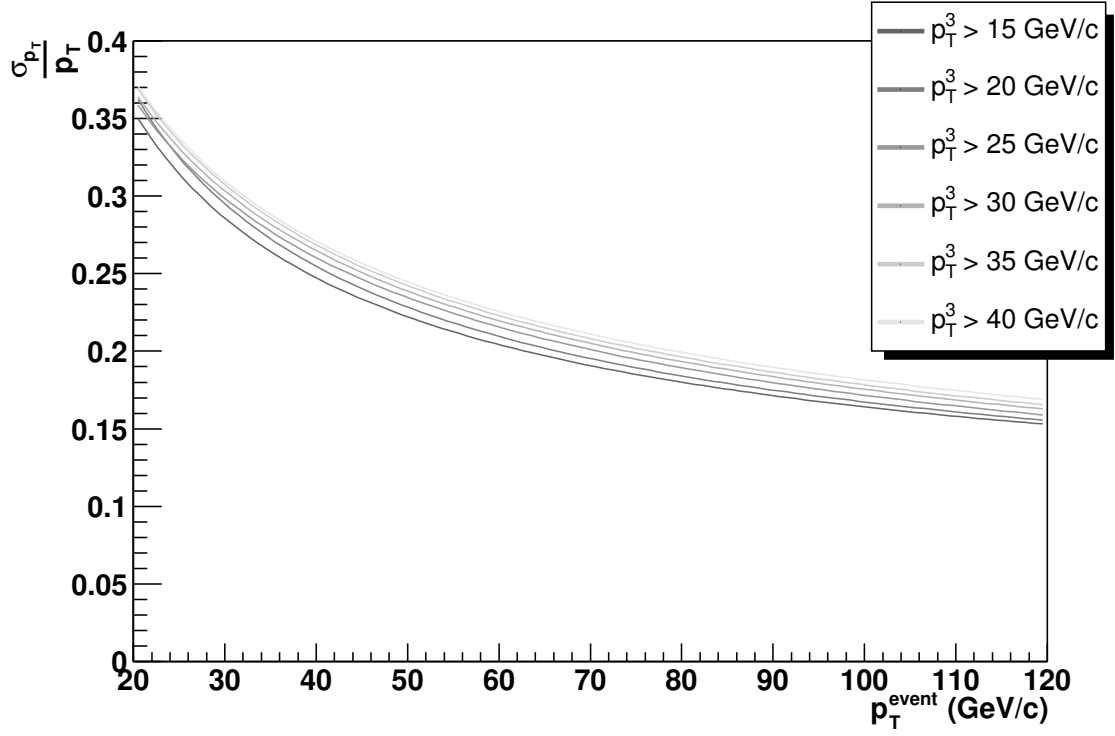


Figure 5.7: *Effect of the presence of a third jet in the event on the jet resolution. The different lines represent different p_T cuts on the third jet.*

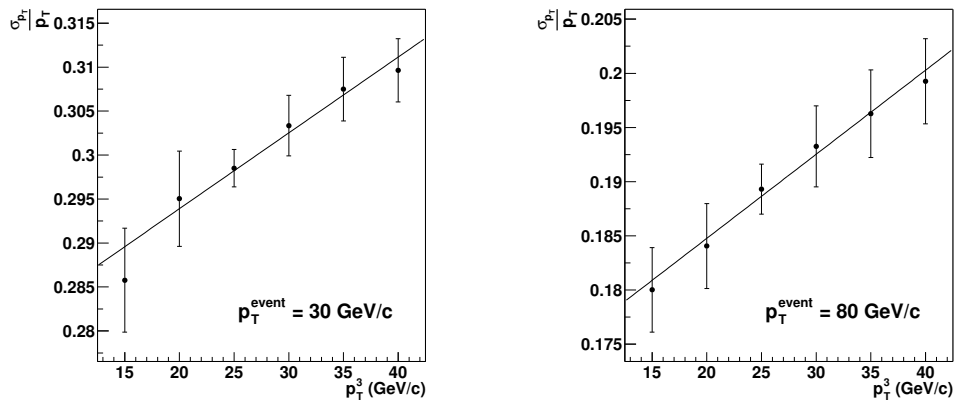


Figure 5.8: *Extrapolation of the jet resolution in two p_T^{event} bins, $p_T^{event} = 30$ GeV (a) and $p_T^{event} = 80$ GeV.*

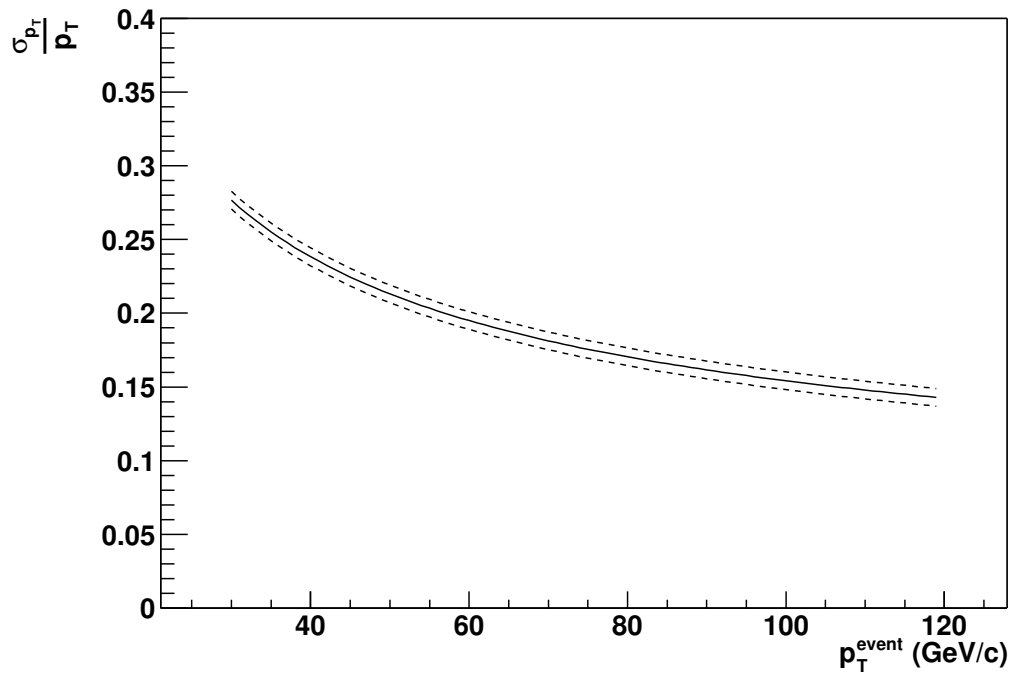


Figure 5.9: *Jet resolution, corrected for the effect of a possible third jet in the event. The dotted lines represent the errors coming from this correction.*

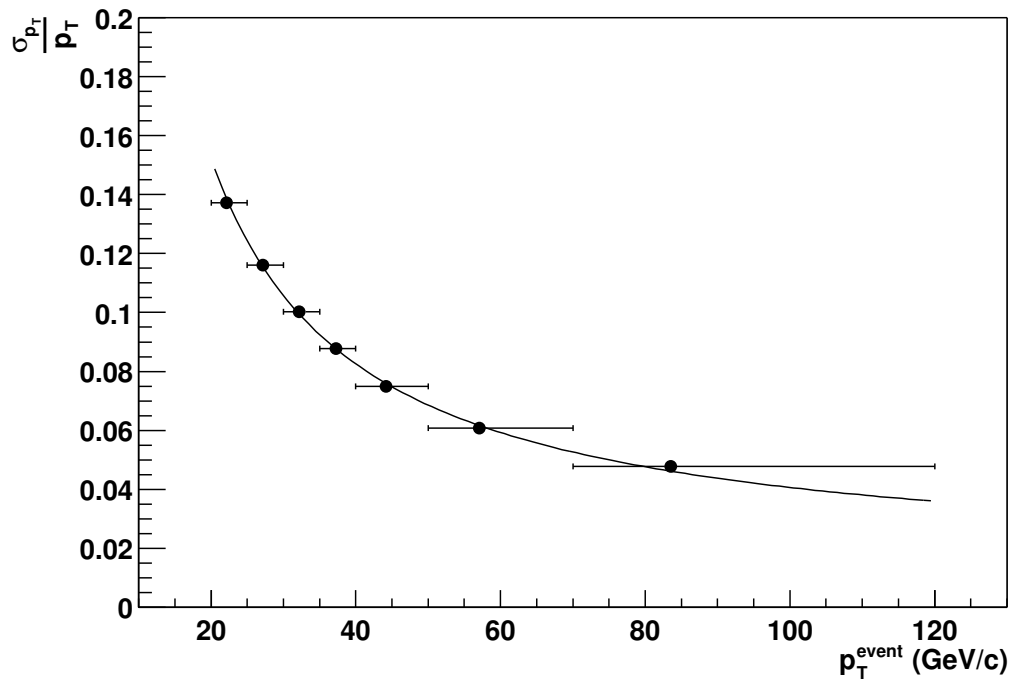


Figure 5.10: *Jet resolution for particle jets obtained from the Monte Carlo simulation.*

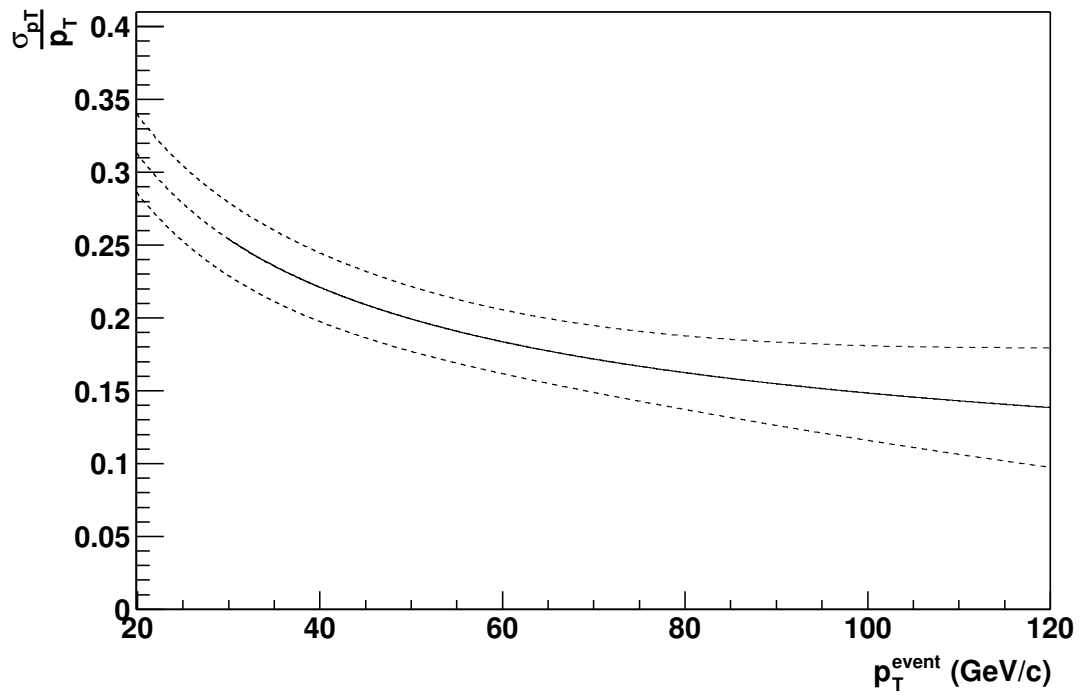


Figure 5.11: *Jet resolution in the data, corrected for both soft radiation corrections and particle imbalance corrections. The dotted lines represent the errors on the resolution.*

Jet Direction Resolution

The resolutions of the jet direction measurement becomes important in the analysis when Monte Carlo templates are used to fit to the data. Especially the difference between the Monte Carlo and the data resolution is important. To get a handle on the resolution of the jet direction, samples of di-jet events are extracted from the data and the Monte Carlo simulation using the same selection criteria as in the previous section. For these events, the differences in η and ϕ between the two jets are shown in figure 5.12 for both data jets and Monte Carlo jets. The difference in ϕ is sensitive to the resolution, since it is the deviation of one jet from the back-to-back axis in di-jet events. The difference in η is less sensitive to the resolution of the measurement of the η direction of the jets, since there is no need for an energy balance in η . Since we are considering central jets here, we assume that the resolution in η is similar to the resolution in ϕ . The absolute value of the resolution is not directly important for this analysis; it is important for the Monte Carlo templates deduced later that this resolution is similar in the data as in the Monte Carlo simulation, as can be concluded from this study.

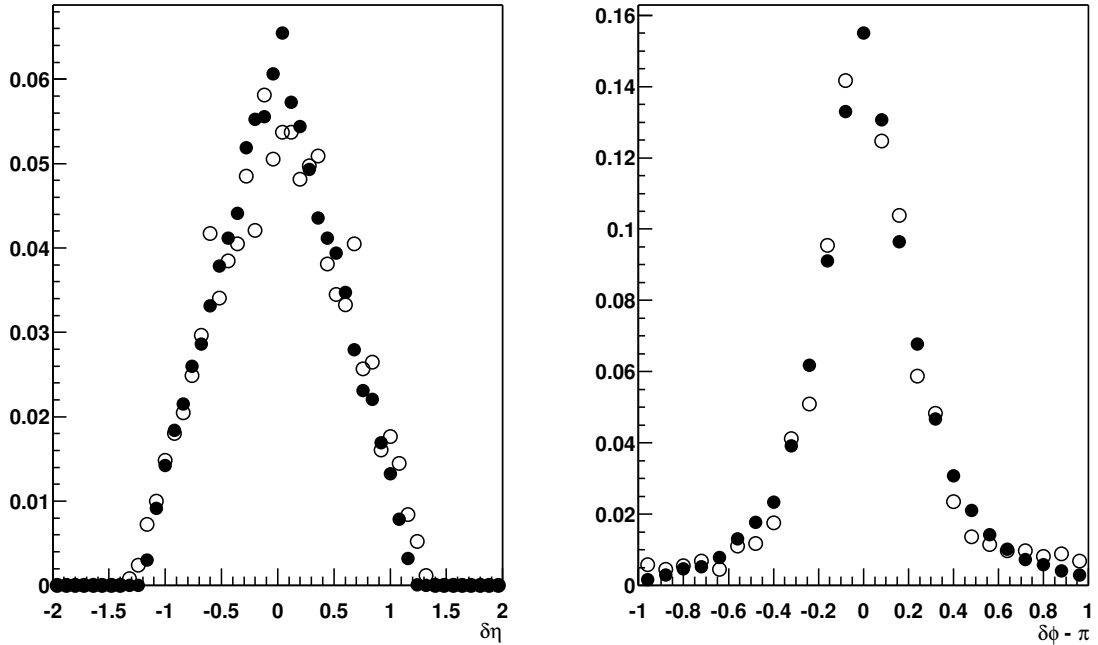


Figure 5.12: *Difference in η - and ϕ -direction between jets in di-jet events in data (solid circles) and the Monte Carlo simulation (open circles). The vertical scale is arbitrary.*

5.3 Muon Reconstruction

The reconstruction of local muon tracks (i.e. measured in the muon system only) from single hits proceeds by a number of steps:

- The reconstruction of raw data (i.e. the times measured at the readout of the channels in the muon system) into positions and times of hits in scintillators, and positions and drift circles of wire hits;
- The combination of reconstructed wire and scintillator hits in each layer into straight lines, called segments;
- A fit of reconstructed segments in the A-layer with reconstructed segments in the B- and C-layers to measure the momentum of the muon.

Each of these will be discussed in more detail below.

5.3.1 Hit Reconstruction

The tracking in the muon system uses three different types of detectors:

- Scintillators;
- Proportional Drift Tubes in the central muon system (PDTs);
- Mini Drift Tubes in the forward muon system (MDTs).

The hits in the scintillators are mainly used to trigger on events and to determine the time of flight of particles passing through the counters. Additionally, they are used as a position determination of the track. Especially in the forward system, where the MDTs do not provide a measurement of the track position along the wire, hits in the scintillating counters are required to measure the axial, or ϕ , position of the track¹. In the central system, they improve the axial position measurement of the track.

Because of the dual time read out (see figure 3.7), the wire hits in the central system provide a measurement of the drift time and the axial time. The axial time determines the axial position of the passing particle, while the drift time is used as one of the two inputs needed to calculate the distance in the drift plane of the particle to the wire. The drift plane is the plane of the drift circle of the hit, perpendicular to the wire. The other input to this drift time to distance conversion is the angle of the track in the drift plane of the hit. This angle dependence is taken into account at the segment reconstruction step, at which point the angle of the track is known.

¹The axial position is the position along the wire. Since the wires are directed parallel to either the global x or y axis, the axial position corresponds to the ϕ position.

In the forward system, the hits on the MDT wires provide one time measurement, namely the sum of the drift and axial time. When the position of the track along the wire is known (by using the position of a scintillator hit on the segment), the drift time can be measured and used to calculate the distance of the passing particle to the wire. The time to drift conversion relation for the MDT hits is not dependent on the angle of the track in the drift plane of the hit.

Hit Efficiencies

We measure the efficiency of the wire hits and the scintillator hits by using reconstructed segments. For the wire hits, the segment is reconstructed with the tubes in one plane ignored, to avoid biases of possible hits in that plane on the reconstruction of the segment. We require the segment to be reconstructed with a hit on all other planes, to make sure that the direction and position of the segment are well known. We define the single plane efficiency as the efficiency that at least one reconstructed hit is present in the relevant tubes ². For the PDTs this results in a single plane efficiency of $92.7 \pm 0.4\%$. We can also study the single PDT hit efficiency as a function of drift distance and the total distance (or ionization length) that the track traversed in the tube. This is shown in figure 5.13. Up to a drift distance of 3 cm, the single hit efficiency is constant at around 90%, to drop rapidly for larger distances. A similar structure can be seen for the ionization length of the track in the tube, where the PDT hits become efficient for ionization lengths above 5.5 cm.

For the MDTs, this algorithm results in a single plane efficiency of $89.2 \pm 0.4\%$. The single hit efficiency as a function of drift distance and ionization length is shown in figure 5.14, where can be seen that the efficiency of the MDT tubes does not depend on the drift distance or the ionization length of the track in the tube.

The scintillator hit efficiency is measured using segments reconstructed with wire hits only, which are extrapolated to the position of a scintillator. To ensure an accurate extrapolation of the tracks, the segments are required to have at least one hit on each plane of the wire chamber. This results in an efficiency of $97.2 \pm 0.2\%$ in the central system, and $84.5 \pm 0.5\%$ in the forward system. Especially in the forward system, this efficiency is lower than the design efficiency as mentioned in section 3.2.3 due to dead channels.

²The segment can pass through multiple tubes in one plane due to a non-zero angle with the normal of the plane.

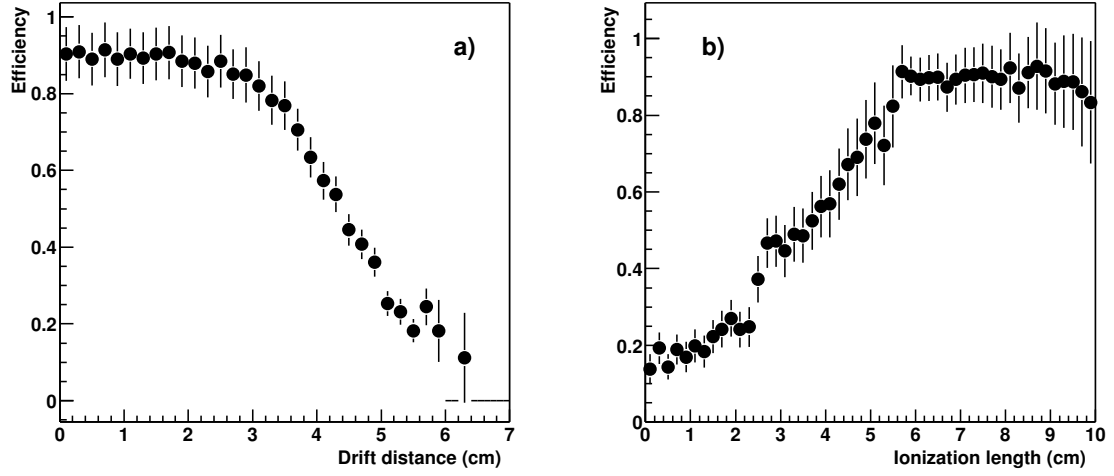


Figure 5.13: *PDT single hit efficiency in the data as function of the drift distance (a) and ionization length (b).*

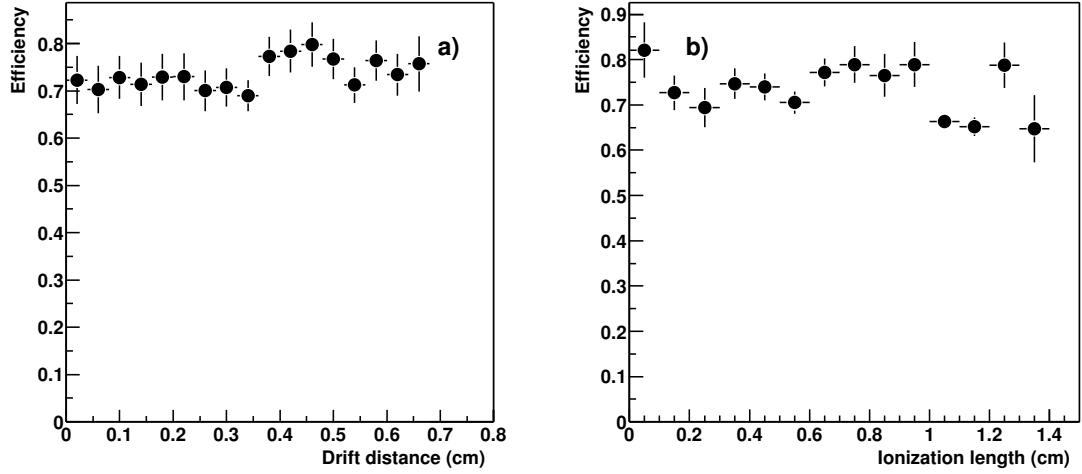


Figure 5.14: *MDT single hit efficiency in the data as function of the drift distance (a) and ionization length (b).*

Hit Residuals

The drift distance resolution, σ_{hit} , with which the PDT and MDT wire hits are measured can be determined by studying the residuals of the hits with respect to reconstructed segments. This is done using segments reconstructed with both B- and C-layer hits, and the requirement that the segment has at least 4 hits in one of the layers. This ensures that the segment has a large lever arm due to the distance between the B- and C-layer, and that the direction of the segment is determined primarily by the position and drift distances of the hits in the other layer. Since the hit system in the A-layer is the same as in the B- and C-layers, except for the number of planes, we assume a similar hit resolution for the A-layer as for the B- and C-layers. To calculate σ_{hit} for the B- and C-layers, we remove one of the hits of the segment in the layer that has the least number of hits, and refit the segment using the remaining hits. The distance of the refitted segment to the removed hit, subtracted from the true drift distance of this hit is the hit residual of that hit. This hit residual is further treated as not biased with respect to the reconstructed segment. However, the segment has an error associated with it, which is a function of the hit resolution and the number of remaining hits, namely:

$$\sigma_{seg}^2 = \frac{\sigma_{hit}^2}{N-1} \quad (5.15)$$

where σ_{hit} is the true hit residual for one hit, N is the original number of hits in the layer, and σ_{seg}^2 is the segment resolution. The width of the residual distribution, σ_{res} , can be written as:

$$\sigma_{res}^2 = \sigma_{hit}^2 + \sigma_{seg}^2 = \frac{N\sigma_{hit}^2}{N-1} \quad (5.16)$$

and consequently:

$$\sigma_{hit}^2 = \frac{N}{N-1} \sigma_{res}^2 \quad (5.17)$$

If we therefore plot the distribution of the hit residual for different values of N , we can determine the true hit residual. Figures 5.15 and 5.16 show this for PDT hits in the data and the Monte Carlo simulation³, and the results are summarized in table 5.3. The single hit resolution for PDT hits in the data is 0.45 cm, while in the simulation this is 0.08 cm. Clearly the Monte Carlo simulation underestimates the PDT hit resolution. This is caused mainly by the fact that the time-to-drift conversion used is not well known in the data. Furthermore, the Monte Carlo simulation uses an optimized value of the uncertainty on the drift time measurement. Figures 5.17 and 5.18 show the MDT hit residual distribution for different values of N for the data and the Monte Carlo simulation, and the results are summarized in table 5.4. In the data, the single MDT hit resolution is 1.1 mm. As can be expected, the Monte Carlo simulation also

³We used an inclusive $b\bar{b}$ sample of 4500 events.

underestimates this resolution, and gives a single hit resolution of 0.8 mm. In the data, the time to drift relation is an approximation of the true time to drift relation in the wire tubes, and is therefore less accurate. The smearing in the Monte Carlo simulation turns out to be insufficient to account for the detector resolution.

N	σ_{res} (cm)	σ_{hit} (cm)	N	σ_{res}	σ_{hit}
2	$0.67 \pm 1.1\text{e-}2$	$0.47 \pm 7.5\text{e-}3$	2	$0.11 \pm 8.2\text{e-}3$	$7.8\text{e-}2 \pm 5.8\text{e-}3$
3	$0.55 \pm 3.5\text{e-}3$	$0.45 \pm 2.9\text{e-}3$	3	$0.10 \pm 3.1\text{e-}3$	$8.5\text{e-}2 \pm 2.5\text{e-}3$
4	$0.52 \pm 9.3\text{e-}3$	$0.45 \pm 8.1\text{e-}3$	4	$9.6\text{e-}2 \pm 2.6\text{e-}3$	$8.3\text{e-}2 \pm 2.3\text{e-}3$
	weighted ave.	$0.45 \pm 4.0\text{e-}3$		weighted ave.	$8.1\text{e-}2 \pm 3.9\text{e-}3$

Table 5.3: Hit residuals for PDT hits in the data (left) and in the Monte Carlo simulation (right).

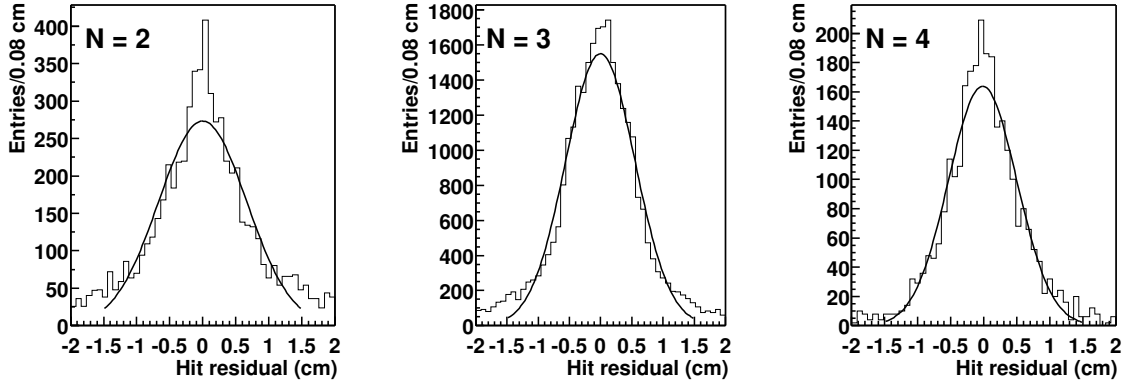


Figure 5.15: *PDT hit residuals in the data for $N=2, 3$ and 4 .*

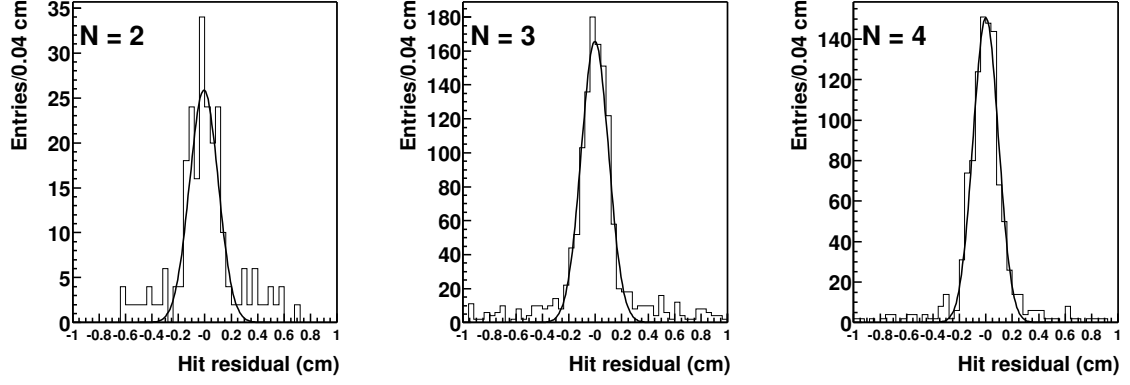


Figure 5.16: *PDT hit residuals in the Monte Carlo simulation for $N=2, 3$ and 4.*

N	σ_{res} (cm)	σ_{hit} (cm)	N	σ_{res}	σ_{hit}
2	$0.17 \pm 2.1\text{e-}3$	$0.12 \pm 1.5\text{e-}3$	2	$0.11 \pm 8.3\text{e-}3$	$7.8\text{e-}2 \pm 5.8\text{e-}3$
3	$0.15 \pm 8.6\text{e-}4$	$0.12 \pm 7.0\text{e-}4$	3	$0.10 \pm 2.1\text{e-}3$	$8.2\text{e-}2 \pm 1.7\text{e-}3$
4	$0.12 \pm 8.7\text{e-}4$	$0.10 \pm 7.5\text{e-}4$	4	$8.9\text{e-}2 \pm 1.2\text{e-}3$	$7.7\text{e-}2 \pm 1.0\text{e-}3$
	weighted ave.	$0.11 \pm 7.8\text{e-}4$		weighted ave.	$7.9\text{e-}2 \pm 1.4\text{e-}3$

Table 5.4: Hit residuals for MDT hits in the data (left) and in the Monte Carlo simulation (right).

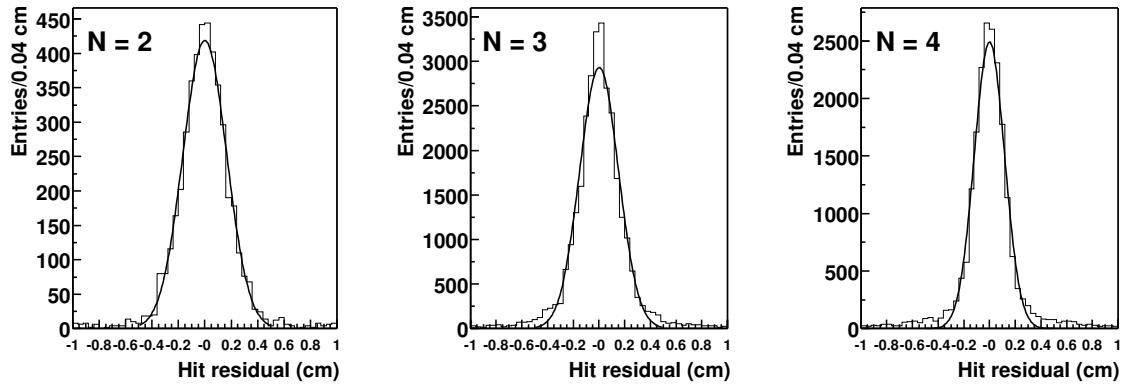


Figure 5.17: *MDT hit residuals in the data for $N=2, 3$ and 4.*

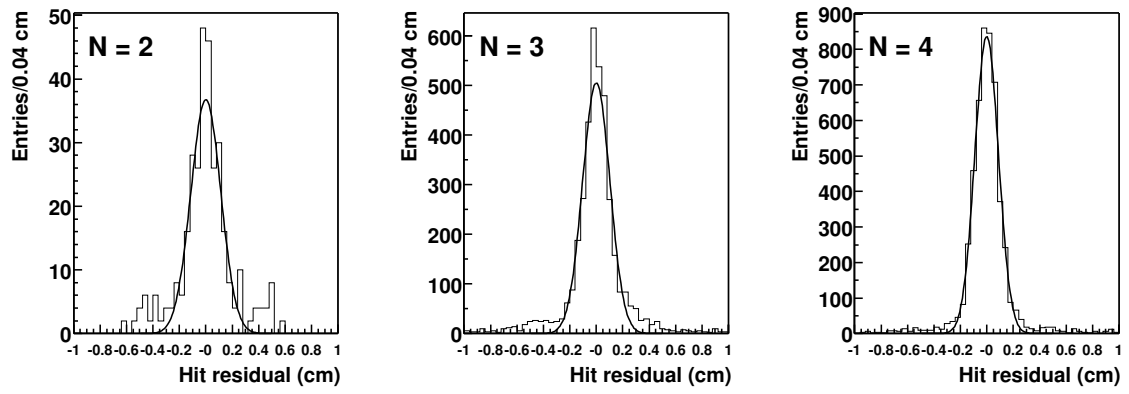


Figure 5.18: *MDT hit residuals in the Monte Carlo simulation for $N=2, 3$ and 4.*

5.3.2 Segment Reconstruction

The segment reconstruction finds track segments in each layer of the muon detector. Starting with the wire hits in each muon wire chamber, a pattern recognition algorithm is applied to reconstruct straight line segments. These line segments are then matched with present hits in nearby scintillators for an updated position and a time measurement. The algorithm can be separated in different steps:

1. Pattern recognition;
2. Segment fit;
3. Scintillator match;
4. B/C layer segment match;
5. Selection of the best segment.

Pattern recognition

The pattern recognition process is a recursive procedure, based on a linked-list algorithm in which straight line links between individual hits are made, and matched together to form a segment [31]. The pattern recognition is done in a local coordinate system, in which the wires are pointing along the z -direction, the wire tubes are stacked along the y -direction and the planes of the chamber are stacked along the x -direction (see figure 5.19). In the A-layer, where the chambers consist of 4 planes of tubes, the typical number of hits on a segment is 3 to 4. In the B- and C-layers, where the chambers consist of 3 planes of tubes, the typical number of hits is 2 to 3. At the start of the procedure, each driftcircle is assigned two hits that are located on the top and the bottom of the circle, to account for left/right ambiguities. Straight lines between the hits, further called links, are made between each pair of hits that conforms to the following requirements:

- The separation between the hits along the y -direction is less than δy (where δy is set by default to 20 cm, which is twice the tube width), to ensure that uncorrelated hits (i.e. hits that are not coming from the same segment) are not matched;
- The two hits are not on the same plane, except when one is at the top of a driftcircle while the other is at the bottom. This ensures that fake segments that are parallel to the planes are removed at an early stage. The exception permits those instances in which a track passes through two neighboring tubes in one plane.

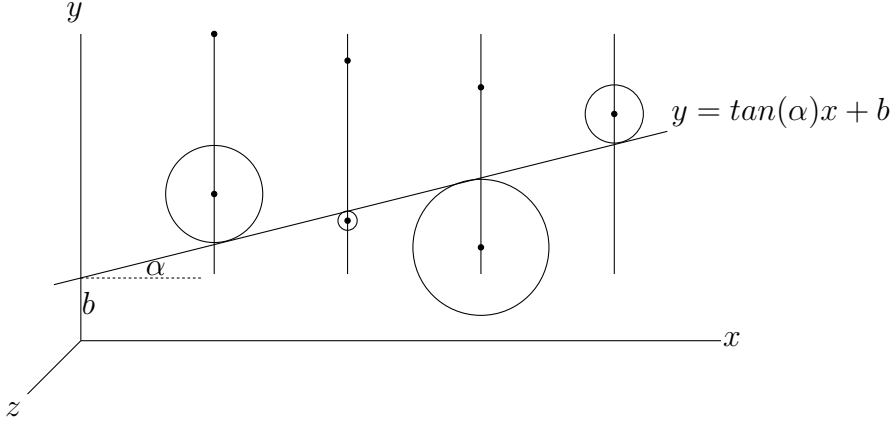


Figure 5.19: Schematic view of a typical collection of hits in a layer. The drift circles of the hits (the large circles) and the reconstructed segment (the diagonal line) are drawn, showing the local coordinate system in which the pattern recognition is performed. The wires are represented by the small open dots.

The direction of the link in the drift plane, α , is defined by the position of the hits used:

$$\tan(\alpha) = \left(\frac{y_2(\alpha) - y_1(\alpha)}{x_2(\alpha) - x_1(\alpha)} \right) \quad (5.18)$$

where x_i and y_i ($i = 1, 2$) are the positions of the hits, which depend on the drift time t_d and the angle of the link α according to:

$$x_{hit} = x_{wire} - n \cdot d(t_d, \alpha) \sin(\alpha) \quad (5.19)$$

$$y_{hit} = y_{wire} + n \cdot d(t_d, \alpha) \cos(\alpha) \quad (5.20)$$

with $n = \pm 1$ depending on whether the hit is on the top (+) or on the bottom (−) of the wire, and where $d(t_d, \alpha)$ is the drifttime to distance relationship. To approximate α in the first step, the direction of the link is estimated by a straight line from the origin of the detector (i.e. the nominal interaction point) to the position of the hit. With this angle, the positions of the hits are calculated with equations 5.19 and 5.20, and the direction of the link is calculated according to equation 5.18.

The links found in this initial step are matched together in a recursive pattern, in which the differences in angle and position of the links are compared to determine whether they belong to a straight line segment. Whenever two links are found to be compatible with a straight line segment, they are merged into a segment that contains all the hits of the two original links. This segment is fitted with the hits it contains to determine its angle and position (taking into account the angle dependence of the hits

on the segment). This procedure is repeated until all links have been attempted to be matched with all other links, thus creating segments.

Segment fit

The fit of the segment to the hits is performed in a (x', y') coordinate system in which the direction of the segment corresponds to the x' -axis. The origin of the coordinate system is placed at the center of gravity of the hits used in the fit. The shortest distance from each hit to the segment is now parallel to the y' axis, so that a straight line fit can be performed. The transformation from the (x, y) system to the (x', y') system first requires the calculation of the center of gravity, according to:

$$x_{cog} = \frac{1}{n} \sum_{i=1}^n x_i^{hit} \quad (5.21)$$

$$y_{cog} = \frac{1}{n} \sum_{i=1}^n y_i^{hit}$$

where the suffix i runs over all hits on the segment.

The hits on the segment are then rotated by the current angle of the segment, by:

$$\begin{pmatrix} x'_{hit} \\ y'_{hit} \end{pmatrix} = \begin{pmatrix} \cos(\alpha) & \sin(\alpha) \\ -\sin(\alpha) & \cos(\alpha) \end{pmatrix} \begin{pmatrix} x_{hit} - x_{cog} \\ y_{hit} - y_{cog} \end{pmatrix} \quad (5.22)$$

Then, a straight line can be fitted through the points (x'_{hit}, y'_{hit}) , with χ^2 defined as:

$$\chi^2 = \sum_{i=1}^n \left(\frac{y'_i - m'x'_i - b'}{\delta r} \right)^2 \quad (5.23)$$

where $m' = \tan(\alpha')$ is the slope of the segment in the (x', y') coordinate system, b' is the intersection with the y' axis and δr is the error on the drift distance of the hit. Differentiating χ^2 with respect to m' , and setting it to zero to find the minimum of χ^2 gives

$$D_{x'y'} - m'D_{x'^2} - b'D_{x'} = 0 \quad (5.24)$$

where

$$D_T = \sum_{i=1}^n \left(\frac{T}{\delta r^2} \right) \quad T = x', y', x'y', x'^2 \quad (5.25)$$

Differentiating with respect to b' results in

$$D_{y'} - m'D_{x'} - b' = 0 \quad (5.26)$$

Eliminating b' from above two equations results in the slope

$$m' = \frac{D_{x'}D_{y'} - D_{x'y'}}{D_{x'^2} - D_{x'}^2} \quad (5.27)$$

Solving these equations generally results in a non-zero value of m' and thus α' , changing the angle α of the segment. Hence, to calculate the proper angle of the segment, the above algorithm is repeated until the position and angle of the segment stabilize, which typically takes 4 iterations.

The errors on the position and angle of the segment are calculated in the rotated (x', y') system, where the covariance of the angle and the position is zero:

$$\sigma_{m'} = \sqrt{1 / (D_1 (D_{x'^2} - D_{x'}^2))} \quad (5.28)$$

$$\sigma_{b'} = \sqrt{D_{x'^2} / (D_1 (D_{x'^2} - D_{x'}^2))} \quad (5.29)$$

where

$$D_1 = \sum_{i=1}^n \left(\frac{1}{\delta r^2} \right) \quad (5.30)$$

Scintillator match

Initially, scintillator hits near the reconstructed segment are not taken into account in the fit, since they do not add significant positional information in the drift plane due to their physical size. However, in the coordinate along the wire, the size of the scintillators is comparable to the axial position resolution of the PDT hits. Also, as explained above, in the forward system the scintillators provide the only position measurement along the wire. Therefore, after the fit has converged and the direction and position of the segment have been calculated using the wire hits, present scintillator hits are matched to the segment by extrapolating the segment to the scintillator position in the drift plane of the wire hits. If a match with a scintillator hit is found, the segment is refitted, now taking into account the scintillator hit position information. For segments found in the FAMUS, the position of the scintillator along the wire provides information about the separation of the measured time of the MDT hit in drift time and axial time, improving the fit of the segment to the drift circles. The position of the segment is set to the center of the scintillator location, resulting in a resolution of about 7 cm. If no scintillator match is found for a FAMUS segment, the position of the segment is set to the center of the wire. The resolution is then equal to the length of the MDT wire, divided by $\sqrt{12}$, resulting in a resolution of typically 60-90 cm. In the WAMUS system, where the hits themselves provide a measurement of the position of the segment along the wire, the z -position of the segment is the weighted average of the z -positions of the hits (including the scintillator hit):

$$z = \frac{\sum_{i=1}^n \left(\frac{z_i}{\delta z} \right)^2}{\sum_{i=1}^n \left(\frac{1}{\delta z} \right)^2} \quad (5.31)$$

with error

$$\sigma_z = \frac{1}{\sum_{i=1}^n \left(\frac{1}{\delta z}\right)^2} \quad (5.32)$$

resulting in a typical resolution of 10 cm.

B/C Layer segment match

Segments are initially reconstructed in the individual layers of the muon system separately. Due to the absence of a magnetic field between the B- and C-layers, segments in the B- and C-layer are expected to be part of the same straight line segment, and can be matched as such. To this avail, each pair of reconstructed B- and C-layer segments found in the same octant and region is merged, and a new fit is performed using all hits on both segments. The old B- and C-layer segments are kept available for the selection of the best segment in the next step.

Selection of best segment

For a given group of hits, the algorithm finds multiple segments out of which the correct one has to be selected for further track reconstruction. This selection is based on the χ^2 of the fit, divided by the number of degrees of freedom. In the case that segments are reconstructed with more than 2 wire hits, the segment with the the lowest χ^2/ndf is chosen. For segments with only 2 wire hits, the segment that points best to the primary vertex is selected.

Segment Reconstruction Efficiency

The segment reconstruction algorithm requires the presence of at least two wire hits to reconstruct a segment. The reconstruction efficiency for these segments is extracted from the data sample using central tracks that are extrapolated to the muon system [29]. To avoid the correlation of the muon reconstruction efficiency with the Level 1 muon trigger efficiency due to double counting of the scintillator efficiency, we require the event to be triggered by the Level 1 muon trigger and a scintillator hit in both the A-layer and the B/C-layer that matches the extrapolated track. The A-layer segment reconstruction efficiency is calculated by extrapolating central tracks to the BC-layer and matching these tracks with present reconstructed BC-segments (see figure 5.20a). These BC-segments are required to consist of at least 3 wire hits in addition to the scintillator hit. The time measured with the scintillator hit is required to coincide with the trigger gate to reduce the contamination by cosmic rays in the sample. Reconstructed segments present in the A-layer, with at least 3 wire hits, are matched with this extrapolated track in the drift plane to calculate the reconstruction efficiency of A-layer segments. The efficiency found in this manner for A-layer segments is shown in figure 5.21 to be $92.7 \pm 0.9\%$ in the central region, and $91.5 \pm 0.6\%$ in the forward region, where the errors are statistical only. The drop at $|\eta| \approx 1$ is caused by the overlap region between the central system and the forward system; the drop at $\phi \approx 4.6$ in the central system is due to the reduced coverage of the A-layer in that region.

A similar method is applied to measure the reconstruction efficiency of BC-layer segments. Central tracks are propagated to the muon system, where they are matched with present A-layer segments, with at least 2 wire hits and a scintillator hit, as well as with the scintillator hit in the B- or C-layer (see figure 5.20b). In the case of a match, the central tracks are matched with possible reconstructed BC-layer segments with at least 3 wire hits. This yields an efficiency of $90.6 \pm 2.7\%$ in the central region, and $97.5 \pm 1.2\%$ in the forward region, as illustrated in figure 5.22. These results are summarized in table 5.5.

The efficiencies of the segment reconstruction algorithm in the Monte Carlo simulation is extracted using the same procedure. Figure 5.21 shows the reconstruction efficiency for A-layer segments, figure 5.22 for BC-layer segments. The efficiencies found from the Monte Carlo simulation are compatible with the efficiencies found in the data, except for the central efficiency of the BC-layers. This can be attributed to an overestimation of the efficiency of the B- and C-layers in the simulation, and effects of worse alignment in the data.

	Data	Monte Carlo
A-layer, central	$92.7 \pm 0.2\%$	$90.8 \pm 0.5\%$
A-layer, forward	$91.5 \pm 0.1\%$	$91.1 \pm 0.6\%$
BC-layer, central	$90.6 \pm 0.6\%$	$95.8 \pm 0.6\%$
BC-layer, forward	$97.5 \pm 0.1\%$	$98.5 \pm 0.3\%$

Table 5.5: *Segment reconstruction efficiencies. The efficiencies for Monte Carlo simulation are calculated by applying the same algorithm on the Monte Carlo simulation as on the data.*

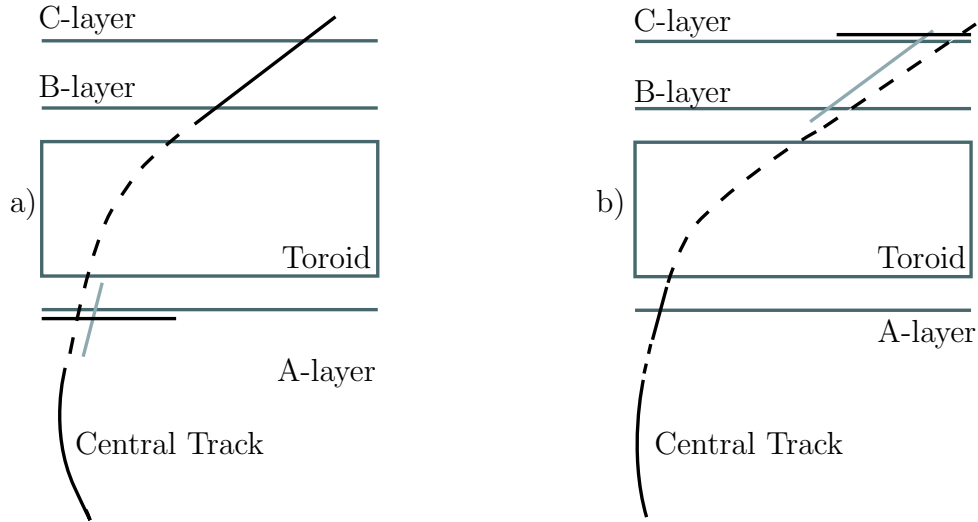


Figure 5.20: *Illustration of the calculation of the segment reconstruction efficiency. Figure a) shows the calculation of the A-layer segment reconstruction efficiency, using an extrapolated central track (curved black line) matched with a reconstructed BC-layer segment (straight black line) and an A-layer scintillator hit (horizontal black line). The dashed line represents the propagation of the central track through the toroid, while the gray diagonal line represents a possible reconstructed A-layer segment. Figure b) shows the calculation of the BC-layer segment reconstruction efficiency, using an extrapolated central track matched with a reconstructed A-layer segment and a C-layer scintillator hit.*

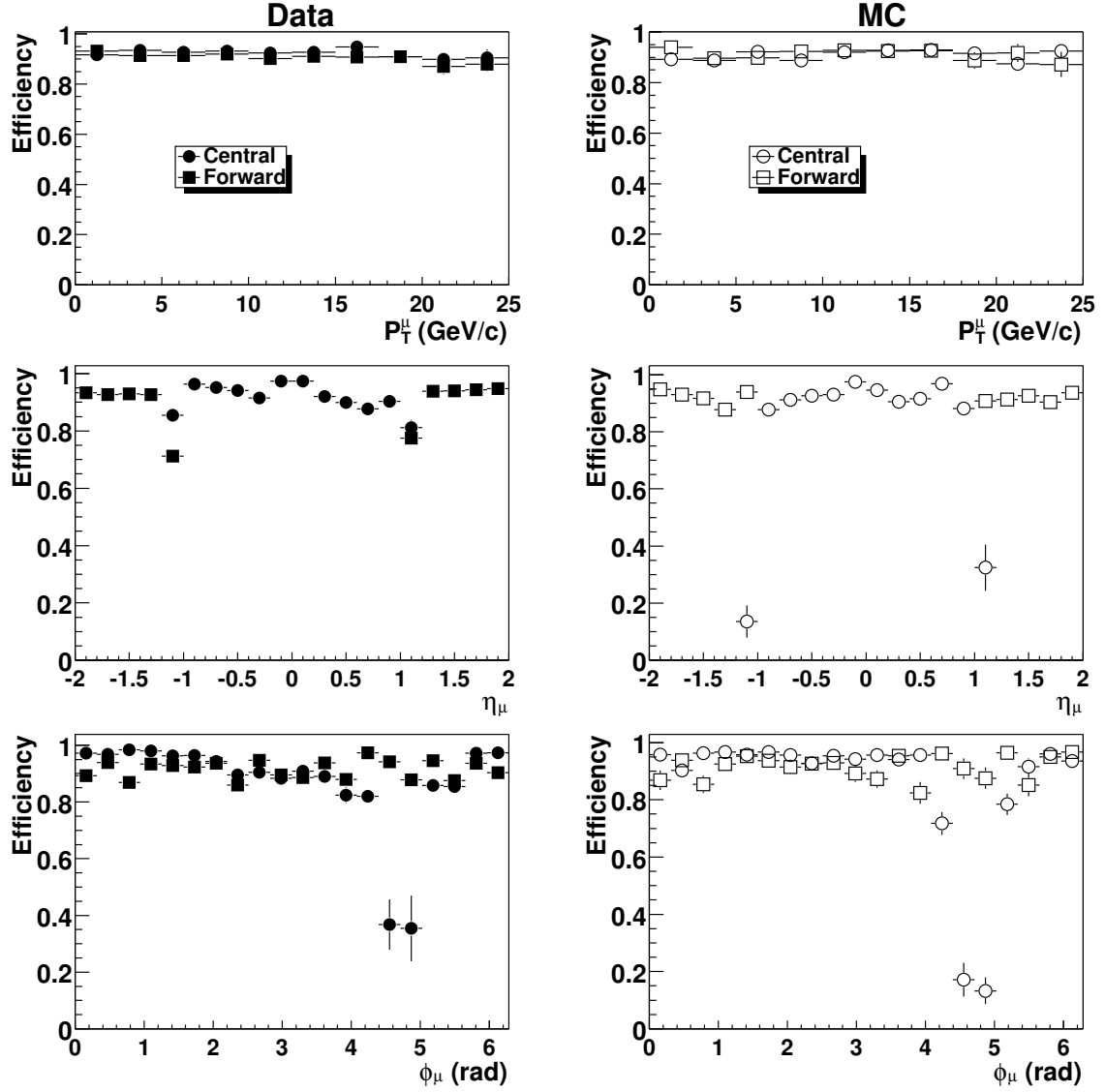


Figure 5.21: A-layer efficiency as a function of p_T , η and ϕ for data on the left side, and for the Monte Carlo simulation on the right side. The central region efficiency is displayed by circles, the forward region efficiency by squares.

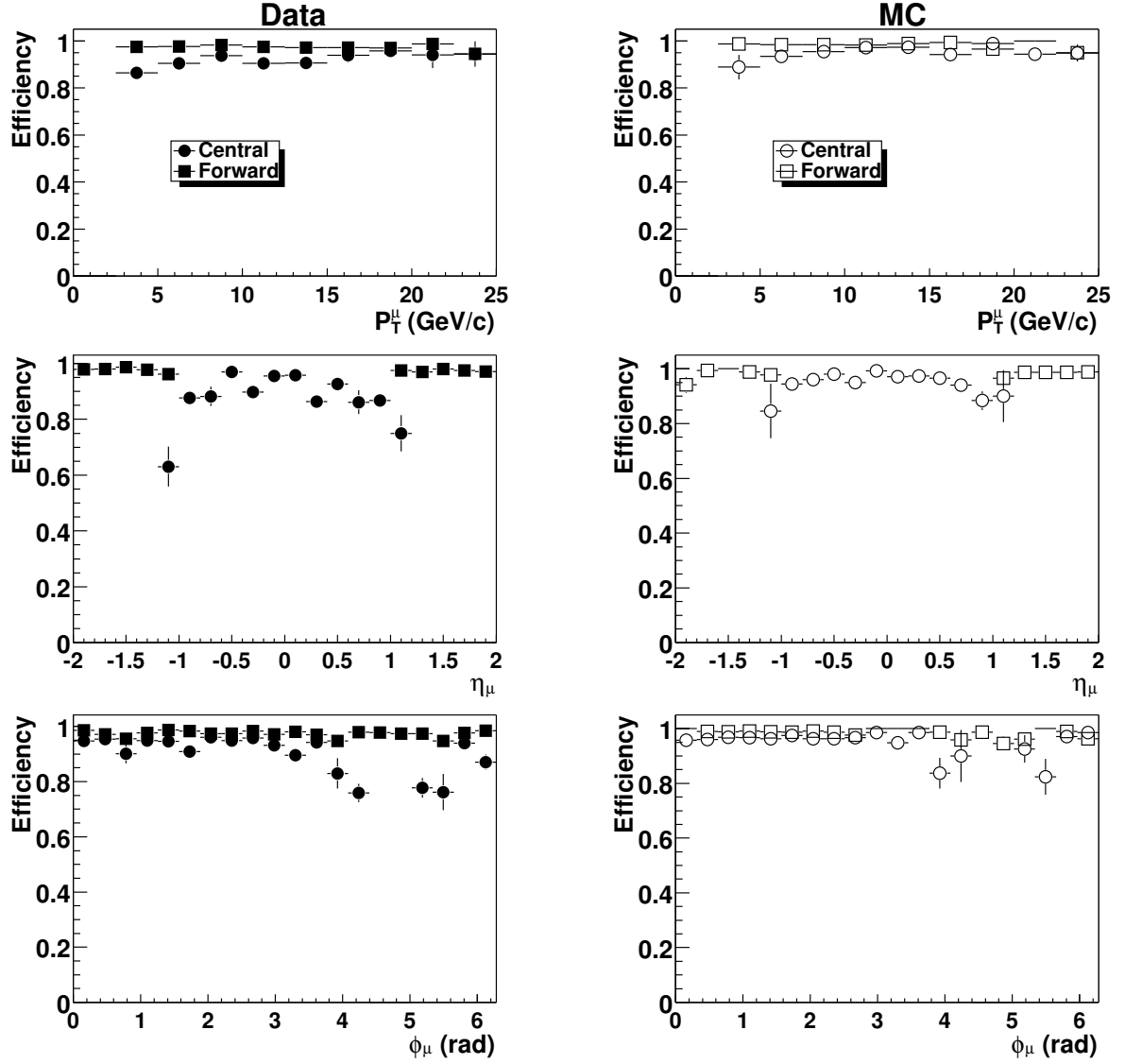


Figure 5.22: BC-layer efficiency as a function of p_T , η and ϕ for data on the left side, and for the Monte Carlo simulation on the right side. The central region efficiency is displayed by circles, the forward region efficiency by squares.

Segment resolution

The performance of the algorithm in terms of the resolution of reconstructed segments is evaluated using the same Monte Carlo sample as used in section 5.3.1, in which the reconstructed segments are compared with the muons in the Monte Carlo simulation as they pass the different muon layers. Figure 5.23 shows the resolution of the reconstructed segments in the central system in the drift angle α , the azimuthal angle ϕ , the position in the drift plane y and the position along the wire z . The α distribution is shown separately in two distributions for single layer segments, which typically have 3 or 4 wire hits, and BC-layer segments, which typically have 6 or more hits and a large lever arm. The resolution on the angle α for a single layer is 7.8 mrad, and 1.2 mrad for BC-layer segments. The other distributions also show a resolution corresponding the design limits: 1 mm for the local y coordinate and 80 mrad for the ϕ direction of the segment [24]. Figure 5.24 shows the pull distributions for the same variables, demonstrating a correct assignment of errors to the segments. Figure 5.25 shows the position and direction resolution for reconstructed segments in the forward regions. Again, the α distribution is split for single layer and BC-layer segments, showing a resolution of 11 mrad and 1.2 mrad respectively. The position distributions are compatible with the design limits of approximately 0.7 cm for the local y coordinate, and 80 mrad for the ϕ direction [19]. The pull distributions are displayed in figure 5.26, indicating correct error assignments to the reconstructed segments.

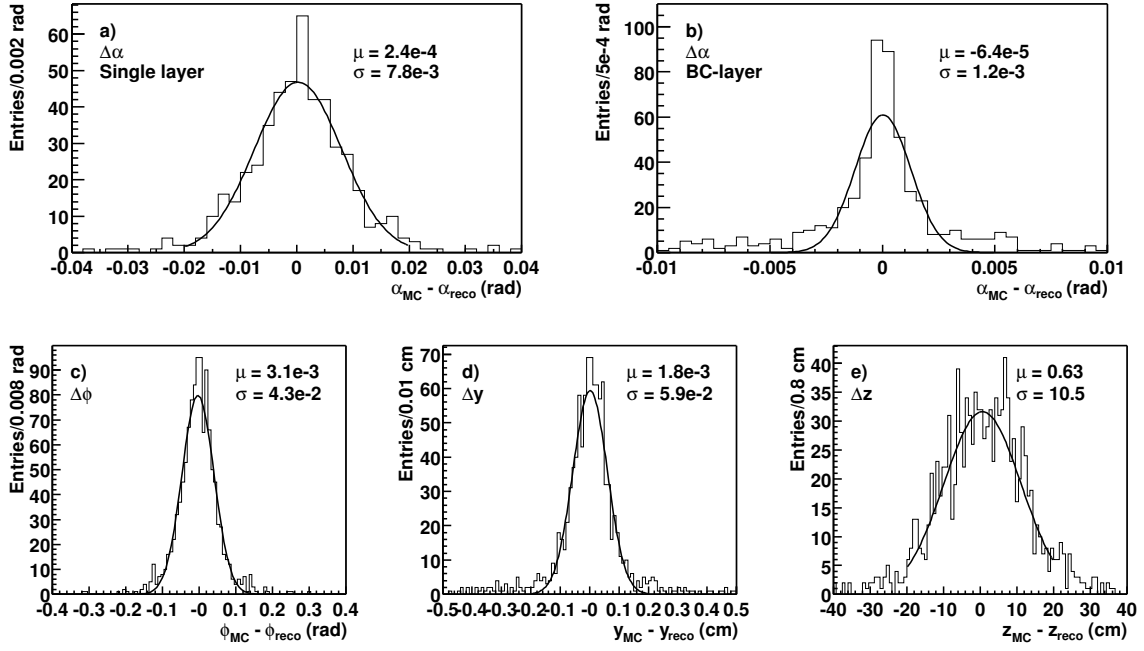


Figure 5.23: Segment reconstruction resolutions in α , ϕ , y and z in the central system.

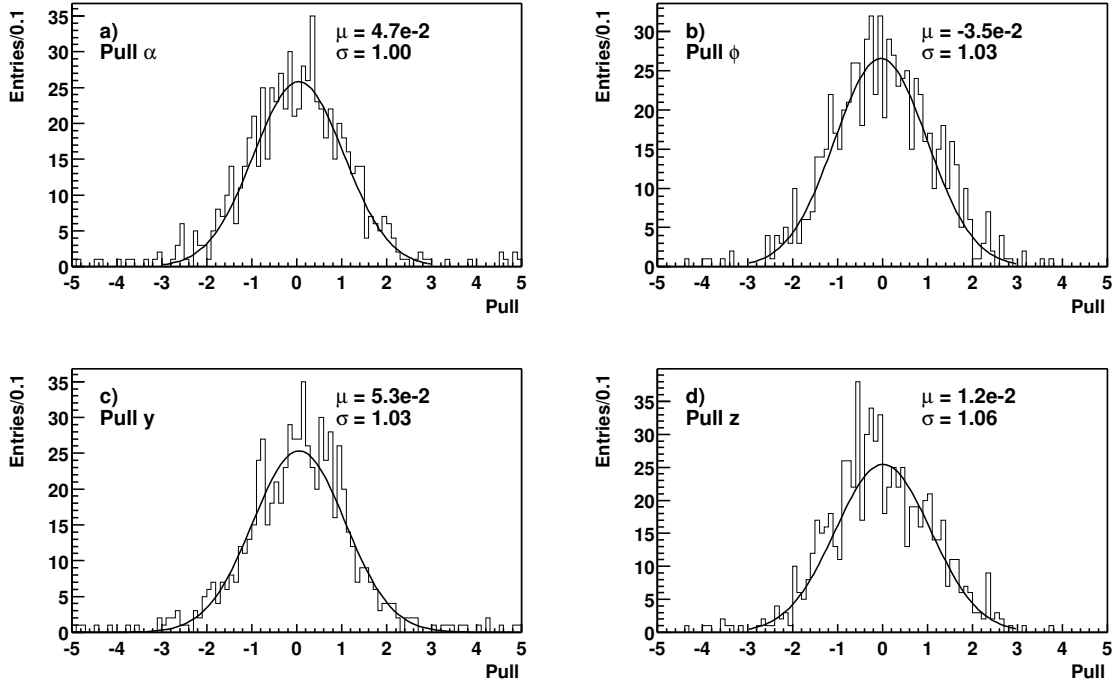


Figure 5.24: Pull distributions for α , ϕ , y and z in the central system.

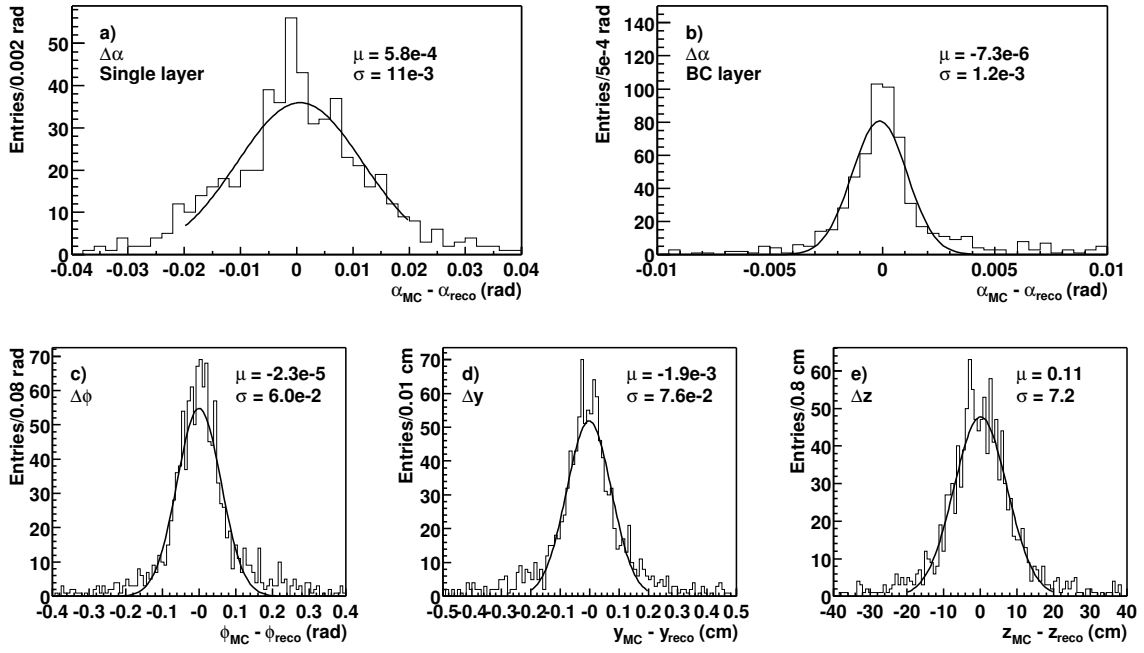


Figure 5.25: Segment reconstruction resolutions in α , ϕ , y and z in the forward system.

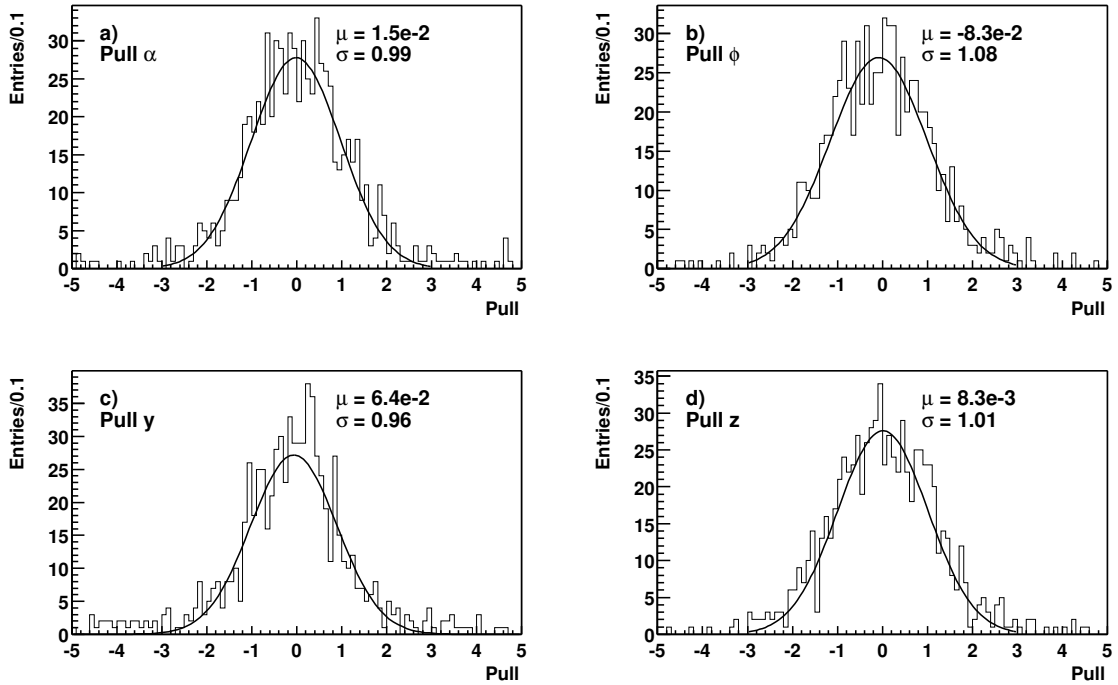


Figure 5.26: Pull distributions for α , ϕ , y and z in the forward system.

5.3.3 Local Track Reconstruction

A local track is a track that is measured by the muon system only, and not necessarily matched with a track reconstructed in the central tracker. The local track reconstruction matches segments in the A-layer in front of the toroid with segments in the B- and C-layers, before performing a fit to determine the momentum of the particle [12]. The match of the segments before and after the toroid is made by relating the directions of the segments in the global directions ϕ and θ with their global positions. In the case of a match, a first estimation of the momentum is made by comparing the angles in the drift plane of the two segments (see figure 5.27):

$$P_{drift} = \frac{0.3BD}{|\tan \theta|} \quad (5.33)$$

where P_{drift} is the momentum in GeV/c in the drift plane perpendicular to the wire direction⁴, B is the magnetic field in the toroid (1.8 Tesla), D is the distance in meters that the particle traverses through the toroid and θ is the angle difference between the two segments. Using the initial parameters from this estimation, a non linear fit is performed to find the best momentum compatible with the positions and directions of the two segments. Starting with the position of the BC segment, the fit propagates the track back stepwise through the toroid to the A-layer along a circular helix path, accounting for energy loss in the toroid at each step, and taking into account multiple scattering at two planes in the toroid.

Local muon fit efficiency

The reconstruction efficiency of the fit algorithm is measured by using extrapolated central tracks that have a matching A-layer and a matching BC-layer segment. The spatial matches used between the central track and the segments are the same as the ones used to calculate the respective segment reconstruction efficiencies. The local muon efficiency is now calculated by dividing the number of muon tracks that pass the quality and kinematic cuts, and originate from the segments matched to the central track, by the number of central tracks with matching segments. Figure 5.28 shows the efficiency of the track fitting algorithm in both the data and the Monte Carlo simulation; table 5.6 summarizes the results. The fit efficiency in the central system can be said to be on the low side. This can be attributed to the angle resolution of the segments reconstructed in the data, and to the fact that the muon fit only uses the segment with the best χ^2 , which may not always be the correct segment. If

⁴This is the same plane in which the drift angle α is calculated in the segment reconstruction; therefore, P_{drift} is not equal to p_T but instead $P_{drift} = p_T \cos \phi'$, where ϕ' is $\phi \bmod \frac{\pi}{4}$.

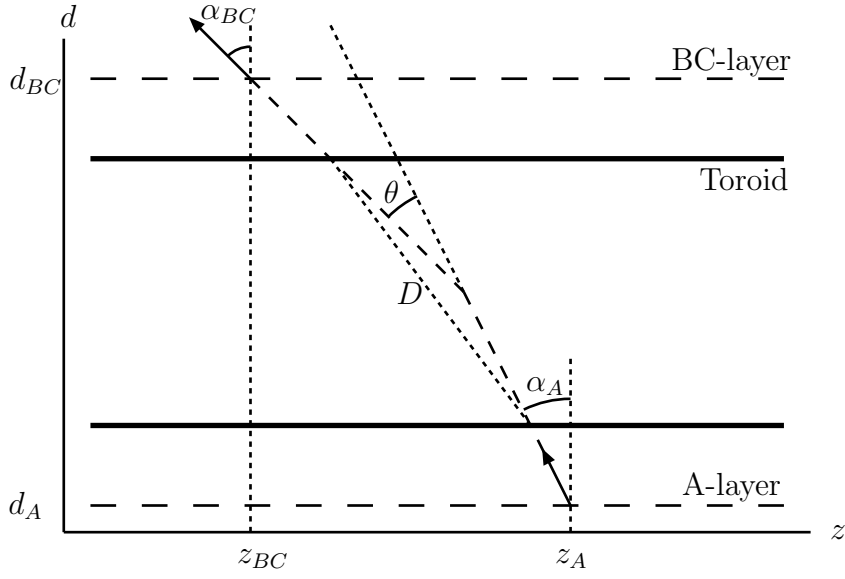


Figure 5.27: First estimation of track momentum by calculating the angle θ . d is the x or y coordinate, depending on the octant of the segments.

two segments are not compatible with a muon track, they can not be fitted into a track, which causes the inefficiency. The Monte Carlo simulations overestimates the fit efficiency if compared with the data, especially in the bottom octants ($3.8 < \phi < 5.3$). This can be attributed to the fact that the Monte Carlo simulation uses an ideal geometry, while the data is reconstructed with a less well aligned geometry.

Scintillator efficiency

Before we can proceed with calculating the final muon reconstruction efficiency, we have to correct for the fact that we required the presence of scintillator hits, which was done to avoid biases with the calculation of the trigger efficiency. If the Level 1 muon trigger fired, this means that both A- and B- or C-layer scintillators are present

	Data	Monte Carlo
Fit efficiency central	$55.3 \pm 0.2\%$	$60.0 \pm 1.4\%$
Fit efficiency forward	$74.6 \pm 0.4\%$	$79.7 \pm 1.0\%$

Table 5.6: Muon track fit efficiency. The efficiencies for Monte Carlo are calculated by applying the same algorithm on the Monte Carlo as on the data.

and located within a Level 1 road. This does not mean that they are also matched to a muon track in the reconstruction. Thus, we have to calculate the efficiency that the trigger fired, and that both scintillators are matched with the muon track. This efficiency is calculated from the data by selecting events for which the muon trigger fired and a central track is present that matches with a muon track. This correction then represents the efficiency of matching two scintillator hits that are located in one trigger road, and therefore fire the trigger, to a reconstructed muon track. The muon track is required to have at least 2 wire hits in the A-layer, at least 3 wire hits in the BC-layer and a converged fit. The scintillator correction is then calculated as:

$$\epsilon_{\text{scintillator}} = \frac{\text{Number of muon tracks with matching scintillator hits}}{\text{Number of muon tracks}} \quad (5.34)$$

This results in an efficiency of $94.1 \pm 0.4\%$ in the central region, and $99.5 \pm 0.1\%$ in the forward region. This correction is calculated in the Monte Carlo simulation in a similar fashion, except that the requirement that the trigger fired is dropped. This results in a correction of $88.6 \pm 1.1\%$ in the central region, and $92.0 \pm 1.0\%$ in the forward region. The correction is lower in the Monte Carlo simulation than in the data, due to the fact that we do not require a fired trigger, and the scintillator hit efficiency is folded into the resulting correction.

Overall muon reconstruction efficiency

Accounting for all the effects discussed above results in a reconstruction efficiency of $43.7 \pm 0.8\%$ and $66.2 \pm 0.3\%$ in the central and forward region respectively. In the Monte Carlo simulation these numbers are $46.2 \pm 0.2\%$ and $65.8 \pm 1.4\%$ (see figure 5.29 and table 5.7). To validate the algorithm that measures the efficiency to find a reconstructed muon that passes the muon identification cuts, it is also extracted from the Monte Carlo truth information. We count the number of produced Monte Carlo muons, and check if there is a reconstructed muon present in a cone of $\delta R < 0.3$. This results in an efficiency of $44.0 \pm 0.5\%$ in the central system, and $62.1 \pm 0.7\%$ in the forward system. The difference between the result of the algorithm applied on the Monte Carlo simulation and the result from the Monte Carlo truth, 2.2% and 3.7%, is taken as the systematic error on the measurement of the muon track reconstruction efficiency.

	Data	Monte Carlo	Monte Carlo Truth
Reconstruction efficiency central	$43.7 \pm 0.8\%$	$46.2 \pm 2.0\%$	$44.0 \pm 0.5\%$
Reconstruction efficiency forward	$66.2 \pm 0.3\%$	$65.8 \pm 1.4\%$	$62.1 \pm 0.7\%$

Table 5.7: Muon track fit and overall reconstruction efficiencies. The efficiencies for Monte Carlo are calculated by applying the same algorithm on the Monte Carlo as on the data; the efficiency in the Monte Carlo Truth column are calculated from the true Monte Carlo information.

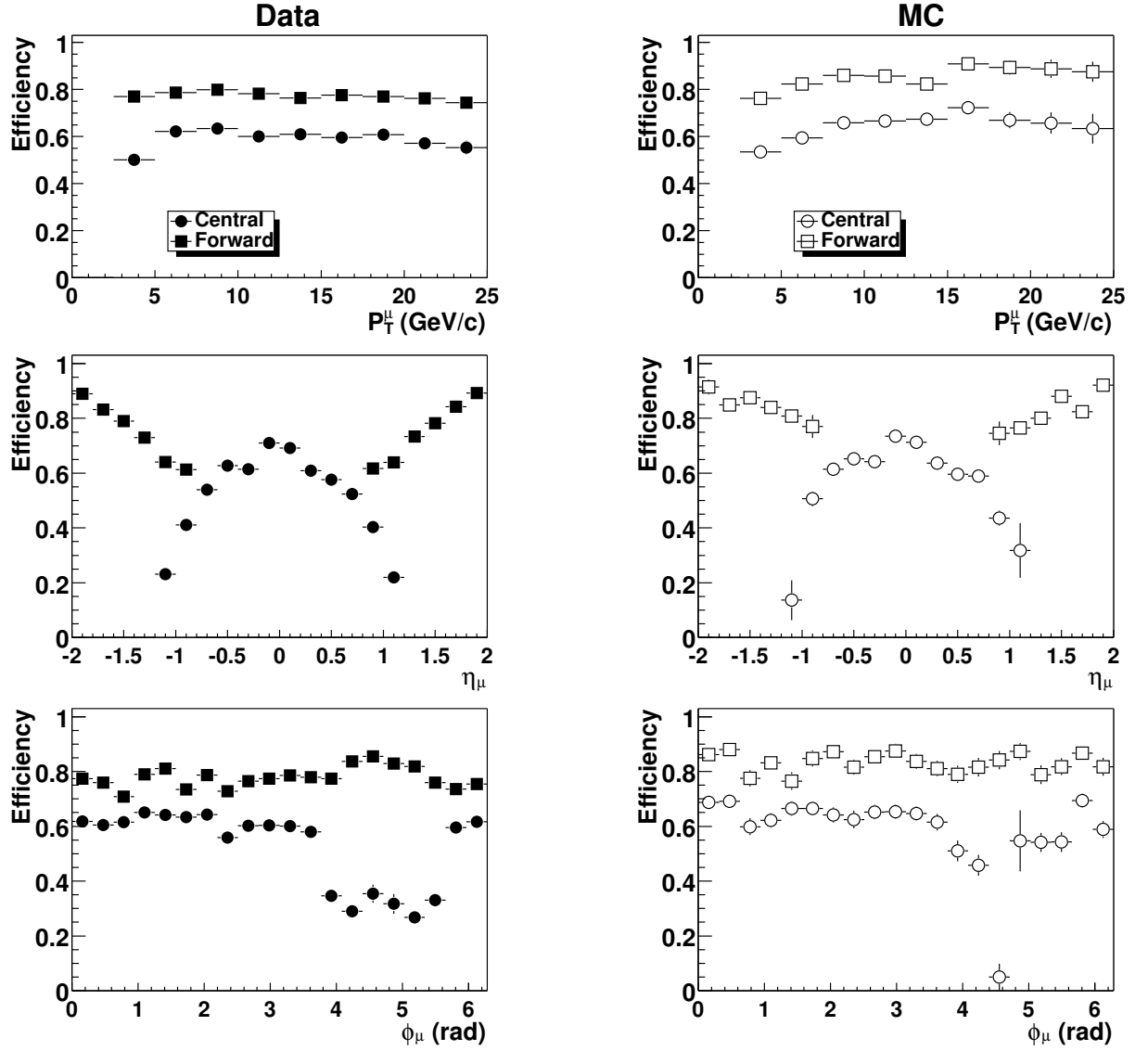


Figure 5.28: Efficiency as a function of p_T , η and ϕ for fitting a muon track from two present segments

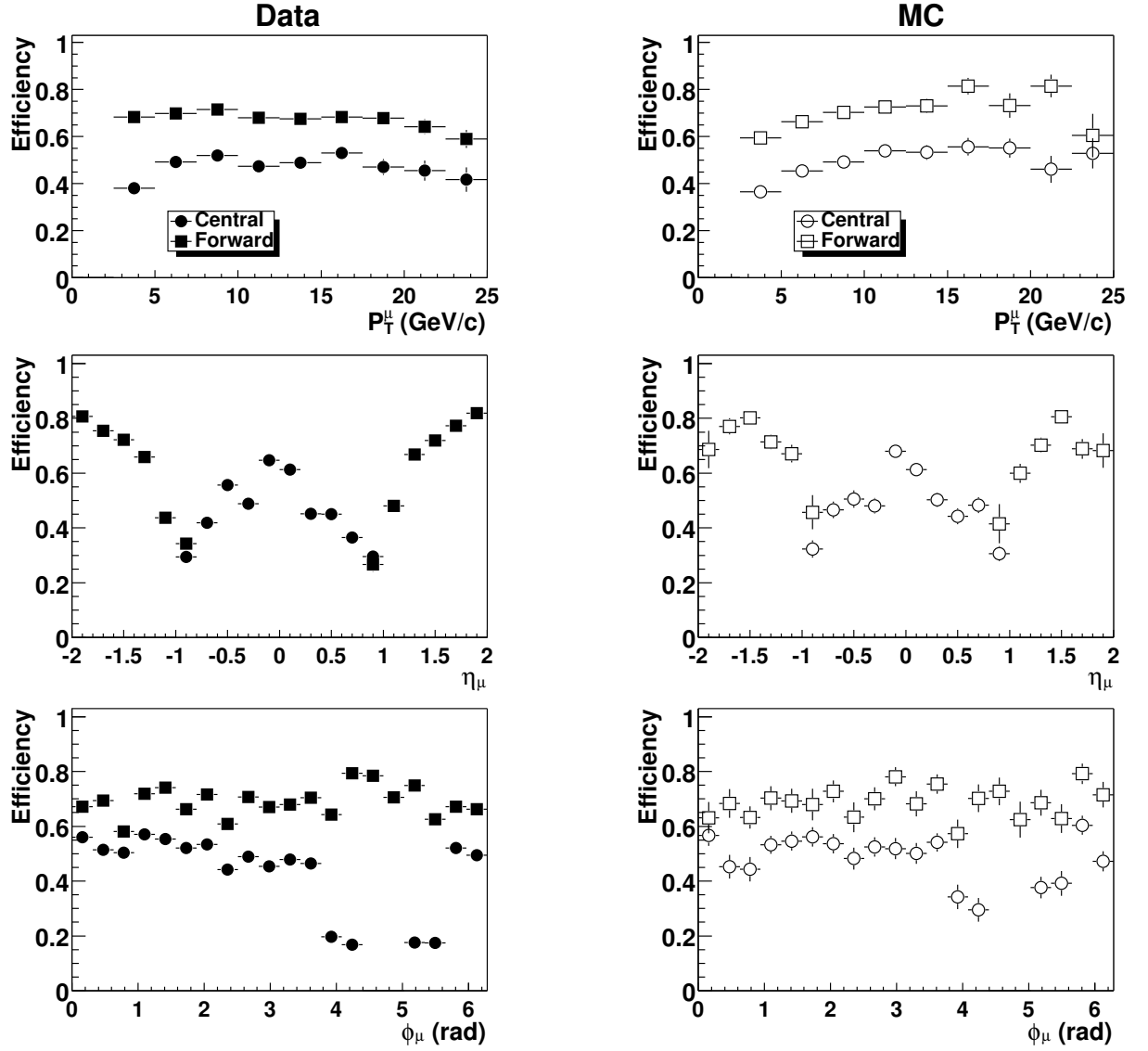


Figure 5.29: Total efficiency to reconstruct a local muon track as function of p_T , η and ϕ .

Local muon resolution

The resolution of the muon track momentum measurement is calculated by using central tracks. These tracks are propagated to the A-layer of the muon system, where they are matched with tight⁵ muon tracks. Since the p_T resolution of central tracks is significantly better, approximately 5% in the p_T range of muons in the sample (see figure 3.5), we can use these tracks to determine the resolution of the local muon track. A data sample of isolated muons is divided in different bins of muon p_T . For each bin we produce the distribution of:

$$\delta = p_T^C \left(\left(\frac{Q}{p_T} \right)^C - \left(\frac{Q}{p_T} \right)^L \right) \quad (5.35)$$

with the C superscript denoting central tracks and the L superscript denoting local muon tracks. If we now fit a gaussian shape to the distributions of δ , the width of the distribution represents the resolution of the local muon in that p_T^μ bin. Figure 5.30 shows this resolution Δ of the local muon track momentum for data, as well as for the Monte Carlo simulation, where

$$\Delta = \sigma(\delta) \quad (5.36)$$

The difference between the two resolutions is obtained by subtracting in quadrature, and is displayed by the gray dotted line. The significantly worse resolution in data can be attributed to the larger hit residuals in the data, leading to a degradation of the p_T resolution of the fitted local muon track. An additional effect is caused by the fact that the Monte Carlo simulation uses an ideal description of the muon detector. The detector description used to reconstruct the data is based on survey data with no further alignment, which is only accurate to a number of millimeters.

The direction resolution in η and ϕ of the muon tracks is also measured using central tracks. To estimate the η resolution of the muon tracks, central tracks are propagated to the A-layer, and matched with tight muons in p_T and ϕ . The ϕ resolution is measured in a similar fashion. These resolutions are shown in figure 5.31 for data and the Monte Carlo simulation. The η resolution of the Monte Carlo simulation is better than the η resolution in the data. This is again due to the underestimation of the p_T resolution in the Monte Carlo simulation. Smearing the p_T of the local muon tracks in the Monte Carlo simulation results in similar η resolutions in the simulation as in the data, due to the fact that both the p_T and the η depend on the angle of the A-layer segment (α_A). If we smear the radial component of this angle (i.e. the p_T), while keeping the p_z component constant, this results in proper corrections for p_T and η . The ϕ resolution in the data is slightly worse than the resolution in the Monte Carlo simulation. We smear

⁵See section 6.1

the ϕ direction of the local muon tracks in the Monte Carlo simulation by keeping p_T constant and smearing p_x and p_y .

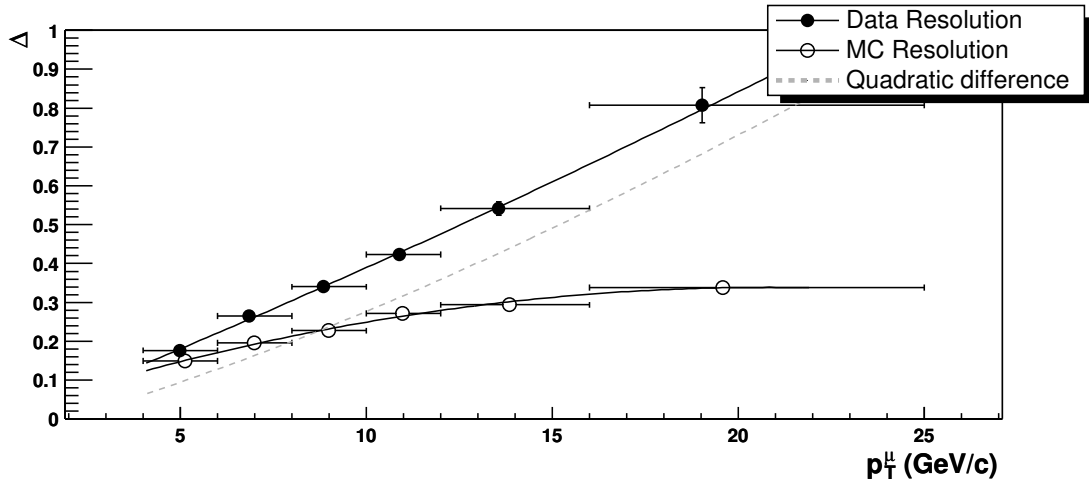


Figure 5.30: Muon momentum resolution as function of p_T^μ . The solid lines are 2nd order polynomials, fitted to the points. The dotted line is the difference between the two fits, obtained by subtracting in quadrature.

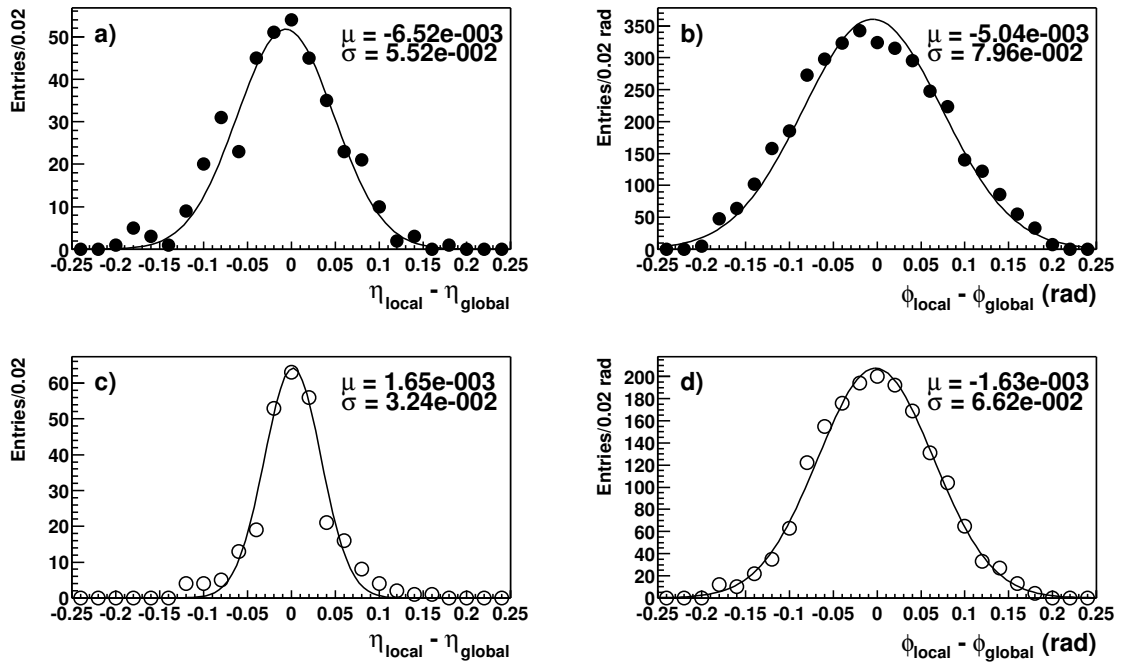


Figure 5.31: Muon direction difference in a) $\eta_{\text{local}} - \eta_{\text{global}}$ and b) $\phi_{\text{local}} - \phi_{\text{global}}$. For the Monte Carlo simulation the same quantities are shown in c) and d).

5.4 DØVE

DØVE (DØ Visualization Environment) is the DØ specific implementation of an ATLAS package called ARVE (Atlas Reconstruction and Visualization Environment) [6]. Originally used primarily as a graphical debugging tool for reconstruction software and visualization of detector geometries, it has evolved into a light weight event display which is now used, among other things, as a monitoring tool for online data taking, as well as a public display of events [7].

To display its objects, DØVE uses two main interfaces: Scenes and Representations. A Scene is anything that outputs information to the user, be it text, graphical or output to a file. For each such output, a different implementation, inheriting from the Scene interface, has to be implemented. Representations are wrappers around non-graphical objects which use the properties of those objects to define a graphical representation of that object that can be drawn on a Scene. Both classes are managed by the DisplayControl class that holds one or more Scenes and to which multiple Representations can be added. Finally, the DØVE singleton handles the DisplayControl, and governs the internal graphical event loop. This event loop is separate from the event loop of the DØ reconstruction framework. After each event has been processed by the DØ framework event loop, DØVE starts its own event loop in which the event is drawn on the Scene. Only when the DØVE event loop is terminated by the user, control is returned to the DØ framework.

Currently, representations for all subdetectors, except for the preshowers and forward proton detectors are implemented, as well as representations of reconstructed physics objects. The central tracker representation displays the geometry, hits and reconstructed central tracks. The calorimeter is represented by displaying cells with high enough energy, as well as by a lego plot. The representation of the muon system displays a wire frame of all detector elements in addition to drift circles for the wire hits and highlighted scintillators when hit.

A detail of the DØVE event display is shown in figure 5.32. Here, the Scene shows representations of the central muon chambers, reconstructed PDT hits and two fitted segments with matched scintillator hits.

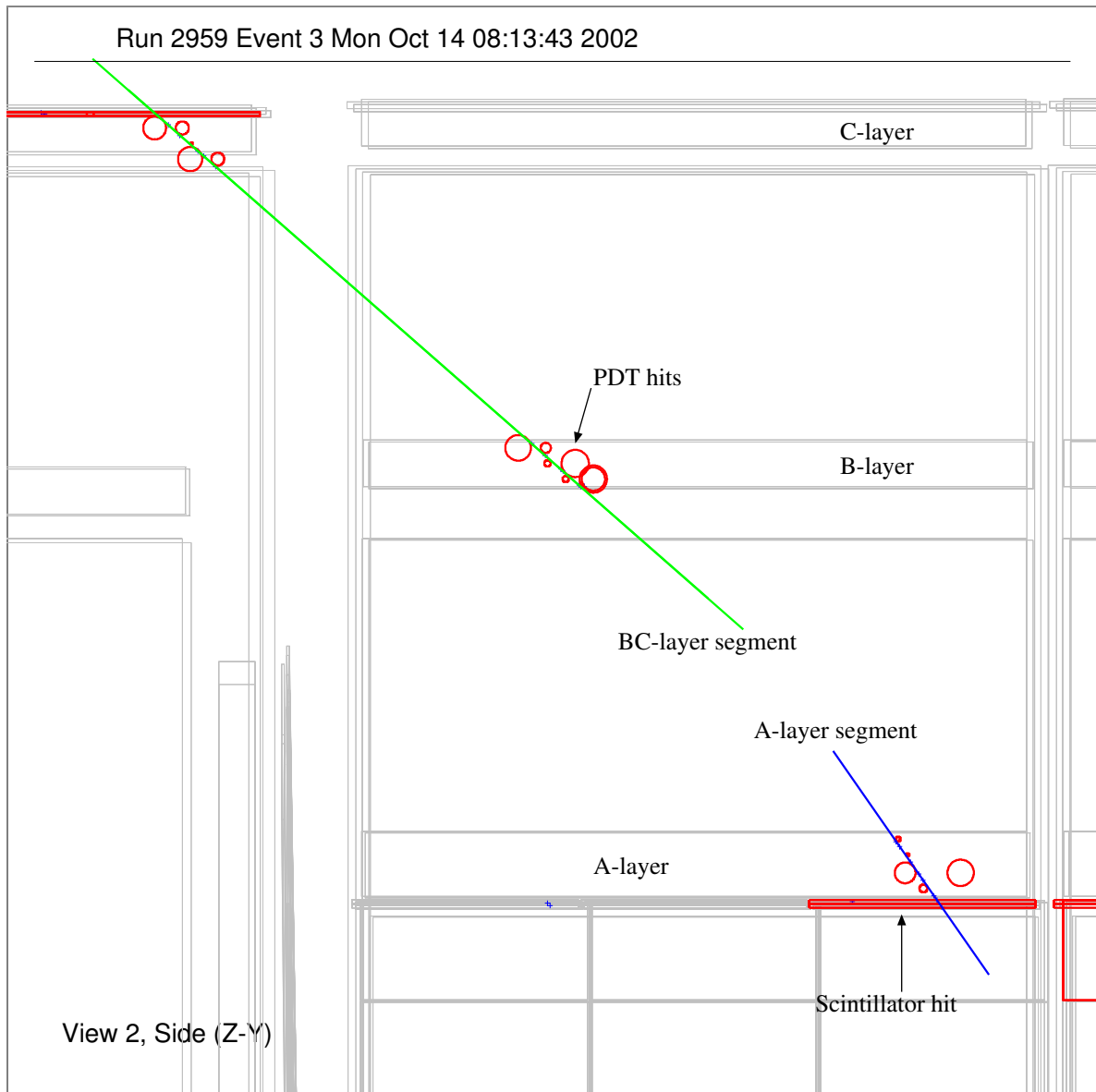


Figure 5.32: *DØve* display of a reconstructed muon track

Chapter 6

Event Selection

This analysis uses data taken with the DØ detector in the period February 28th until May 10th. The sample is divided in 4 parts, with each part corresponding to a specific trigger setting. Events in the sample are further selected on trigger, physics and quality criteria, namely:

- The run is qualified as good in the run quality database;
- A muon + jet Level 1 trigger requirement, *mulptxatxx_CJT5*, as described in section 4.4;
- The presence of a reconstructed muon and a reconstructed jet, with the additional constraint that the muon lies in a cone of radius $\delta R(jet, \mu) < 0.7$ around the jet axis, where $R = \sqrt{(\Delta\eta)^2 + (\Delta\phi)^2}$.

Table 6.1 lists the resulting data sample, containing 361037 events and corresponding to a total integrated luminosity of 3.4 pb⁻¹.

Trigger	Number of events	Integrated luminosity (nb ⁻¹)
global_CalMuon4.20	92900	862.7
global_CalMuon5.00	33201	331.1
global_CalMuon5.01	209190	2003
global_CalMuon5.10	25746	246.0
Total	361037	3442.8

Table 6.1: *Data sample used in the analysis*

6.1 Muon Identification

Due to the low reconstruction efficiency of tracks in the central tracking system during most of the data taking period, the standard muon reconstruction and identification can not use the central tracking, but has to rely solely on the information of the muon system. To ensure a reasonable momentum and direction measurement of the muon, it is required that the muon passes all three layers and hit a minimum number of detector components in these layers:

- At least 2 wire hits in the A-layer;
- At least 1 matching scintillator hit in the A-layer;
- At least 3 wire hits in the combined B- and C-layer;
- At least 1 matching scintillator hit in the B- or C-layer.

In addition, the fit of the A and B/C layer segments is required to converge. Furthermore, kinematic cuts are applied to the muon:

- $p_T^\mu > 4 \text{ GeV}/c$, to be well above the implicit cut of around $3 \text{ GeV}/c$ that a muon requires to penetrate the iron core of the muon toroid
- $|\eta_\mu| < 0.8$, to avoid the overlap regions between the forward and central system at $|\eta| \approx 1$.

Figure 6.2 shows the p_T , η and ϕ distributions of the muon after applying the above selection criteria. Even though the η distribution is symmetric around $\eta = 0$, as expected, it falls rapidly. This can be explained by the combined effect of the L1 trigger efficiency (see figure 4.5) and the reconstruction efficiency (see figure 5.29). The ϕ distribution clearly shows the hole in the detector at $\frac{5\pi}{4} < \phi < \frac{7\pi}{4}$, as well as the octant boundaries at $\phi = \frac{\pi}{4}$ and $\phi = \frac{3\pi}{4}$, where the muon wire chambers change orientation (the effect of the octant boundaries at $\phi = \frac{5\pi}{4}$ and $\phi = \frac{7\pi}{4}$ are also present but obscured by the larger effect of the hole in the bottom). The p_T of the muon is corrected for the energy loss of the muon in the calorimeter, due to ionization. This loss is around 2 GeV , as is shown by figure 6.1.

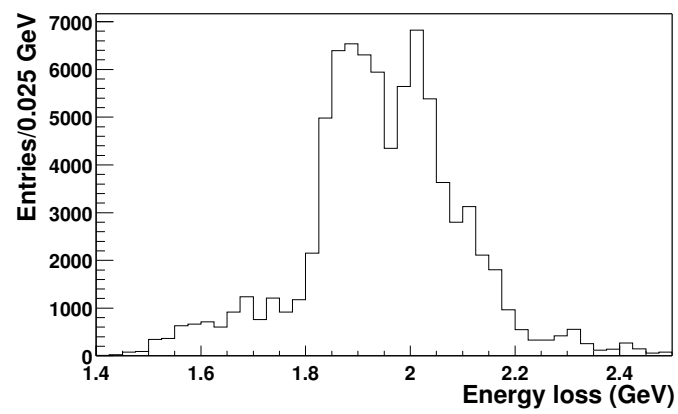


Figure 6.1: *Energy loss of a muon as it traverses the calorimeter.*

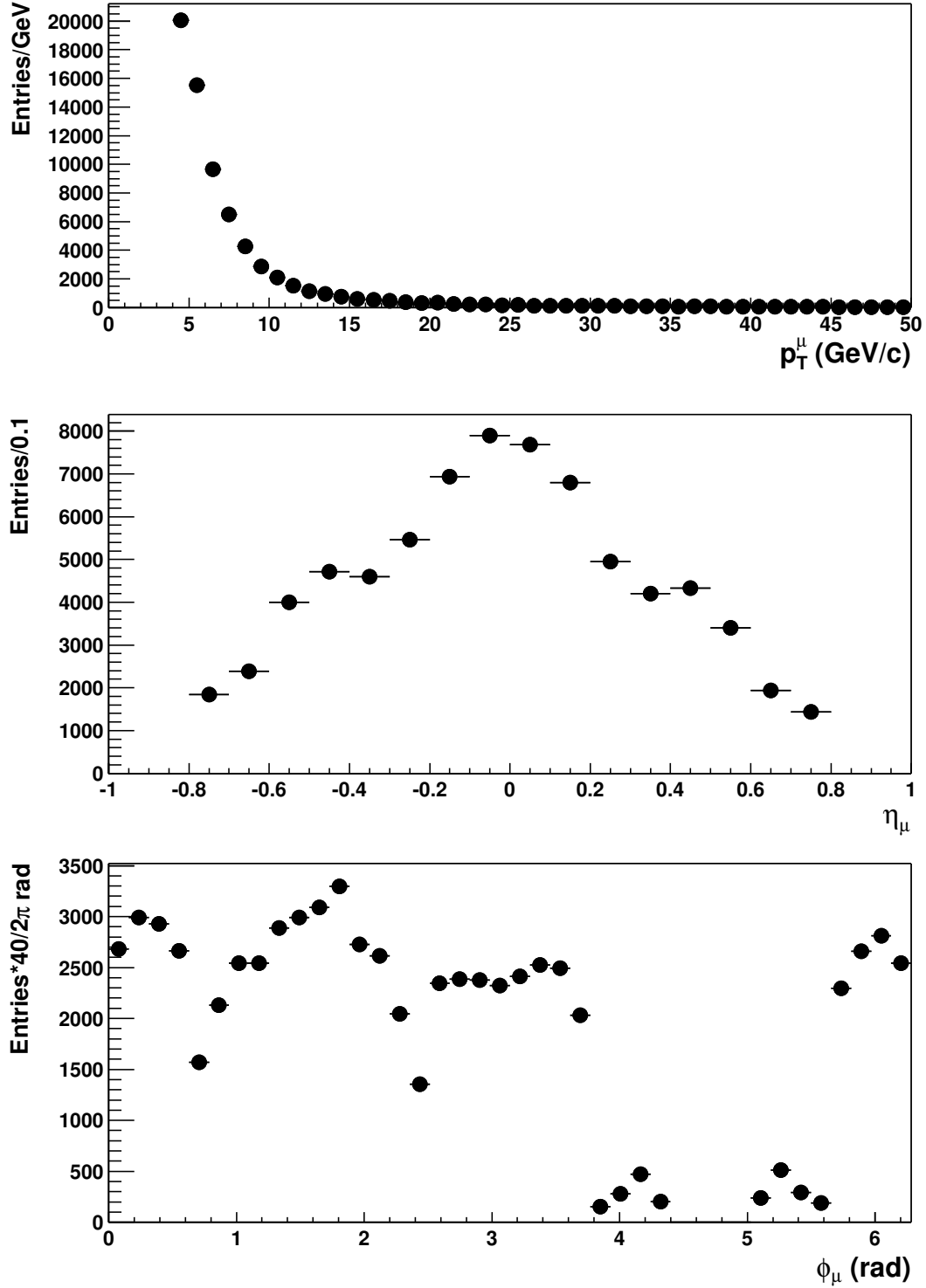


Figure 6.2: p_T , η and ϕ distributions of reconstructed muons, after applying kinematic cuts. The statistical errors on the data points are so small that they are hidden by the data points.

6.1.1 Cosmic ray contamination

A major source of background to muons produced in the collisions are cosmic ray muons that pass through the muon detector and mimic a muon. As has been shown in Run I [33], the requirement of the jet association removes the majority of this contamination. This effect can also be seen in the dataset used for this analysis, if we select muons associated with jets and count how many of these are outside the trigger gate, i.e. cosmic ray muons. This number turns out to be of the order of $0.2 \pm 0.05\%$, and can therefore safely be neglected.

6.1.2 Punch through

A possible irreducible background to genuine muons are pions that punch through the calorimeter and the muon toroid, faking a muon. In Run I this effect was investigated, and no punch through was observed for jets with $E_T^{jet} < 200$ GeV [11]. To investigate this effect in the (for this particular effect unchanged) Run II detector, we select a data sample of reconstructed muons and jets, with the muon in a cone of $\delta R < 0.7$ of the jet axis. If the muon is caused by punch-through, we expect the number of hits in the A-layer of the muon system around the muon to increase with increasing E_T^{jet} . As can be seen in figure 6.3, no dependance of the number of A-layer hits is observed (a similar plot can be made for the number of B- and C-layer hits), and the amount of punch through can be ignored.

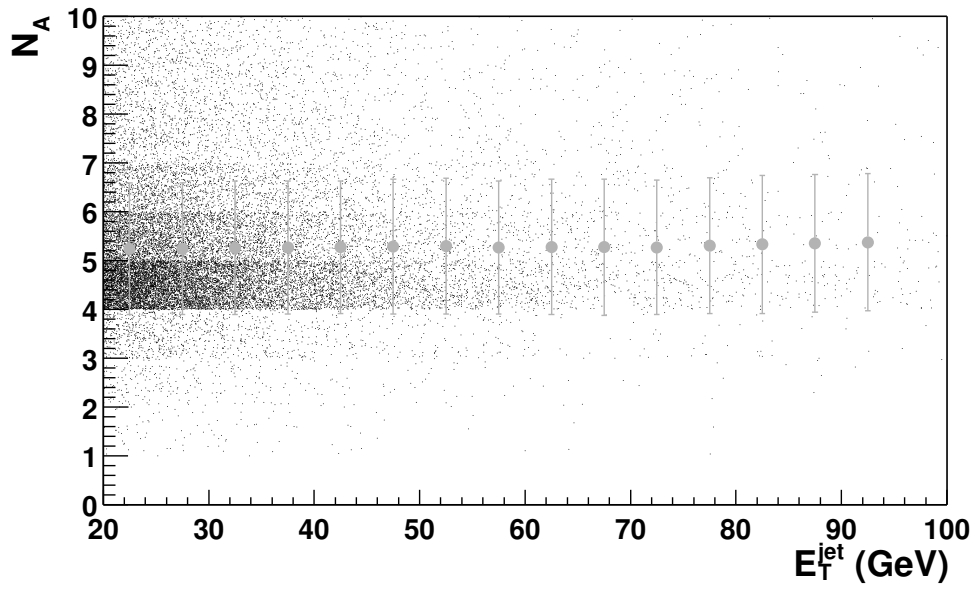


Figure 6.3: Number of hits around a muon in the A-layer of the muon system, as a function of E_T^{jet} . The points represent the averages in each E_T^{jet} bin, with the errors representing the spread.

6.2 Jet Selection and Identification

The majority of the background to physics jets consists of hot cells, which fake an energy deposit due to electronic noise. Even though these are partially removed at the readout level and by a hot cell suppression algorithm, some still remain and are reconstructed as fake jets. To suppress these jets, the following cuts are applied (see figure 6.4):

- Hot Fraction < 10 : the fraction between the most energetic cell and the next to most energetic cell has to be lower than 10. A higher ratio points to an unbalanced jet in which the highest energy cell is probably a hot cell;
- $1 < n_{90} < 30$: n_{90} is the number of calorimeter towers that contain 90% of the jet energy. If this number is 1, this again points to an unbalanced jet consisting of one tower. If it is greater than 30, the jet consists of a high number of towers which each contain little energy. These are mainly jets consisting completely of noisy cells.
- Coarse Hadronic Fraction (CHF) < 0.4 : The energy fraction of the total energy of the jet in the outer (hadronic) layer of the calorimeter. A coarse hadronic fraction of more than 0.4 is highly unlikely for genuine physics jets;
- Electromagnetic Fraction (EMF) between 0.05 and 0.95: electrons deposit more than 95% of their energy in the electromagnetic calorimeter. The lower bound indicates hot cells in the hadronic calorimeter.

In addition, the following criteria have to be met:

- $|\eta| < 0.6$, to avoid the effects of the jets overlapping with the Inter Cryostat region, where the jets are poorly measured due to the gap between the central and forward calorimeters;
- $E_T > 20$ GeV, to be well above the cut-off energy in the jet reconstruction, where E_T is the transverse energy of the jet, corrected by applying the Jet Energy Scale correction.

The resulting E_T , η and ϕ distributions of the reconstructed jets are displayed in figure 6.5. The E_T distribution turns on at 14.4 GeV, which is caused by the cut-off in the jet reconstruction algorithm, as well as the jet reconstruction efficiency which is only fully efficient above 20 GeV. The η distribution is flat in the region of interest for this analysis, and drops at higher η values due to the reduced calorimeter coverage in the intercryostat region. The ϕ distribution shows an eight-fold structure, due to the requirement of an associated muon with $\delta R(jet, \mu) < 0.7$. Less muons are reconstructed

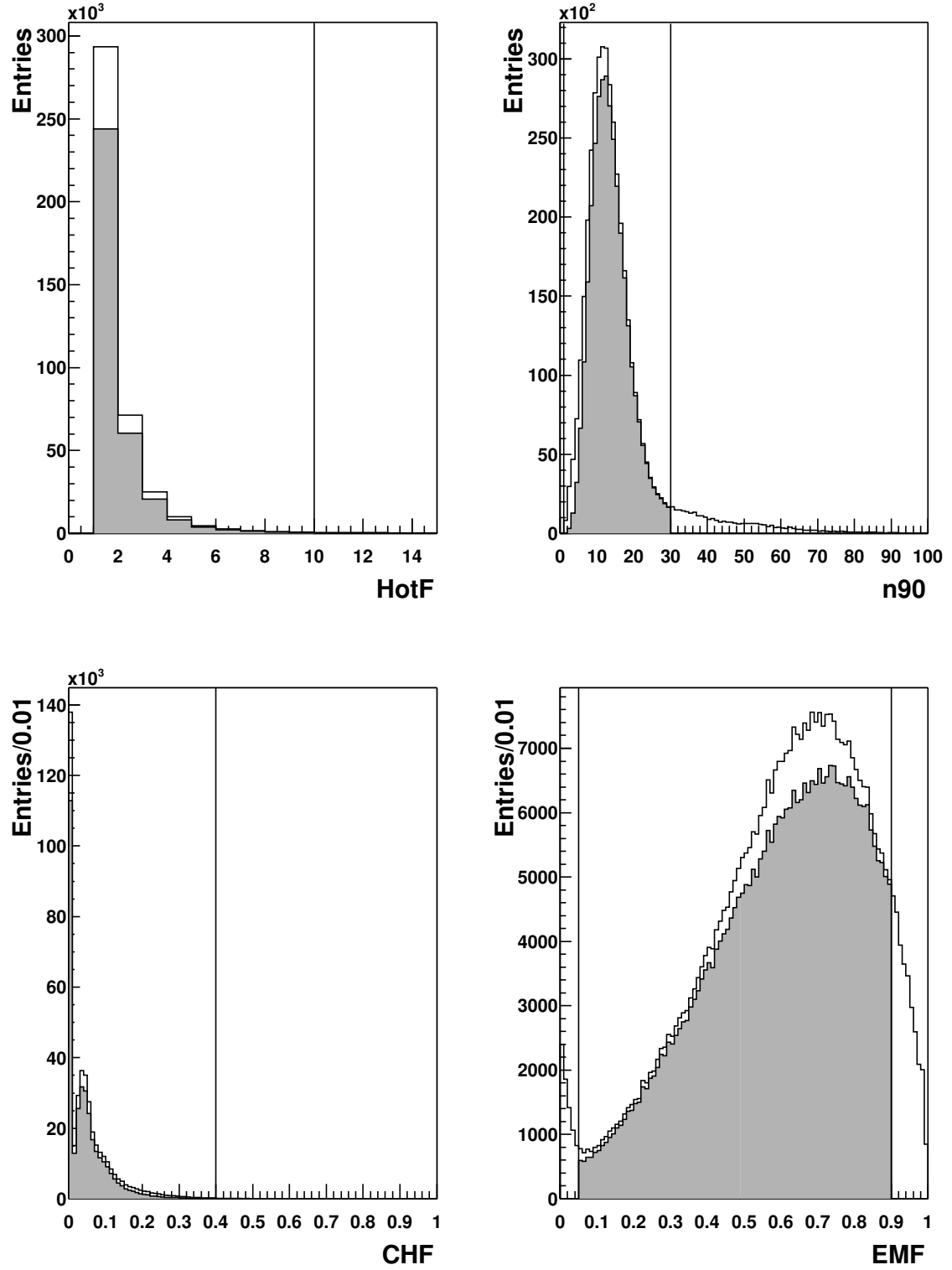


Figure 6.4: Properties of jets used to suppress fake jets, before (open histograms) and after (solid gray histograms) ID cuts. The properties on the horizontal axes are explained in the text.

in the region $\frac{5\pi}{4} < \phi < \frac{7\pi}{4}$, resulting in less associated jets in that region. Also, other side jets in the region $\frac{\pi}{4} < \phi < \frac{3\pi}{4}$ are suppressed by this effect.

6.2.1 Jet ID Efficiency

Not only do the jet ID cuts as explained in the previous section cut out the fake jets, they also remove a number of good jets for which a correction needs to be applied. The extent of this correction is calculated using di-jet events, in which one of the jets passes the ID criteria, and furthermore:

- Both jets have $|\eta| < 0.6$ and $E_T > 20$ GeV, to be in the same fiducial volume as the jets in the data sample;
- The jets are back-to-back: $\Delta\phi > 175^\circ$, and $\cancel{E}_T < 0.7p_T^{\text{leading jet}}$, to ensure a proper di-jet event;
- $E_{\text{tot}} < 2$ TeV, to remove events with noisy calorimeter readout.

The ID efficiency can be extracted from this sample using the following definition:

$$\epsilon_{ID} = \frac{\text{Number of other side jets passing ID cuts}}{\text{Total number of other side jets}} \quad (6.1)$$

This efficiency is shown as a function of jet E_T, η and ϕ in figure 6.6, and averages to $94.2 \pm 0.1\%$. The ID efficiency as a function of jet E_T shows a turn-on curve for jets below 40 GeV. This turn-on curve is caused by the cut on the electromagnetic fraction of the jet - low energy jets deposit a higher fraction of their energy in the first (electromagnetic) layers of the calorimeter. This is demonstrated in figure 6.6 by the small crosses, which represent the jet ID efficiency without the EMF cuts. Without these cuts, the ID efficiency averages to $98.7 \pm 0.1\%$.

An additional event topology that affects this efficiency measurement is back to back γ +jets events, in which the jet passes the ID cuts listed above. To measure the extent of this effect, we count the number of such events in the Monte Carlo simulation as a ratio of number of di-jet events. This ratio results in $0.05 \pm 0.05\%$, indicating that these event topologies do not have a significant effect on the jet ID measurement.

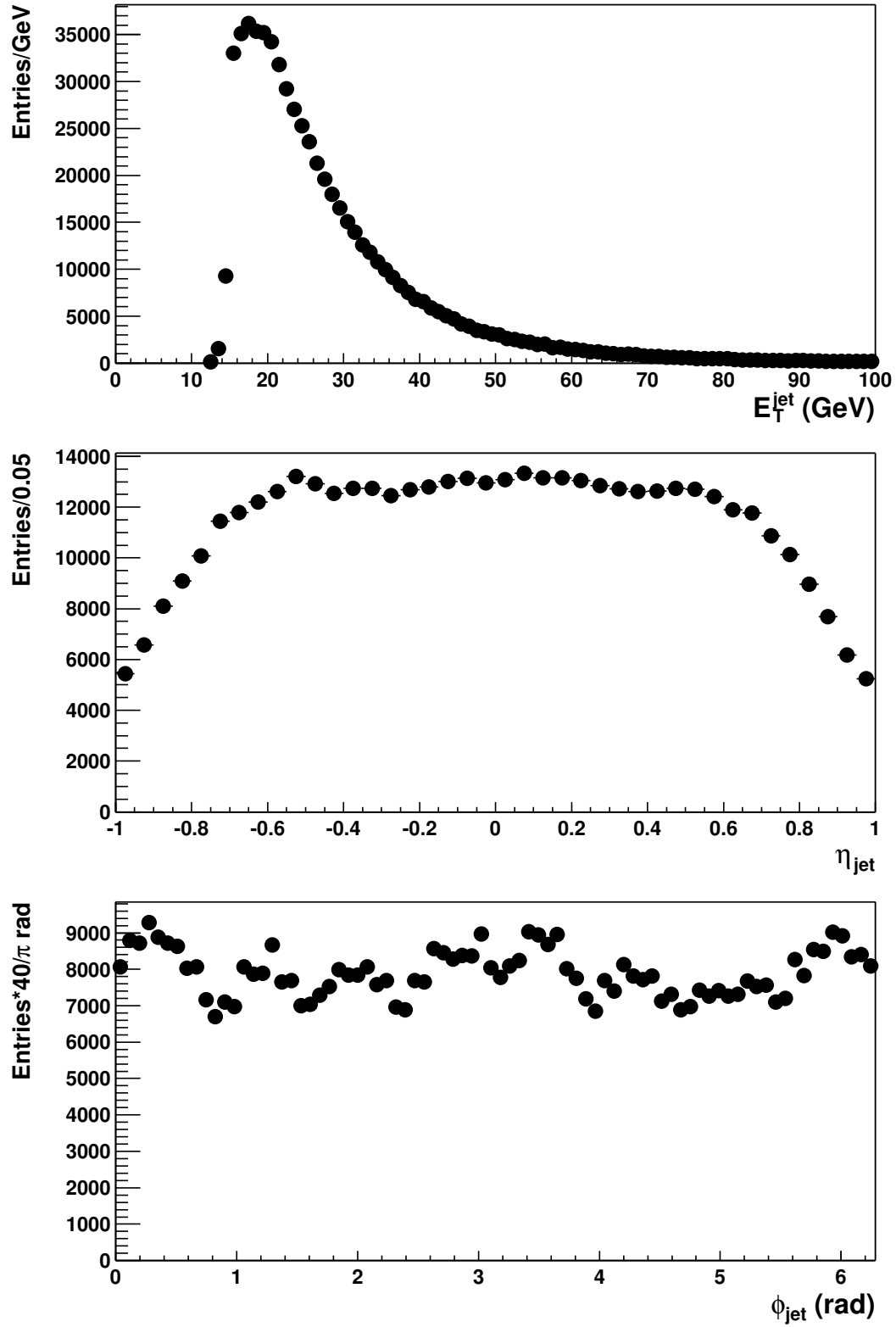


Figure 6.5: E_T , η and ϕ distribution of reconstructed jets, after selection and kinematic cuts.

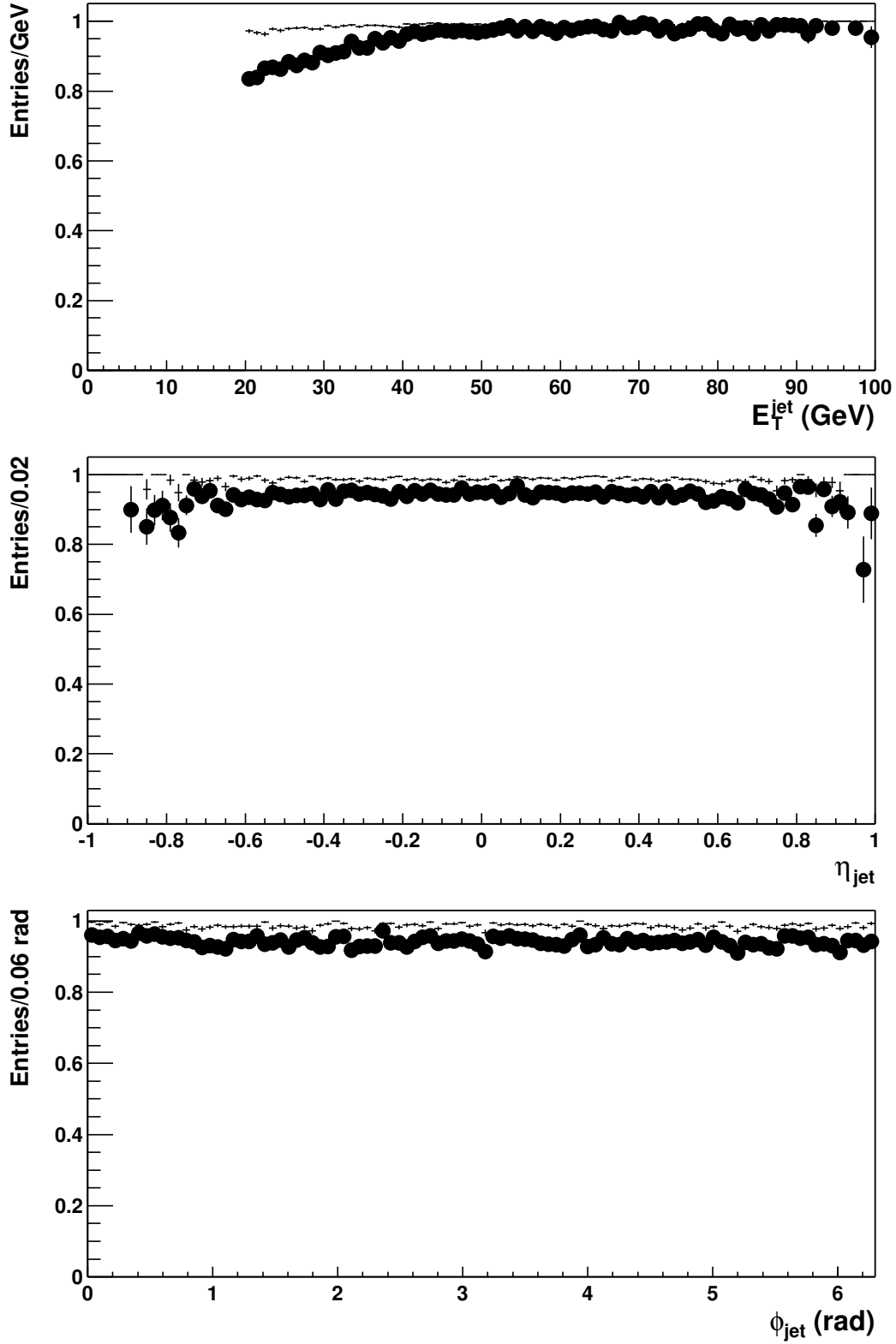


Figure 6.6: Jet ID efficiency as function of E_T^{jet} , η and ϕ . Black dots represent the efficiency after all cuts, the crosses represent the efficiency without the EMF cuts.

Chapter 7

Muon + Jet Cross section

The first step towards the measurement of the b -jet cross section is the measurement of the total μ +jet cross section as a function of the transverse energy of the jet: $d\sigma/dE_T^{jet}$. Using the trigger, reconstruction and identification efficiencies for jets and muons as derived in previous chapters, we will now measure this cross section with the Run II data taken between February 28th and May 10th.

7.1 Differential cross section for μ + jet events

The data sample corresponds to an integrated luminosity of 3.4 pb⁻¹. In this sample, we first measure the differential cross section as a function of E_T^{jetCal} , where E_T^{jetCal} is the transverse energy of the jet, measured in the calorimeter and corrected for the Jet Energy Scale. The ionization energy that the muon deposits in the calorimeter is subtracted from the jet energy. To measure the differential cross section, each event needs to be scaled with the detection efficiency for that event and the total integrated luminosity:

$$\frac{d\sigma}{dE_T^{jetC}} = \frac{1}{\int \mathcal{L} dt} \frac{1}{\epsilon(\mu, jet_C)} \frac{dN}{dE_T^{jetC}} \quad (7.1)$$

Here, dN/dE_T^{jetC} is the number of events in each E_T^{jetCal} bin, $\int \mathcal{L} dt$ is the total integrated luminosity and $\epsilon(\mu, jet_C)$ is the combined efficiency of all trigger, reconstruction and identification efficiencies for the muons and jets in that E_T^{jetCal} bin. Both the jet and the muon have to pass the identification cuts as discussed in chapter 6. Furthermore, we use the following cuts on the jets and the muons:

- $E_T^{jetCal} > 20$ GeV;
- $|\eta^{jetCal}| < 0.6$;
- $p_T^\mu > 6$ GeV/c;

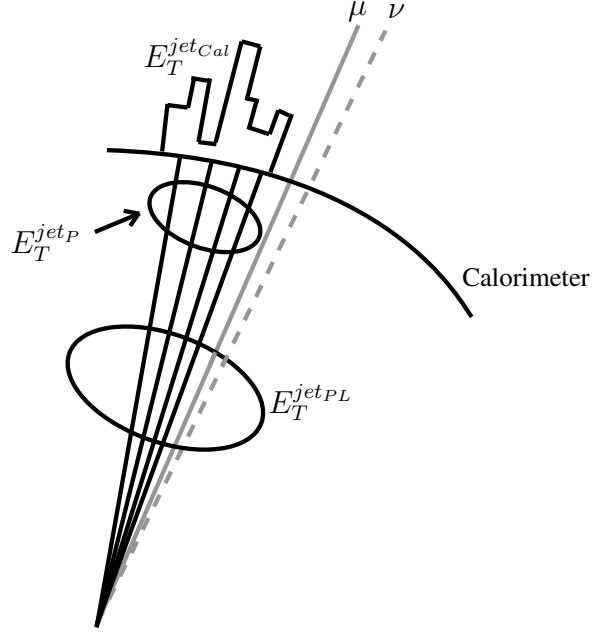


Figure 7.1: Illustration of different jet energy scales used in the analysis. The energy that is deposited in the calorimeter by the jet, represented by the black irregular shape is denoted by $E_T^{jet_{Cal}}$. This energy can be unfolded to the particle level jet energy $E_T^{jet_P}$, which is the energy of all particles in the jet, without the muon and neutrino (shown by the solid and dashed gray lines respectively). Adding the energy of these two particles to the jet energy results in the lepton corrected jet energy, $E_T^{jet_{PL}}$.

- $|\eta_\mu| < 0.8$;
- $\delta R(jet_C, \mu) < 0.7$.

The next step is to extract the differential cross section $d\sigma/dE_T^{jet_P}$ as a function of the true transverse jet energy $E_T^{jet_P}$, where $E_T^{jet_P}$ is the true particle level jet E_T , without the muon and neutrino energy (see figure 7.1). This is done using a correction function $U(E_T^{jet_C})$, which is an unfolding correction that accounts for the finite resolution of the calorimeter. In addition, a correction needs to be applied for the kinematic acceptance $K(E_T^{jet_P})$ of the detector:

$$\frac{d\sigma}{dE_T^{jet_P}} = \frac{K(E_T^{jet_P})}{U(E_T^{jet_C})} \frac{d\sigma}{dE_T^{jet_C}} \quad (7.2)$$

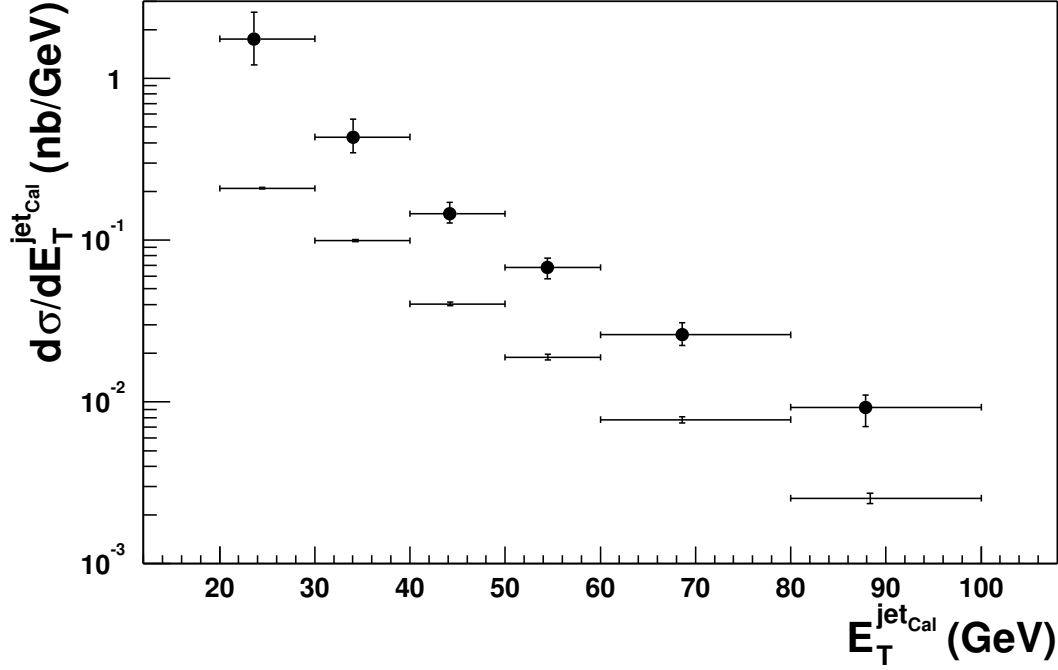


Figure 7.2: μ +jet differential cross section as a function of calorimeter jet E_T . The lower data points show the cross section, uncorrected for trigger, reconstruction and identification efficiencies. The statistical errors are shown, but not visible for most data points. The black dots show the cross section corrected for all these efficiencies, with full statistical and systematic errors.

7.2 Efficiency corrections

The lower data points in figure 7.2 represent the μ + jet cross section as a function of $E_T^{\text{jet}_{\text{Cal}}}$, uncorrected for trigger, reconstruction and identification efficiencies. The horizontal lines represent the bin size, which are chosen according to the jet energy resolution.

The correction to the measured cross section for efficiencies is applied on a jet by jet basis. For every jet with an associated muon, the dependence of the efficiency on the η , ϕ or p_T of the muon and jet is taken into account. We use the 1-dimensional distributions under the assumptions that the efficiency factorizes. The effect of the uncertainty on each efficiency is propagated to the full cross section by varying each efficiency within the errors. Each source of uncertainty is briefly explained below.

Level 1 calorimeter trigger

The μ +jet cross section is corrected for the Level 1 calorimeter trigger efficiency according to the turn-on curve shown in figure 4.3. The effect of the statistical uncertainty of the trigger efficiency on the cross section is shown by the open circles in figure 7.3. The systematic uncertainty of the trigger efficiency is dominated by the uncertainty of the Jet Energy Scale correction. This effect is not taken into account here, but will be discussed below.

Level 1 muon trigger efficiency

The Level 1 muon trigger efficiency shows a dependence on both p_T^μ and η^μ (see figure 4.4). Due to statistical limitations, it is not possible to perform a full 2-dimensional calculation of the efficiency in (p_T, η) bins. Therefore, we first calculate the efficiency averaged over p_T but taking into account the η dependence. Then, the efficiency is calculated using an averaged η efficiency and taking into account the p_T dependence. The difference resulting from using these two different efficiencies is taken as an additional systematic error on the Level 1 muon trigger efficiency. The effect of the resulting total error on the cross section is shown by the black squares in figure 7.3.

Muon reconstruction efficiency

The muon reconstruction efficiency depends on p_T, η , and to a lesser extent, on ϕ (see figure 5.29). Since the physics is invariant under rotations in ϕ , we correct for the hole in the bottom of the detector by an overall scale factor. The dependence on p_T and η is taken into account in a similar fashion as done for the Level 1 muon trigger efficiency. The black circles in figure 7.3 show the systematic error on the cross section resulting from the errors on the muon reconstruction efficiency.

Jet Energy Scale correction

We use the uncertainty on the Jet Energy Scale correction of typically 7%, as shown in figure 5.3, to estimate the systematic effect on the μ +jet cross section. The calculation of the μ +jet cross section is redone for a Jet Energy Scale correction obtained by adding (subtracting) the uncertainty to the nominal values. The resulting effects are illustrated in figure 7.4 by the open triangles. The strong dependence of the μ +jet cross section on the energy scale of the jets leads to effects of 40% in the lowest E_T bin.

The total systematic error is represented by the black triangles in figure 7.4. The resulting μ +jet cross section, measured as a function of the calorimeter transverse jet

energy, $E_T^{jet_{cal}}$, is shown by the black dots in figure 7.2, with statistical and systematic errors. The systematic errors dominate the total error.

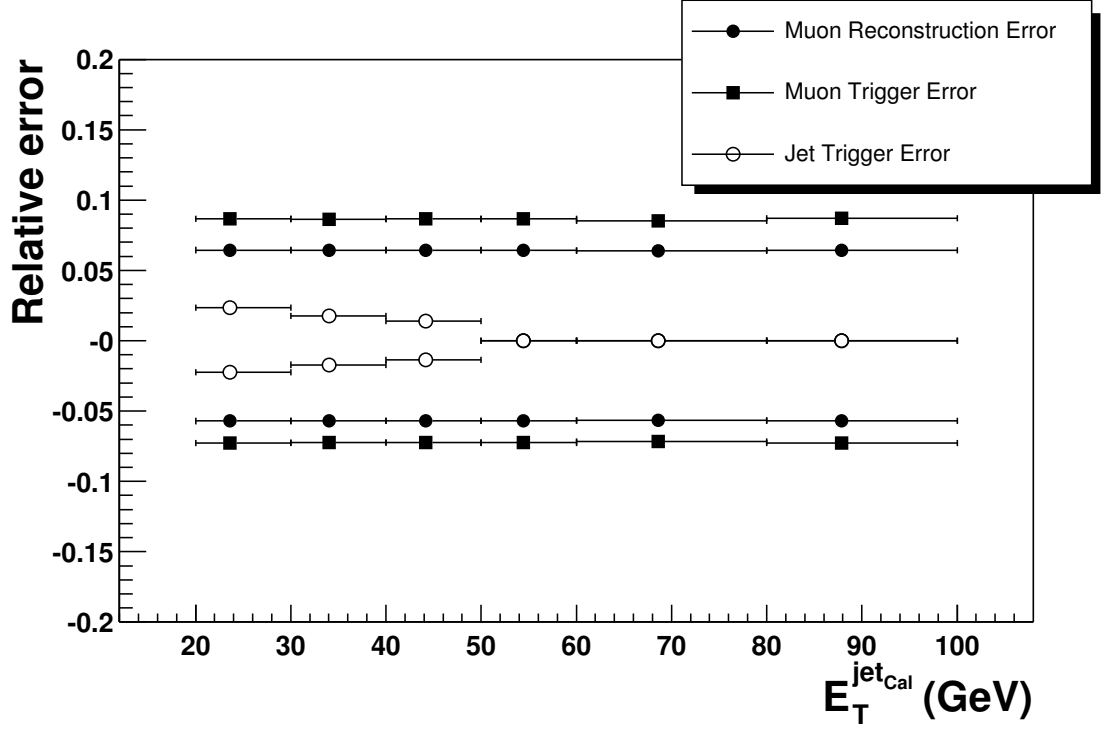


Figure 7.3: Systematic errors on the $\mu + jet$ differential cross section, resulting from the trigger, reconstruction and identification efficiencies, as a function of transverse calorimeter jet energy.

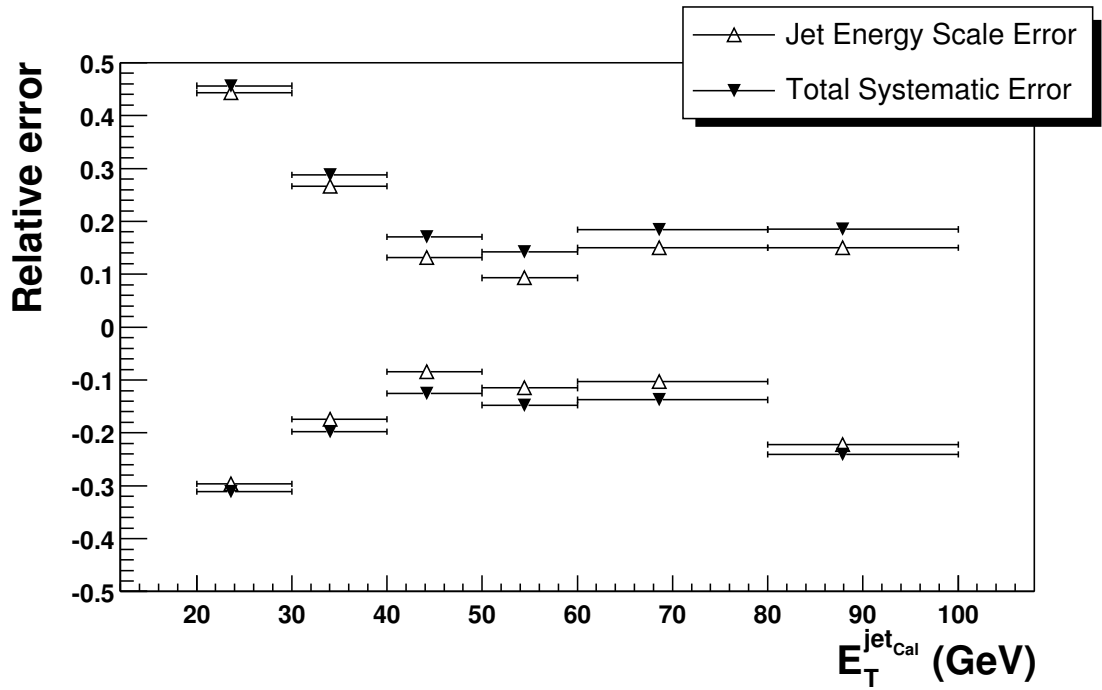


Figure 7.4: Systematic error on the μ +jet differential cross section resulting from the uncertainty on the Jet Energy Scale (open triangles) and the total systematic error (black triangles), as a function of transverse calorimeter jet energy.

7.3 Unfolding the μ +jet cross section

To extract the μ +jet cross section as a function of the true particle energy of the jet from the cross section $\frac{d\sigma}{dE_T^{jet_{Cal}}}$ we have to remove the effect of the finite resolution with which the calorimeter measures the jet energy. We start with an ansatz function for the μ +jet cross section with 3 free parameters, of the form:

$$F(E_T, \alpha, \beta, \gamma) = \alpha E_T^\beta \left(1 - \left(\frac{2}{\sqrt{s}} \right) E_T \right)^\gamma \quad (7.3)$$

where E_T is the true energy of the jet, α, β and γ are free parameters, and \sqrt{s} is the center of mass energy. The shape of this function is based on Monte Carlo trials, and has also been used in the Run I analysis [33]. This function is smeared with the E_T resolution of the jets, as discussed in section 5.2. The parameters of this ansatz function are obtained in a fit procedure, such that the smeared ansatz function represents the measured cross section. The errors on the parameters of the jet energy resolution are analytically propagated to the resolution function using the full covariance matrix, and the error on the unfolded cross section resulting from this uncertainty is estimated by varying the resolution function within the errors. Figure 7.5 shows the result of this unfolding procedure, where the solid curve is the ansatz function, and the dotted curve the smeared ansatz function. The smeared ansatz function shows good agreement with the data points. The fact that the ratio of the smeared ansatz function (dashed curve) and the ansatz function itself (solid curve) is greater than one over the entire $E_T^{jet_C}$ range can be understood by Gaussian smearing of each bin in the ansatz function. Since the cross section drops rapidly with increasing $E_T^{jet_C}$, more events migrate from low energy bins to higher energy bins than there are events that migrate from higher energy bins to lower energy bins. Shown in figure 7.6 is the ratio between the smeared ansatz and the ansatz function itself, with the dashed lines representing the errors resulting from varying the jet energy resolution errors. The measured cross section is now updated according to this ratio, according to:

$$\frac{d\sigma}{dE_T^{jet_P}} = \frac{1}{U(E_T^{jet_C})} \frac{d\sigma}{dE_T^{jet_C}} \quad (7.4)$$

where $U(E_T^{jet_C})$ is the ratio shown in figure 7.6. The relative error on $U(E_T^{jet_C})$ is added in quadrature to the previously calculated systematic errors of the cross section.

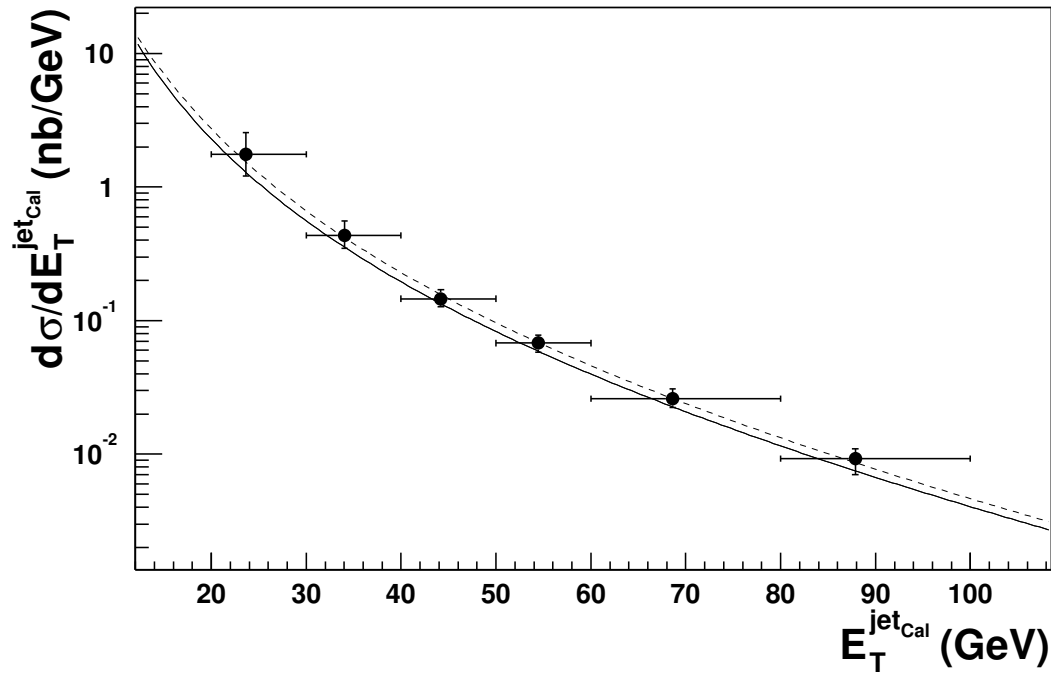


Figure 7.5: Comparison of the smeared ansatz function, represented by the dashed line, with the data points. Also shown by the solid line is the underlying ansatz function which generates the smeared ansatz function through the jet energy resolution.

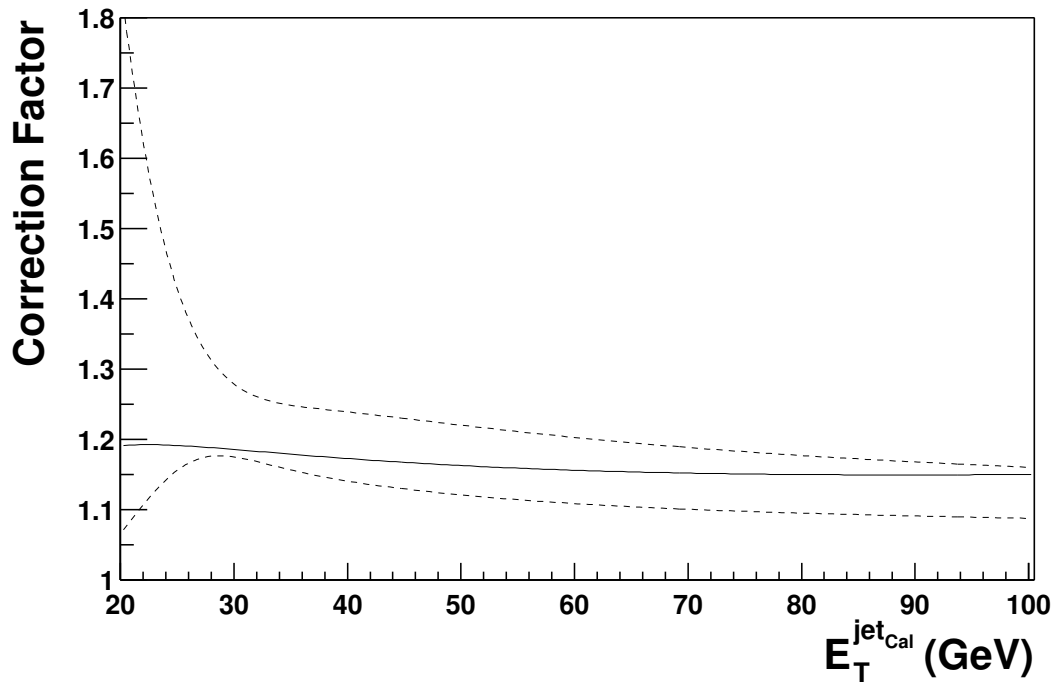


Figure 7.6: *Ratio between the smeared ansatz and the ansatz function. The dashed lines represent the errors on this ratio.*

7.4 Kinematic acceptance corrections

We measure the cross section in the kinematic region with $p_T^\mu > 6$ GeV/c, $|\eta_\mu| < 0.8$ and $|\eta_{jet}| < 0.6$. The reconstructed kinematic properties of the muons and jets are smeared around their true values, which causes fluctuation of events in and out of the kinematic region in which the cross section is measured. Therefore, the unfolded cross section needs an additional correction for the effects of these cuts. We investigate this effect using the QCD Monte Carlo simulation, in which we select particle jets with an associated muon with $\delta R < 0.7$. Two distributions are extracted, both as function of the transverse particle jet energy, E_T^{jetP} . The first distribution is the number of events in each E_T^{jetP} bin that passes the kinematic acceptance cuts, using the Monte Carlo true values of the jet and the muon. For the second distribution, we smear the kinematic properties of the muons and jets according to the measured resolutions in the data, and count the number of events in each E_T^{jetP} bin that pass the kinematic acceptance cuts using the smeared kinematic properties of the jet and the muon. Dividing the first histogram by the second results in the correction factor $K(E_T^{jetP})$ that we have to apply to the measured cross section. This factor is independent of E_T^{jetP} and close to one (1.018 ± 0.036), as can be seen in figure 7.7.

Correcting the measured cross section for the unfolding and the kinematic acceptance, according to equation 7.2, results in the differential μ +jet cross section as a function of particle jet E_T , or E_T^{jetP} , without the muon and neutrino energy, as is shown in figure 7.8. Also shown is the Pythia prediction for μ +jet events.

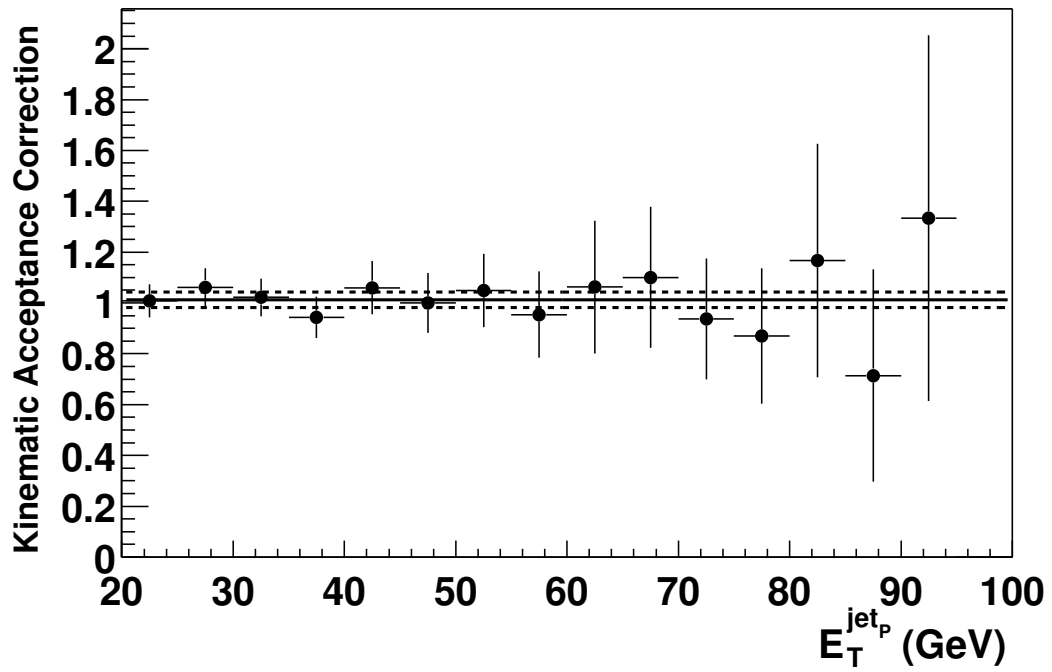


Figure 7.7: Kinematic acceptance correction to account for the effect of smearing the kinematic properties of the muon and jet on the cross section.

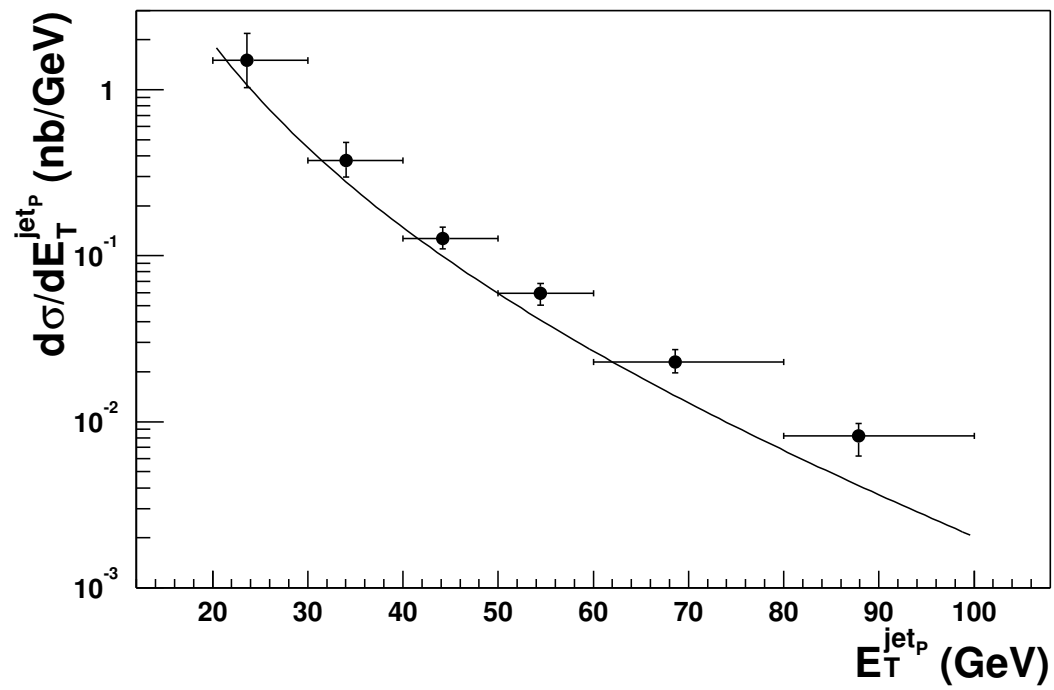


Figure 7.8: Differential μ +jet cross section as function of particle jet E_T , without muon and neutrino corrections. The black curve represents the Pythia prediction for this cross section.

Chapter 8

B -jet cross section

In $p\bar{p}$ collisions, the b -jets are produced according to some distribution as function of the true b -jet energy $E_T^{jet_{PL}}$. It is this distribution that we want to measure in this analysis. However, in the experiment we cannot measure this distribution directly, since it is folded with a number of effects that distort the distribution. First, we have to consider the $b \rightarrow \mu + \nu$ decay, in which the muon and neutrino carry away energy from the jet energy. The measurement of the remaining jet energy is distorted by the resolution and kinematic acceptance of the calorimeter. Also, other processes occur in the collisions which can produce a muon and a jet. If we call the underlying distribution according to which the b -jets are produced F , it is convoluted with the effects described above, according to:

$$G(E_T^{jet_{Cal}}) = X^{\mu+jet}(E_T^{jet_{Cal}}) \oplus R^{Cal}(E_T^{jet_P}) \oplus C^{b \rightarrow \mu + \nu}(E_T^{jet_{PL}}) \oplus F(E_T^{jet_{PL}}) \quad (8.1)$$

where $C^{b \rightarrow \mu + \nu}(E_T^{jet_{PL}})$ is the effect of the energy carried away from the jet through the $b \rightarrow \mu + \nu$ decay, $R^{Cal}(E_T^{jet_P})$ represents the resolution and kinematic acceptance of the calorimeter and $X^{\mu+jet}(E_T^{jet_{Cal}})$ is the distribution of other μ +jet producing processes. It is this distribution $G(E_T^{jet_{Cal}})$ that is measured in the experiment, and which forms the basis from which we extract the function F . For this extraction we need to correct for each effect in the above equation.

The first step is to extract the b -jet content from the measured μ +jet cross section. For this we use a variable called P_T^{Rel} , which is the transverse momentum of the muon with respect to the combined μ +jet axis. The resulting b -jet cross section is then corrected for detector effects, notably the energy resolution, and the kinematic acceptance cuts, to get the b -jet cross section as function of $E_T^{jet_P}$, without the muon and neutrino energies. Also correcting for the energy carried away by the muon and neutrino, as well as the $b \rightarrow \mu + \nu$ branching ratio yields the detector independent b -jet cross section measurement as a function of jet E_T , including the energy of the muon and neutrino.

We start with the μ +jet events, where the transverse energy of the jet is measured

in the calorimeter and corrected for the Jet Energy Scale, E_T^{jetCal} . The ionization energy of the muon that transversed the calorimeter, as discussed in section 6.1, is subtracted from this energy. Using the momentum of the muon relative to the μ +jet axis, P_T^{Rel} , the fractional b -jet content $B(E_T^{jetCal})$ is extracted as a function of E_T^{jetCal} . The muon tagged b -jet cross section can now be written as:

$$\frac{d\sigma}{dE_T^{jetCal}} = B(E_T^{jetCal}) \frac{d\sigma}{dE_T^{jetCal}} \quad (8.2)$$

Similar to the procedure described in section 7.3, this muon tagged b -jet cross section needs to be corrected for the resolution of the calorimeter. This correction will be applied in two ways. First, we will correct for the resolution of the calorimeter only. This results in the b -jet cross section as a function of E_T^{jetP} , which is the true jet energy without the energy of the muon and the neutrino:

$$\frac{d\sigma}{dE_T^{jetP}} = \frac{K(E_T^{jetP})B(E_T^{jetCal})}{U(E_T^{jetCal})} \frac{d\sigma}{dE_T^{jetCal}} \quad (8.3)$$

where $U(E_T^{jetCal})$ is the unfolding correction that accounts for the calorimeter resolution, and $K(E_T^{jetP})$ is the kinematic acceptance factor, described in section 7.4

Ultimately we are interested in the b -jet cross section as a function of the b -jet energy, with no constraints on the decay of the b -quark. The energy carried away by the muon and neutrino is not a fixed amount, but varies, and induces an uncertainty on the full jet energy with the muon and neutrino included, E_T^{jetPL} . This uncertainty can be dealt with in the same manner that we deal with the calorimeter resolution, namely using an ansatz function that is smeared according to a resolution to represent the data. Doing both corrections sequentially results in the same correction as smearing the ansatz function with both resolutions before fitting to the data. Therefore, we correct for both in one single step called $U_L(E_T^{jetCal})$. We again start from the cross section measured as function of E_T^{jetCal} . The correction $U_L(E_T^{jetCal})$ transforms the cross section measured as a function of E_T^{jetCal} into a cross section measured as a function of E_T^{jetPL} , which is the transverse energy of the jet with all leptons included. Finally, this cross section also needs a kinematic acceptance correction $K(E_T^{jetPL})$ to correct for smearing effects in and out of the fiducial region in which we measure the cross section, and a correction for the branching ratio $BR(b \rightarrow \mu)$. Summarizing, the differential b -jet cross section will be measured as:

$$\frac{d\sigma}{dE_T^{jetPL}} = \frac{K(E_T^{jetPL})U_L(E_T^{jetCal})B(E_T^{jetCal})}{BR(b \rightarrow \mu)} \frac{d\sigma}{dE_T^{jetCal}} \quad (8.4)$$

Each of the steps discussed above will be explored in detail in the following sections.

8.1 Extraction of the b -jet component

To extract the b -jet component $B(E_T^{jetCal})$ used in equations 8.2-8.4 from the μ +jet sample we use the properties of the muon with respect to the jet to identify direct $b \rightarrow \mu$ decays. Background processes are $c \rightarrow \mu$ decays, $\pi/K \rightarrow \mu$ decays and $\tau \rightarrow \mu$ decays. The cross section for $W/Z \rightarrow \mu$ decays is so small compared to the b -jet cross section that these decays can be neglected. A good discriminant between these production processes is the quantity P_T^{Rel} , which is explained in detail below.

8.1.1 P_T^{Rel} Tagging variable

The P_T^{Rel} tagging variable is defined as the transverse momentum of the muon with respect to the combined axis of the muon and jet (see figure 8.1). It is measured using the jet direction and energy, and the muon direction and momentum. The variable is based on the decay of the quark in the jet: in the rest system of the meson or hadron that contains the b -quark, the muon gets a significant momentum due to the mass difference of the b -quark and its decay products. This momentum is lower when a c - or light quark decays, because the mass difference between those quarks and their decay products is lower. If the whole system is boosted along the quark momentum axis, the P_T^{Rel} variable is a measure for the transverse boost of the muon with respect to the quark momentum axis. The discriminating power of this variable is shown in figure 8.2, which shows the P_T^{Rel} of the muon from different decays on the Monte Carlo true level. Already on this level, it can be seen that $\pi/K \rightarrow \mu$ decays, $c \rightarrow \mu$ decays and $b \rightarrow c \rightarrow \mu$ decays are practically indistinguishable. The resolution of the detector measurement of the muon and the jet will make the difference between the distributions even less, resulting in an inability to separate these decays.

Therefore, we divide the sample in two parts: $b \rightarrow \mu$ and non- $b \rightarrow \mu$, where the non- $b \rightarrow \mu$ includes the cascade decay $b \rightarrow c \rightarrow \mu$. The resulting P_T^{Rel} distributions in the two samples are used for the extraction of the b -jet content, and are referred to as templates.

Figure 8.3 shows the P_T^{Rel} distribution measured in the data, with the following cuts:

- $E_T^{jetCal} > 20 \text{ GeV}$;
- $|\eta^{jetCal}| < 0.6$;
- $p_T^\mu > 6 \text{ GeV}/c$;
- $|\eta^\mu| < 0.8$;
- $\delta R(jet, \mu) < 0.7$.

To measure the b -jet content of the data, we need templates that describe the shape of the P_T^{Rel} variable in background events and signal events. These templates are for a large part extracted from the Monte Carlo simulation, as explained in detail in the next sections.

Smearing of Monte Carlo templates

As was shown in chapter 5, the resolution with which the Monte Carlo simulation measures the kinematic properties of reconstructed muons and jets is underestimated compared to the resolutions in data. To be able to use the P_T^{Rel} shape that is extracted from the Monte Carlo simulation to measure the b -jet content in the data, we have to account for this effect, and apply smearing corrections to the kinematic properties of the muons and jets we extract from the Monte Carlo events. For the jets, we only need to smear the transverse energy since the η and ϕ directions are measured with comparable resolution in the Monte Carlo simulation as in the data (see section 5.2). The transverse energy of the jets is smeared according to the results of section 5.2. For the reconstructed muons in the Monte Carlo simulation we smear the p_T, η and ϕ of the muons, as they were derived in section 5.3.3.

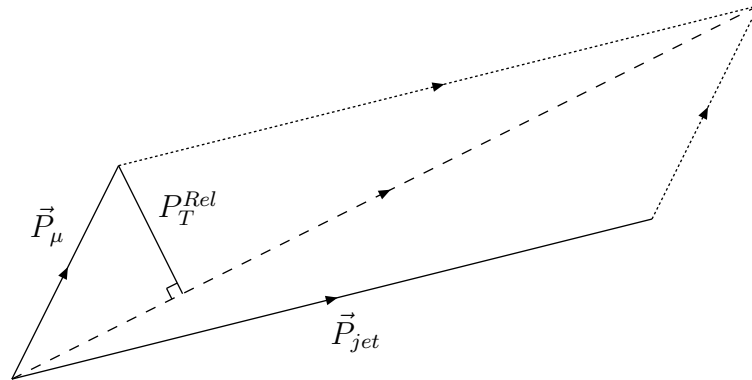


Figure 8.1: The definition of the P_T^{Rel} variable. The muon direction and momentum are indicated by \vec{P}_μ , the jet direction and energy by \vec{P}_{jet} . Adding these two vectors results in the combined μ +jet axis, indicated by the dashed line. The P_T^{Rel} of the muon is now the transverse momentum of the muon with respect to this axis.

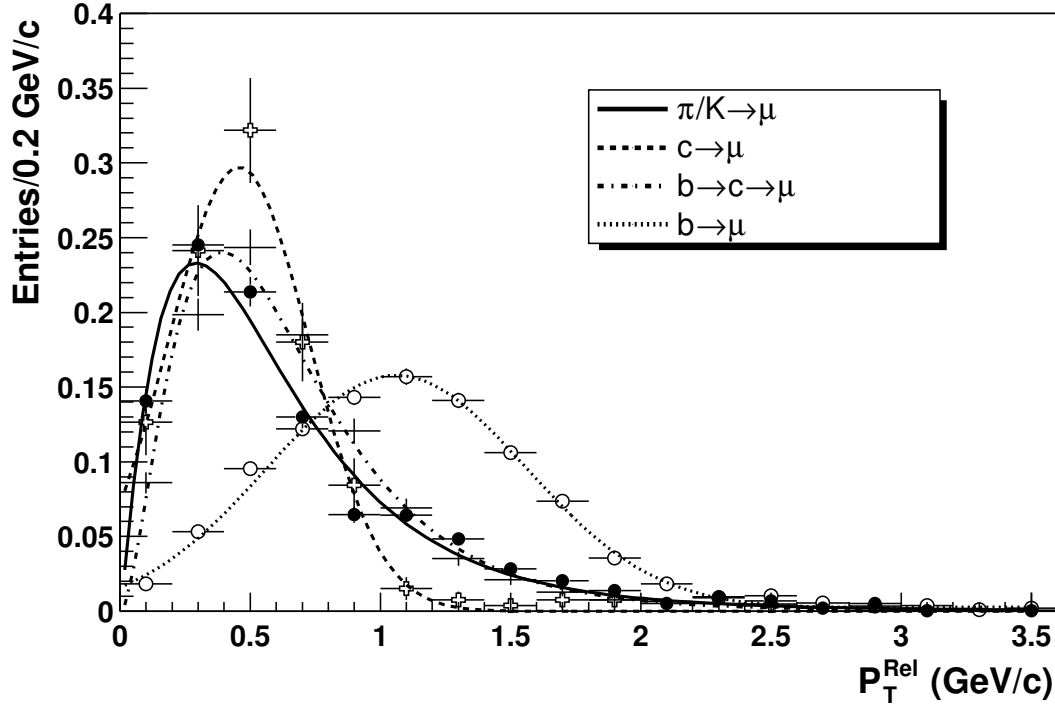


Figure 8.2: P_T^{Rel} templates at the Monte Carlo true level. The $c \rightarrow \mu$ decay includes the $b \rightarrow c \rightarrow \mu$ decay.

Extraction of the signal P_T^{Rel} template

The shape of the P_T^{Rel} distribution for $b \rightarrow \mu$ decays is obtained with a Monte Carlo sample of 0.5 million $b\bar{b}$ events, with no initial constraints on the decay of the b -quarks. From this sample, events are selected that contain a reconstructed jet and a reconstructed muon, with a δR separation between the jet and the muon of less than 0.7. Also, the muon is matched with a muon from the Monte Carlo information within a cone of $\delta R < 0.3$ and is required to be a direct decay product of the parent b -quark. The kinematic properties of the muons and jets are then smeared as explained previously, and the same cuts are applied as listed above, resulting in the P_T^{Rel} template illustrated by the open circles in figure 8.4.

The $b\bar{b}$ events are generated in Pythia using the direct $b\bar{b}$ production process, which uses the leading order matrix elements for massive quarks, but which does not include processes like flavor excitation and gluon splitting. Especially the latter might impact the shape of the P_T^{Rel} distribution, due to the possibility of two heavy quarks present in the same jet. This effect is investigated by running the Pythia simulator in a generic QCD mode that includes the flavor excitation and gluon splitting processes.

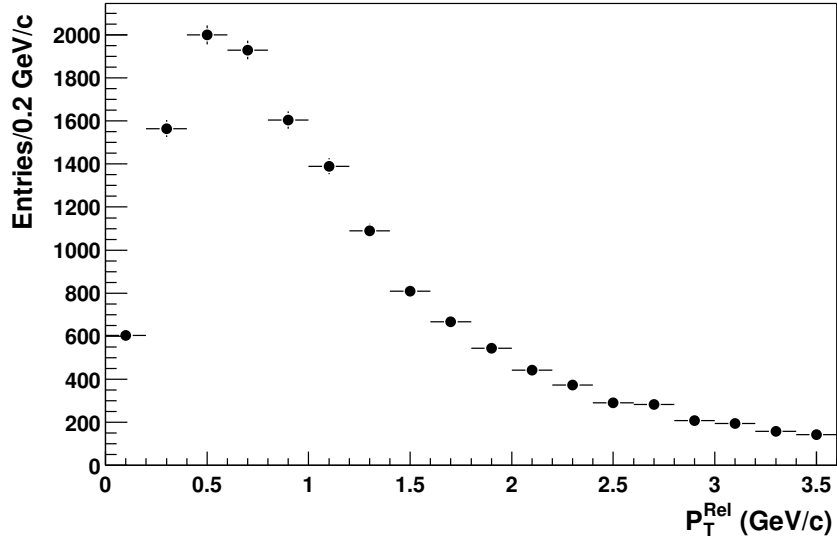


Figure 8.3: *Distribution of the P_T^{Rel} variable in the data sample.*

From the generated events the b -producing events are then extracted. We now look at the difference in the resulting P_T^{Rel} shape for the $b \rightarrow \mu$ decays in both the direct $b\bar{b}$ production and the $b \rightarrow \mu$ decays extracted from the QCD generation mode. We split the templates in two E_T^{jet} ranges, $E_T < 35$ GeV and $E_T > 35$ GeV, to account for the fact that high E_T jets are more likely to contain two b -quarks (see figure 2.6). The resulting templates are shown in figure 8.5. For both E_T ranges, no significant difference is visible between the P_T^{Rel} templates from QCD and $b\bar{b}$ production. Since we have higher statistics in the sample extracted from direct $b\bar{b}$ production, we use that for further analysis.

Extraction of the background P_T^{Rel} template

The biggest difficulty in extracting the P_T^{Rel} template for non- $b \rightarrow \mu$ decays is the contribution of $\pi/K \rightarrow \mu$ decays. Pythia treats pions and kaons as stable at the generation level, and they are decayed at the detector simulation step. To be able to get a template for the background with reasonable statistics, we have simulated 2.5 million QCD events, from which all non- $b \rightarrow \mu$ decays have been extracted. If we apply the same fiducial cuts as used in the data, the majority of the events is removed, resulting in low statistics in the background template. Properly smearing the jet and muon resolutions results in the template as shown in figure 8.4 by the black circles.

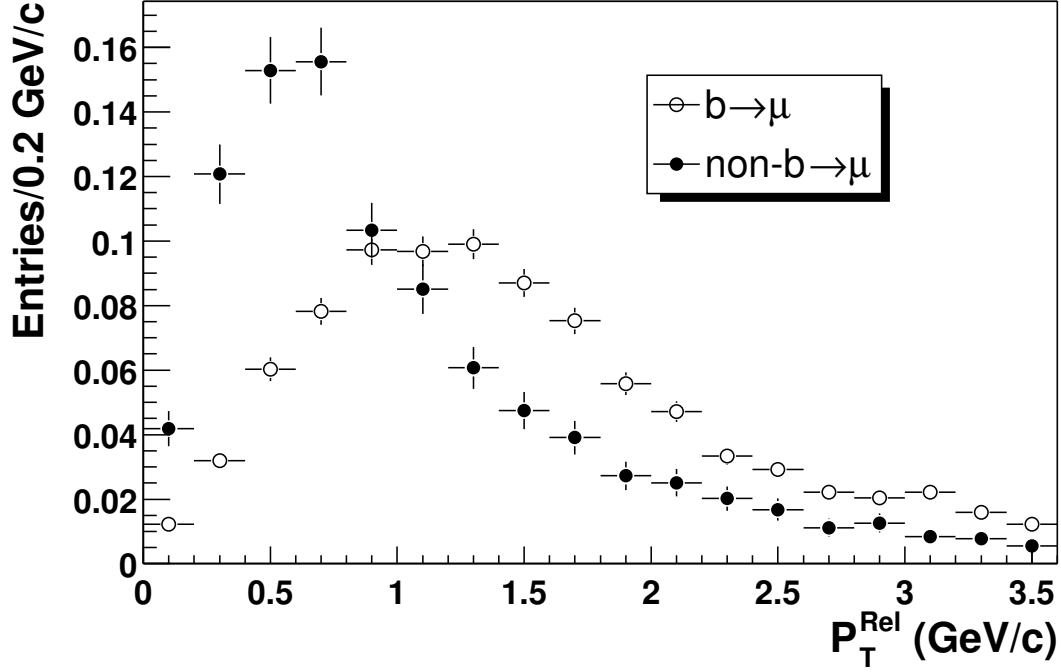


Figure 8.4: P_T^{Rel} templates extracted from reconstructed MC information. The black circles show the P_T^{Rel} distribution of the background template, the open circles show the signal template.

To circumvent the problem of the low statistics, the background template is also extracted directly from the data sample. This is done by selecting tracks reconstructed in the central tracker, which adhere to the following requirements:

- The event is taken during a run which is qualified as good by the central tracking groups;
- Tracks reconstructed with only CFT information are removed, since they do not contain any η information;
- The relative error on the measurement of the p_T of the central track is less than 2.5%, to ensure properly reconstructed tracks;
- $\delta R(jet, central\ track) < 0.7$ to make sure the track is associated with the jet.

If we assume that all tracks are muons from pion decays, we can use them in the P_T^{Rel} template if we weigh them with p_T^{-1} to account for the probability of a pion decaying to a muon, and smear them according to the muon resolution. We do not have to take into

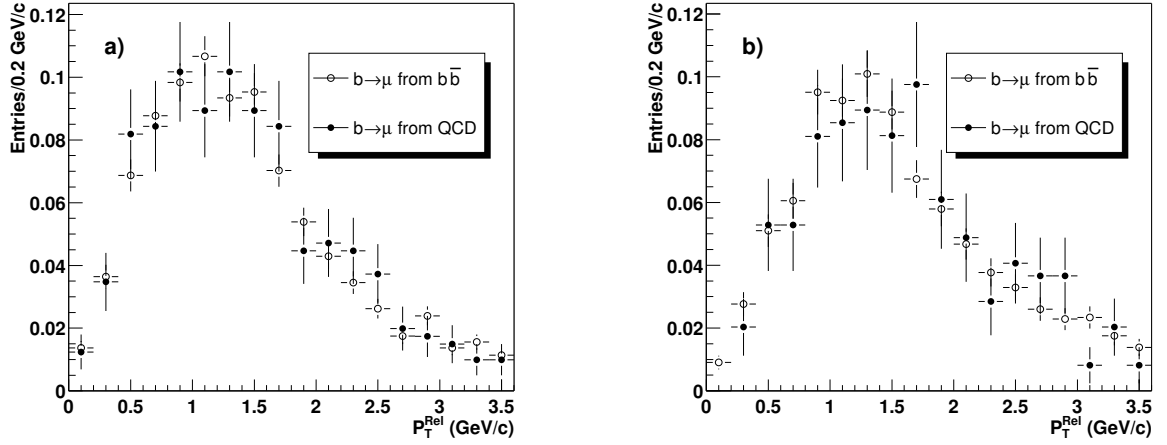


Figure 8.5: Comparison of P_T^{Rel} templates for $b \rightarrow \mu$ decays, extracted from direct $b\bar{b}$ generation (black circles) and from QCD generation (open circles), for $E_T^{jet} < 35$ GeV (a) and $E_T^{jet} > 35$ GeV (b).

consideration the resolution of the central tracks, since the muon resolution is measured with respect to these central tracks, and the resolution with which the central tracks are measured is negligible with respect to the local muon resolution (see section 5.3.3). In addition to higher statistics, this method has the added benefit that the properties of the jets in the events do not have to be smeared, since we are using data events. The data used for the extraction of this template still contains a certain amount of b -quarks. However, since we do not require the presence of a muon in the events, this contribution is not significant. Figure 8.6 shows the resulting template from central tracks, compared to the one using the muons in the QCD Monte Carlo simulation.

8.1.2 Kinematic dependance

Theoretically, the P_T^{Rel} variable is a boost independent quantity, and does not depend on the p_T of the quark nor the p_T of the muon. However, due to the finite resolution of the detector, dependencies on p_T^μ and E_T^{jetCal} are introduced. Since we are ultimately interested in the differential cross section as a function of E_T^{jetCal} , we integrate over p_T^μ and investigate the dependance of the templates on E_T^{jetCal} . This is shown in figure 8.7 for the $b \rightarrow \mu$ and non- $b \rightarrow \mu$ templates, in the E_T^{jetCal} bins:

a. 20 - 25 GeV

b. 25 - 35 GeV

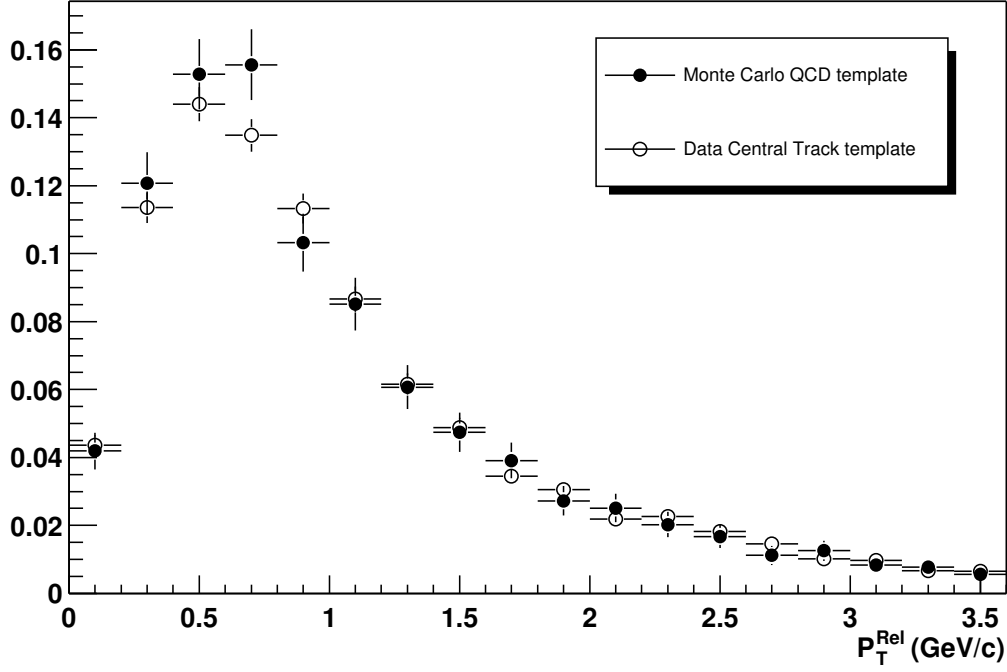


Figure 8.6: P_T^{Rel} templates for light quark jets, extracted from the Monte Carlo simulation (black circles) and from the data using central tracks (open circles).

c. 35 - 50 GeV

d. 50 - 100 GeV

where the size of the bins is constrained by statistics, especially for the non- $b \rightarrow \mu$ template. The strategy is now to divide the data in the same bins of $E_T^{jet_{Cal}}$ and fit the templates to the data to measure the contributions of signal and background in the data, as a function of $E_T^{jet_{Cal}}$.

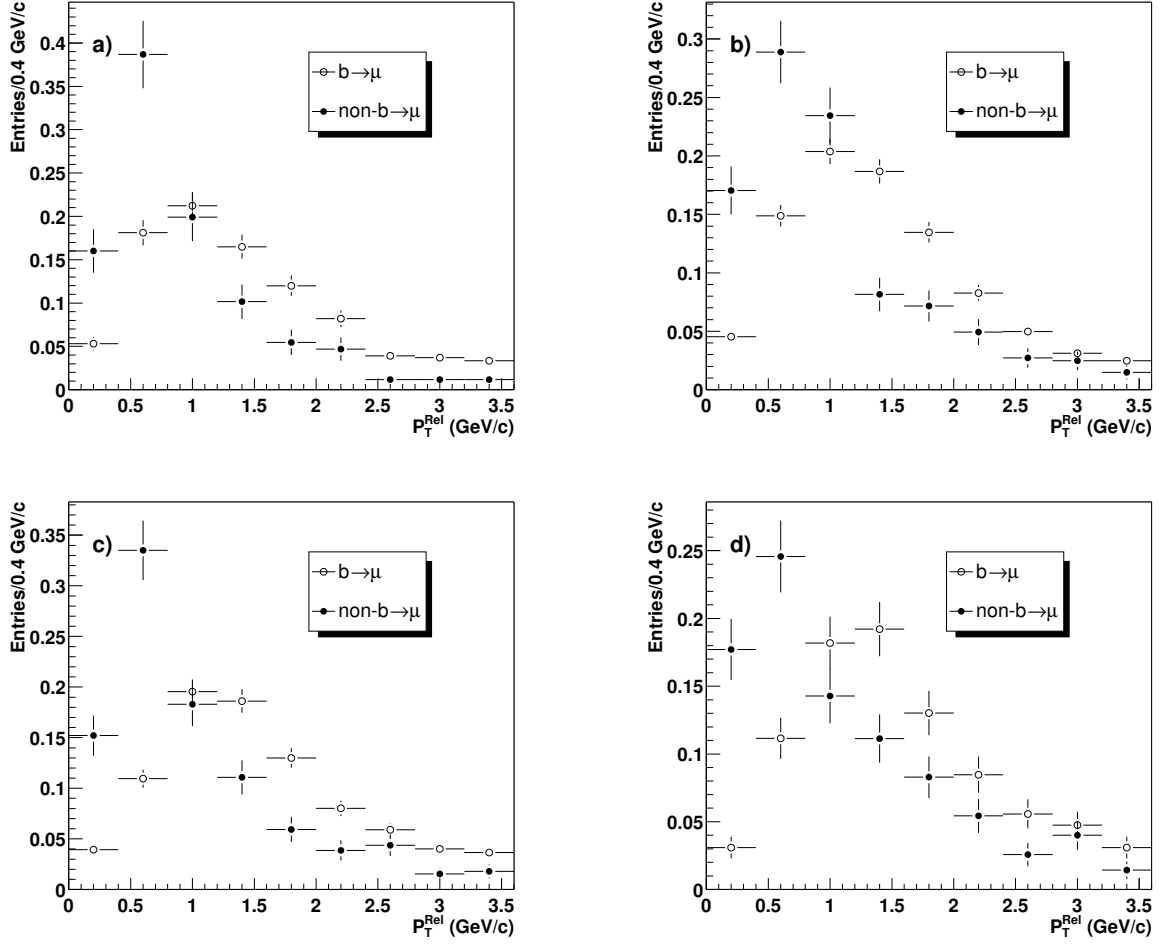


Figure 8.7: Dependence of the P_T^{Rel} templates on E_T^{jet} , in the bins 20-25-35-50-100. The open circles show the $b \rightarrow \mu$ template, while the black dots show the non- $b \rightarrow \mu$ template. The errors on the data points are statistical only.

8.1.3 Template fit

In each of the E_T^{jetCal} bins a fit is done of the P_T^{Rel} templates to the data, according to:

$$\left(\frac{dN}{dP_T^{Rel}} \right)_i^{data} = C_{b \rightarrow \mu} \left(\frac{dN}{dP_T^{Rel}} \right)_i^{b \rightarrow \mu} + C_{non-b \rightarrow \mu} \left(\frac{dN}{dP_T^{Rel}} \right)_i^{non-b \rightarrow \mu} \quad (8.5)$$

where i loops over each E_T^{jetCal} bin, and $\frac{dN}{dP_T^{Rel}}$ represents the P_T^{Rel} distribution in each E_T^{jetCal} bin. The factors C are the scaling factors with which the templates need to be scaled to fit the data. The fit is done using the HMCMLL [3] program, which fits the Monte Carlo templates to the data distribution using a maximum likelihood fit that includes the effect of both the data and Monte Carlo statistics, and returns the best estimate of the fraction of each Monte Carlo template present in the data. This procedure is followed using both the non- $b \rightarrow \mu$ template from the QCD Monte Carlo simulation as well as with the non- $b \rightarrow \mu$ template extracted from the data. Figure 8.8 shows the fit of the QCD template and the $b\bar{b}$ template to the data in all four bins, and the results are summarized in table 8.1. Figure 8.9 shows the fit of the background template extracted from data, and the $b\bar{b}$ template to the data, summarized in table 8.2. Figure 8.10 illustrates these numbers, together with a fit of the form:

$$a + \frac{b}{E_T^{jetC}} \quad (8.6)$$

The shape of this function is chosen after trials using the Monte Carlo simulation, and was also used in the Run I analysis [33]. The dashed gray lines represent the error on the fit. For the final b -jet content measurement, we take the fit that used the background template from data, because of lower errors on the fit. The difference of that fit with the result of the fit using the template from the QCD Monte Carlo simulation is added in quadrature to the present error to cover the uncertainty introduced by the method. This results in the solid gray lines in figure 8.10b.

As a consistency check of the method, we perform a closure test in which we simulate the data sample by taking all $\mu + \text{jet}$ events from the QCD Monte Carlo simulation. This sample then includes well known amounts of $b \rightarrow \mu$ decays and non- $b \rightarrow \mu$ decays. Using the $b\bar{b}$ template extracted from the $b\bar{b}$ sample and the non- $b \rightarrow \mu$ template extracted from the data, we apply the same fit as described above to measure the amount of $b \rightarrow \mu$ decays in the sample. Integrated over the entire E_T^{jetCal} range, this results in a measured b -jet content of $26 \pm 3\%$, compared to a true b -jet content in the sample of $28 \pm 1\%$.

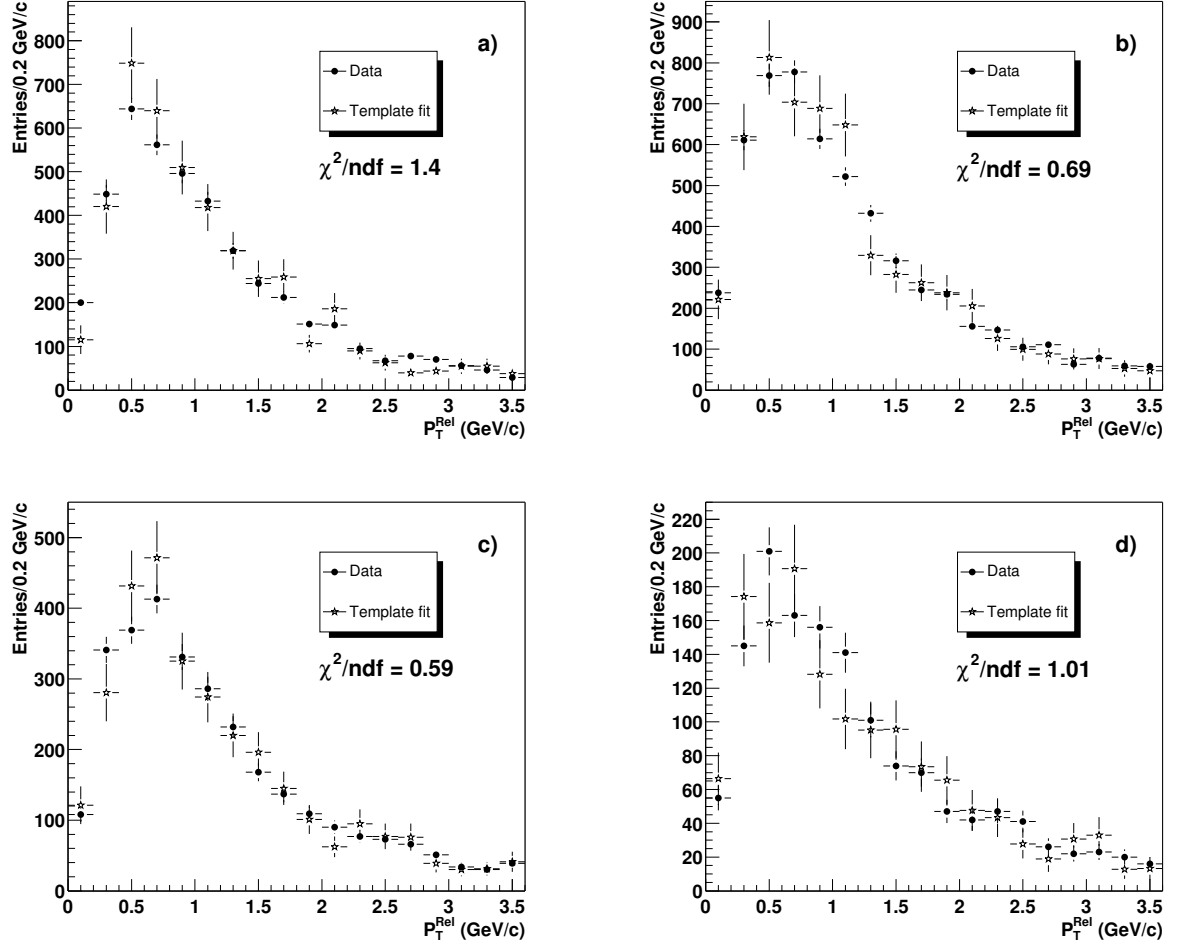


Figure 8.8: Fit of the background template, extracted from the QCD Monte Carlo simulation, and the signal template, to the data in each of the four $E_T^{jet_C}$ bins.

$E_T^{jet_{Cal}}$ range	b-content	background content
20 - 25 GeV	0.39 ± 0.064	0.61 ± 0.073
25 - 35 GeV	0.22 ± 0.066	0.78 ± 0.077
35 - 50 GeV	0.24 ± 0.055	0.76 ± 0.068
50 - 100 GeV	0.14 ± 0.08	0.86 ± 0.10

Table 8.1: The *b*-jet and background content in each bin of $E_T^{jet_{Cal}}$, where the background template is extracted from the QCD Monte Carlo simulation.

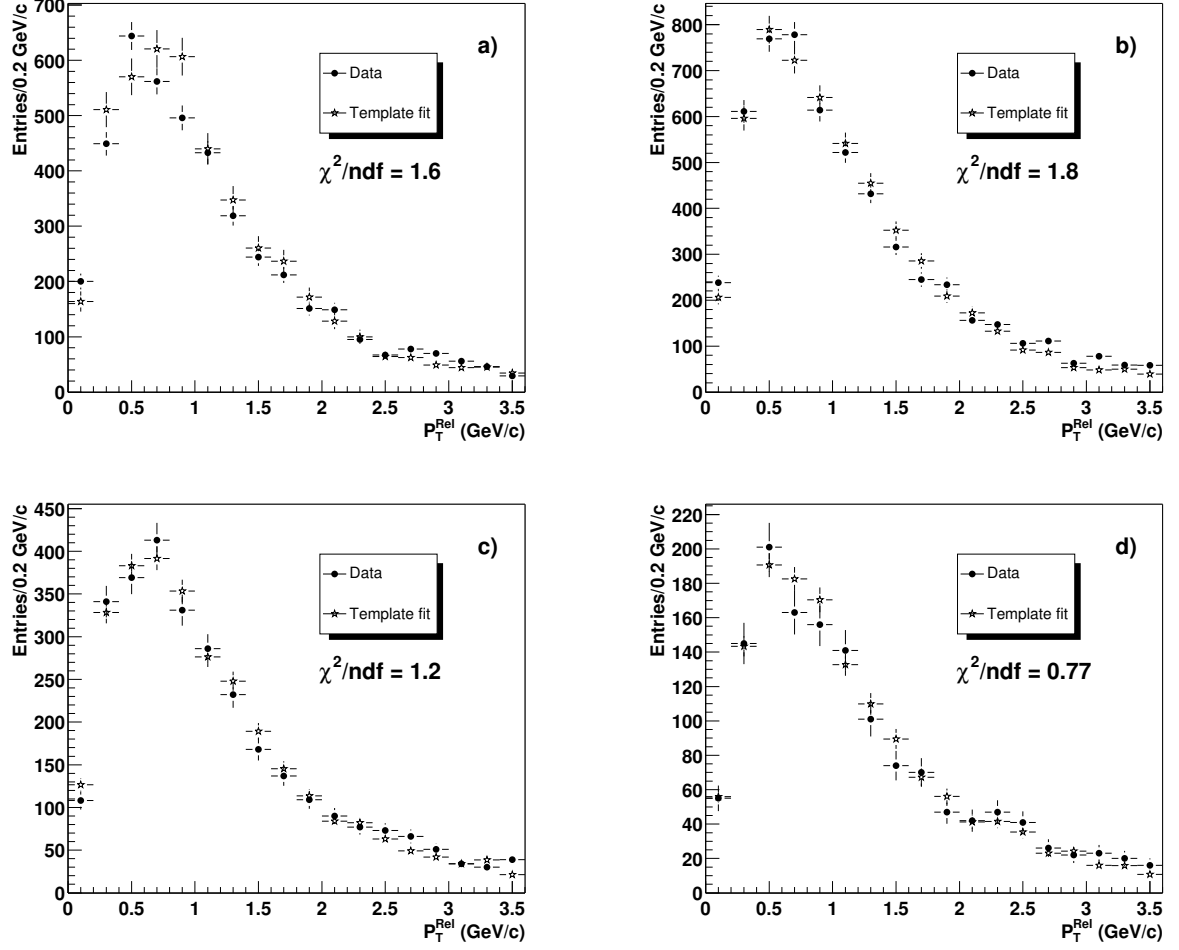


Figure 8.9: Fit of the background template, extracted from the data using central tracks, and the signal template, to the data in each of the four E_T^{jetCal} bins.

E_T^{jetCal} range	b-content	background content
20 - 25 GeV	0.32 ± 0.041	0.68 ± 0.043
25 - 35 GeV	0.29 ± 0.028	0.71 ± 0.030
35 - 50 GeV	0.24 ± 0.031	0.76 ± 0.034
50 - 100 GeV	0.19 ± 0.043	0.81 ± 0.048

Table 8.2: The b -jet and background content in each bin of E_T^{jetCal} , where the background template is extracted from the data using central tracks.

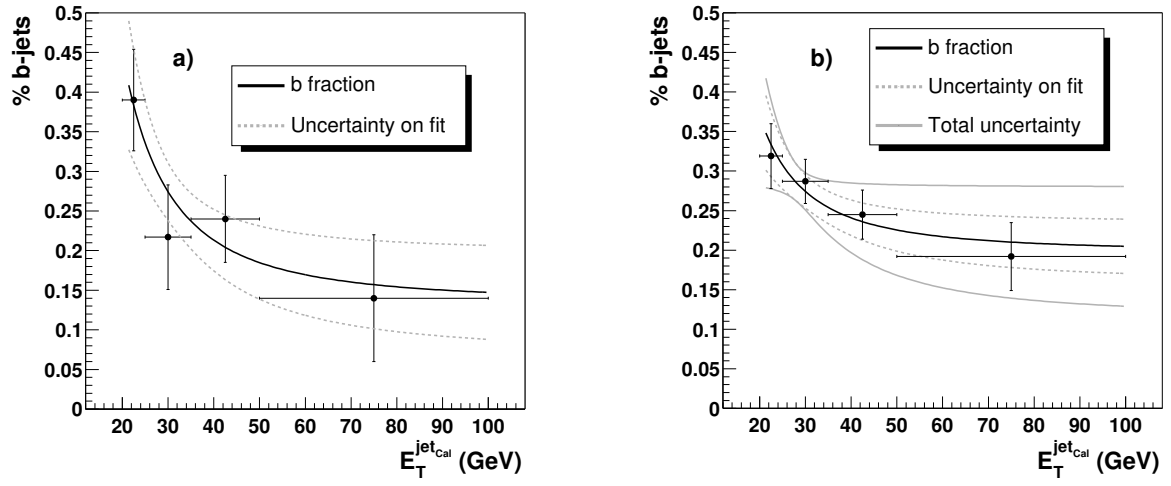


Figure 8.10: Measured *b*-jet content as function of $E_T^{\text{jet cal}}$, using the background template extracted from the QCD Monte Carlo simulation (a), and the template extracted from the data (b). The errors from the fit are represented by the gray dotted lines. The solid line in figure b includes the systematic error from the method.

8.2 b -jet cross section

Using the b -jet content measured above, we can now extract the b -jet cross section from the measured μ +jet spectrum (corrected for all efficiencies). This is done on a bin-by-bin basis, where every bin is weighted with the b -jet content that corresponds to its E_T . The errors on the fit parameters of equation 8.6 are taken into account by propagating the full covariance matrix. This results in the b -jet cross section of figure 8.11, measured as a function of E_T^{jetCal} , as it is measured in the calorimeter. The next step will therefore be to correct for the detector effects on the measurement of the b -jet cross section.

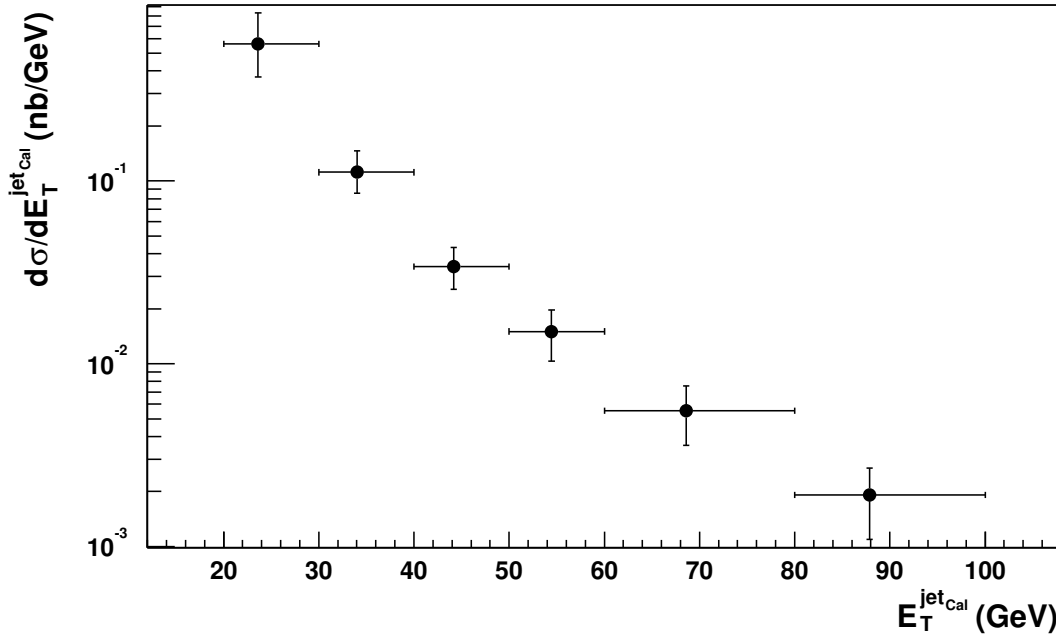


Figure 8.11: The b -jet cross section, with $b \rightarrow \mu$, as a function of calorimeter E_T^{jetCal} .

8.2.1 Unfolding the b -jet cross section

We now proceed to unfold the b -jet cross section, measured as function of E_T^{jetCal} , according to equation 8.2, for the effect of the finite resolution of the calorimeter. This only accounts for the jet resolution, and does not take into account the muon and neutrino which are present in the jet. The latter correction will be discussed in the next section.

To unfold the b -jet cross section we follow the procedure outlined in section 7.3. Again, we start with an ansatz function with three free parameters, as shown in equation 7.3, and schematically displayed in figure 8.12a. We smear this distribution with the jet energy resolution (resulting in figure 8.12b), and fit to the b -jet cross section measured in the previous section. Upon convergence of the fit, we use the ratio of the smeared ansatz function to the ansatz function to scale the data points. This ratio is shown in figure 8.13. We also have to make the kinematic acceptance correction as explained in section 7.4, to define the b -jet cross section, measured as function of $E_T^{jet_P}$, as:

$$\frac{d\sigma}{dE_T^{jet_P}} = \frac{K(E_T^{jet_P})}{U(E_T^{jet_{Cal}})} \frac{d\sigma}{dE_T^{jet_{Cal}}} \quad (8.7)$$

which combines equation 8.2 and equation 8.3. This results in the b -jet cross section as function of $E_T^{jet_P}$ as shown in figure 8.14.

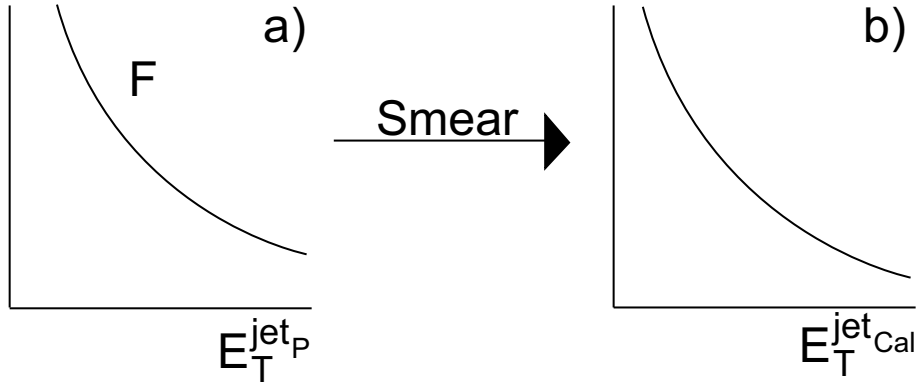


Figure 8.12: Schematic view of the procedure taken to unfold the b -jet cross section. Figure a shows the ansatz function F as function of $E_T^{jet_P}$, which is smeared according to the jet resolution to get the distribution as function of E_T^{jet} .

8.2.2 Resolution and lepton corrections

To measure the b -jet cross section as a function of the full b -jet energy $E_T^{jet_{PL}}$, including the muon and neutrino energies, we follow a similar method as the one described in the previous section. Adding the muon and neutrino energies increases the b -jet energy, changing the scale of the cross section from the measured jet E_T , $E_T^{jet_{Cal}}$, to the unfolded and lepton corrected jet E_T , $E_T^{jet_{PL}}$. Thus, we need to devise a correction

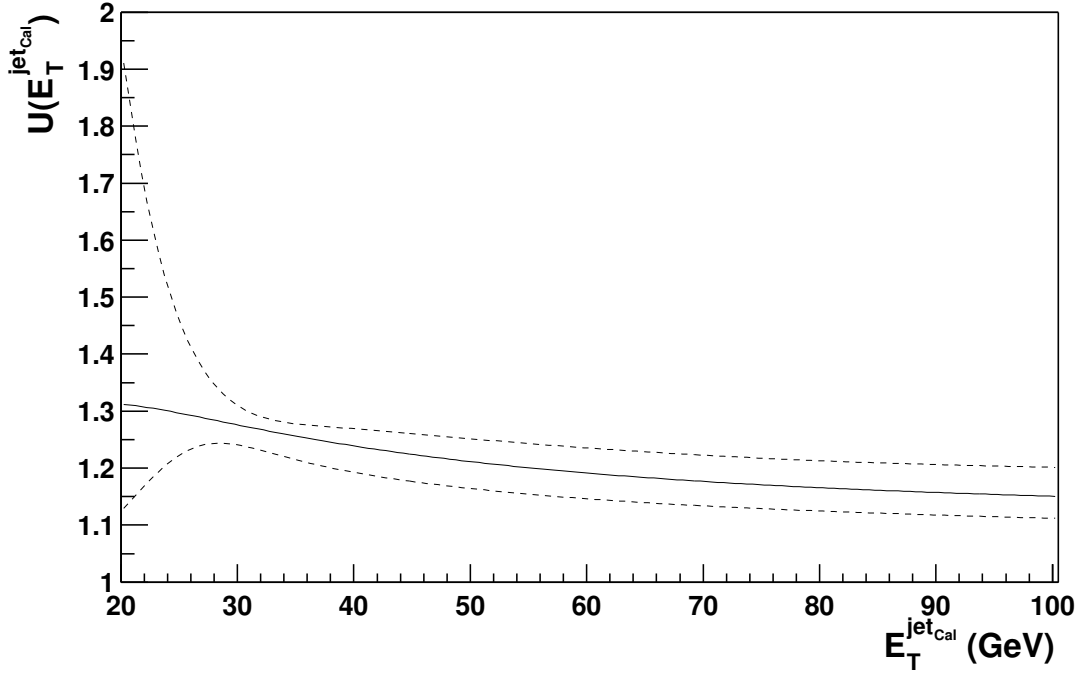


Figure 8.13: Ratio $U(E_T^{jetCal})$ between the smeared ansatz and the ansatz function. The dashed lines represent the errors on this ratio.

function $S(E_T^{jetCal})$, which is a function of E_T^{jetCal} and scales the data points to the appropriate value of E_T^{jetPL} . For this, we construct a model of the b -jet cross section, which corresponds to the function F in equation 8.1. According to the same equation, we correct this function to get the function G which can be compared to the measured data points. We then have to devise the function $S(E_T^{jetCal})$ such, that it transforms the function G back to the underlying function F . The function S can then also be used to scale the b -jet cross section in the data, measured as function of E_T^{jetCal} , to a b -jet cross section measured as function of E_T^{jetPL} .

We start with the underlying distribution F , for which we assume a shape according to:

$$F(E_T^{jetPL}, \alpha, \beta, \gamma) = \alpha \left(E_T^{jetPL} \right)^\beta \left(1 - \left(\frac{2}{\sqrt{s}} \right) E_T^{jetPL} \right)^\gamma \quad (8.8)$$

which is a function of the total b -jet transverse energy, including the transverse muon and neutrino energy (schematically depicted in figure 8.15a). This distribution is taken as an ansatz function which we now correct for the effects listed in equation 8.1.

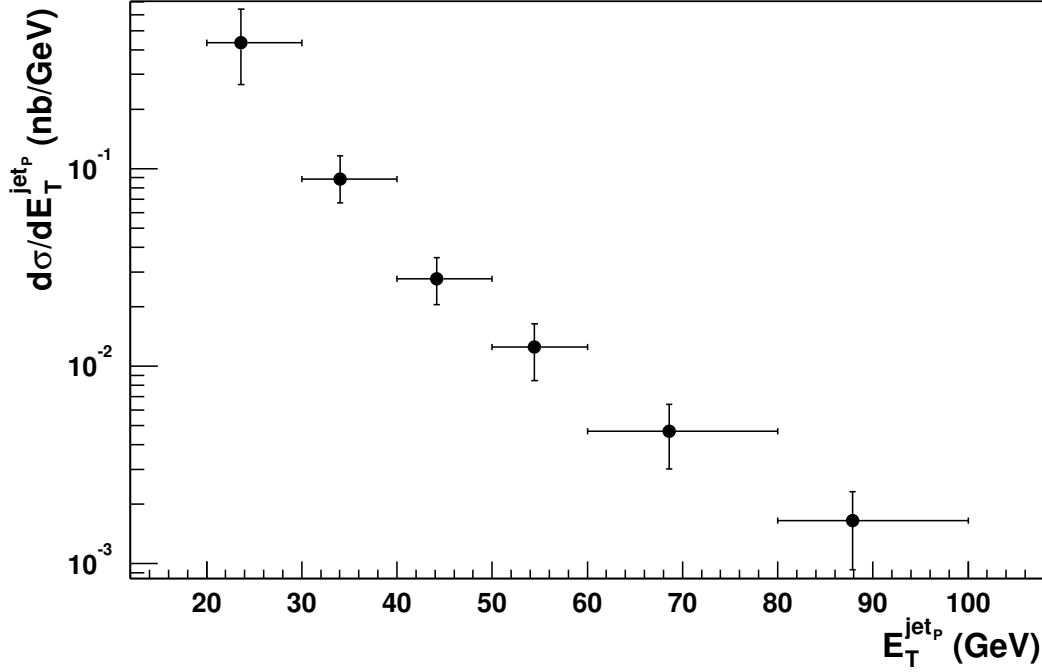


Figure 8.14: The *b*-jet cross section as a function of particle level transverse jet energy, $E_T^{jet_P}$, without muon and neutrino energies.

The first correction is for the contribution of the muon and neutrino energy to the *b*-jet. This correction is extracted from the Monte Carlo simulation, by generating QCD events and extracting the $b\bar{b}$ events, with at least one *b*-quark decaying to a muon, and with both the jet and the muon in the correct fiducial volume. We then plot:

$$C_L(E_T^{jet_{PL}}) = \frac{E_T^{jet_{PL}}}{E_T^{jet_P}} \quad (8.9)$$

as a function of $E_T^{jet_{PL}}$, where

$$E_T^{jet_{PL}} = E_T^{jet_P} + p_T^\mu + p_T^\nu \quad (8.10)$$

This results in the scatter plot shown in figure 8.16. The spread in each vertical slice of this scatter plot can be interpreted as a resolution effect on the jet energy, caused by the uncertainty on the energy carried away by the muon and the neutrino. We have to take into account this scatter, to correct for possible changes to the cross section that this resolution effect might incur. The distribution in each vertical slice of this scatter plot is used to map each point of the ansatz function to a distribution as function of

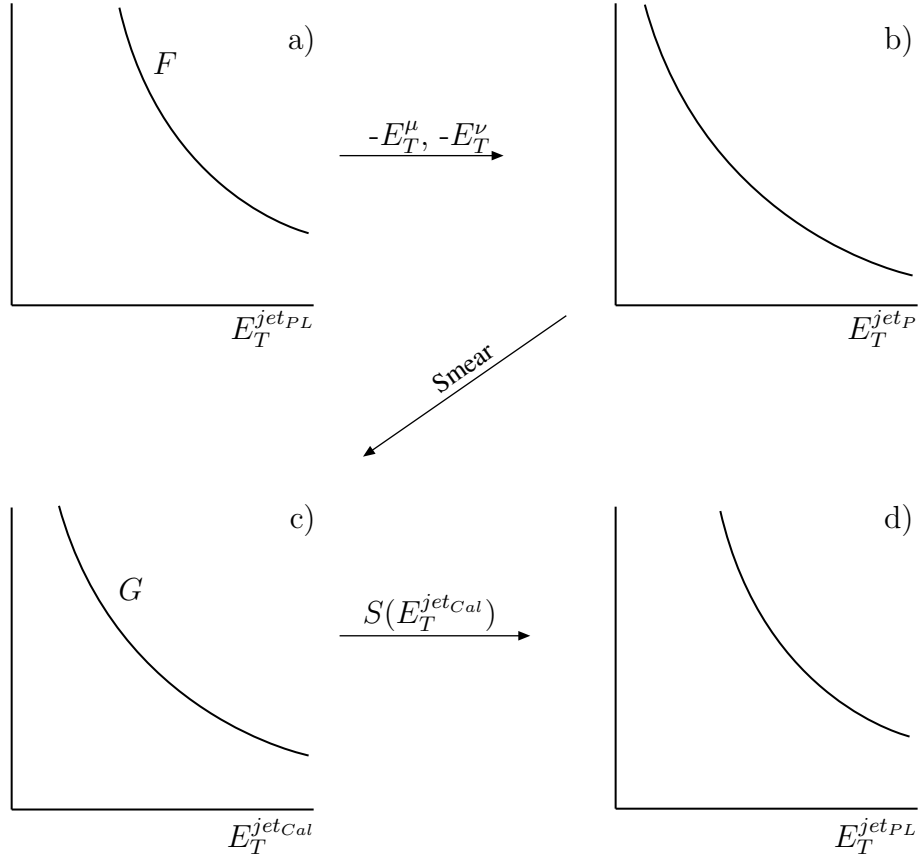


Figure 8.15: *Schematic illustration of the lepton correction and unfolding procedure.*

$E_T^{jet_P}$, which, integrated over all points of the ansatz function, results in a distribution as shown in figure 8.15b.

The next step is to take into account the resolution of the calorimeter. Each value of $E_T^{jet_P}$ in the distribution of figure 8.15b has a resolution associated with it, as discussed in section 5.2. Therefore, we fold each point on the distribution with a gaussian shape, with the width of the gaussian corresponding to the resolution. This results in the distribution of figure 8.15c, which is now a function of the transverse calorimeter jet energy, $E_T^{jet_{Cal}}$. This distribution corresponds to the measured data points that are displayed in figure 8.14.

The function S , which transforms the distribution as function of $E_T^{jet_{Cal}}$ into the true distribution $E_T^{jet_{PL}}$ can now be extracted using the method described above. Each

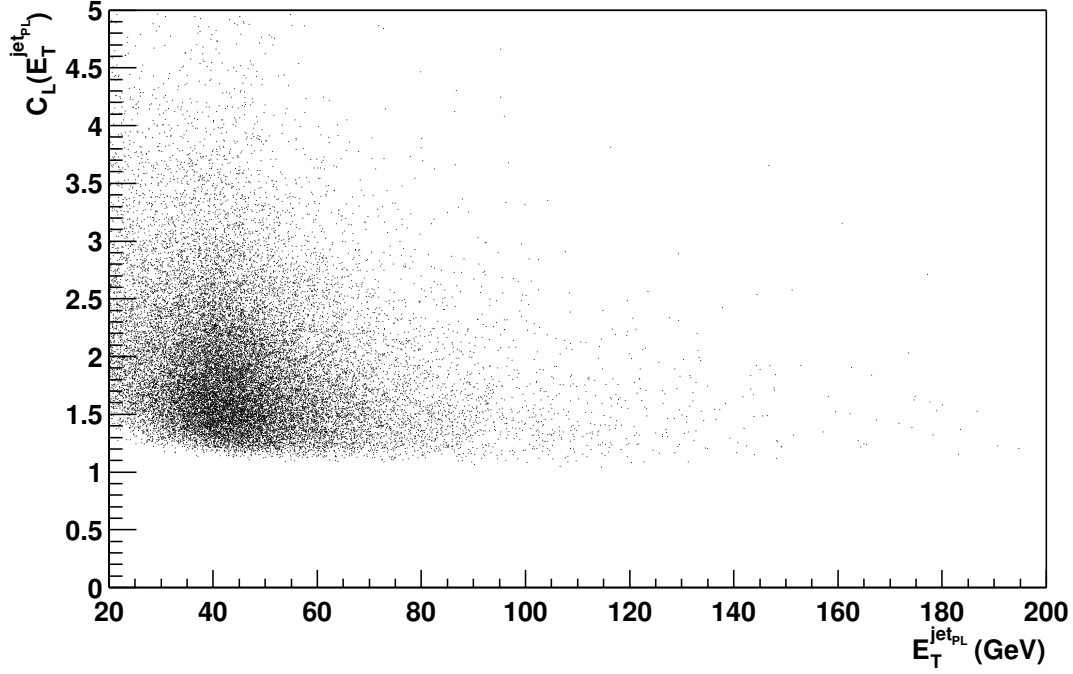


Figure 8.16: Lepton correction factor $C_L^{jet_{PL}}$ as a function of the total b -jet transverse energy $E_T^{jet_{PL}}$.

point on the original ansatz function F maps to a distribution as a function of $E_T^{jet_{Cal}}$. This distribution is shifted to the left and has a well defined maximum. Since S needs to be the inverse of this mapping, we choose S such that it scales the maximum of this distribution to the original point on the function F , resulting in figure 8.15d. This distribution can now be seen as the smeared ansatz function.

Each data point, measured at a certain value of $E_T^{jet_{Cal}}$, is scaled using the derived function S to the corresponding value of $E_T^{jet_{PL}}$, taking into account the bin sizes. The smeared ansatz function, which is also a function of $E_T^{jet_{PL}}$ and can be compared directly to the scaled data points, is fit to these data points by changing the parameters in the original ansatz function, by minimizing the χ^2 , defined as:

$$\chi^2 = \sum_{i=1}^{i=6} \left(\frac{\Delta_i}{\epsilon_i} \right)^2 \quad (8.11)$$

where Δ_i is the difference between the data and the smeared ansatz for data point i , and ϵ_i is the error on data point i .

Upon convergence of the fit, the resulting ansatz function now represents the true b -jet cross section as a function of lepton corrected transverse energy. Figure 8.17

shows the result of the fit, where the dotted curve is the smeared ansatz function. The smeared ansatz function fits the data points well ($\chi^2 = 0.11$). Figure 8.18 shows the ratio of the smeared ansatz and ansatz function. The dotted curves represent the error on the ratio, resulting from varying the measured jet resolution, taking into account the full covariance matrix.

The scaled data points are now multiplied by the ratio shown in figure 8.18 to arrive at the b -jet cross section as a function of total jet E_T . What remains is to correct for the $b \rightarrow \mu$ branching ratio and the kinematic acceptance to get the final differential b -jet cross section.

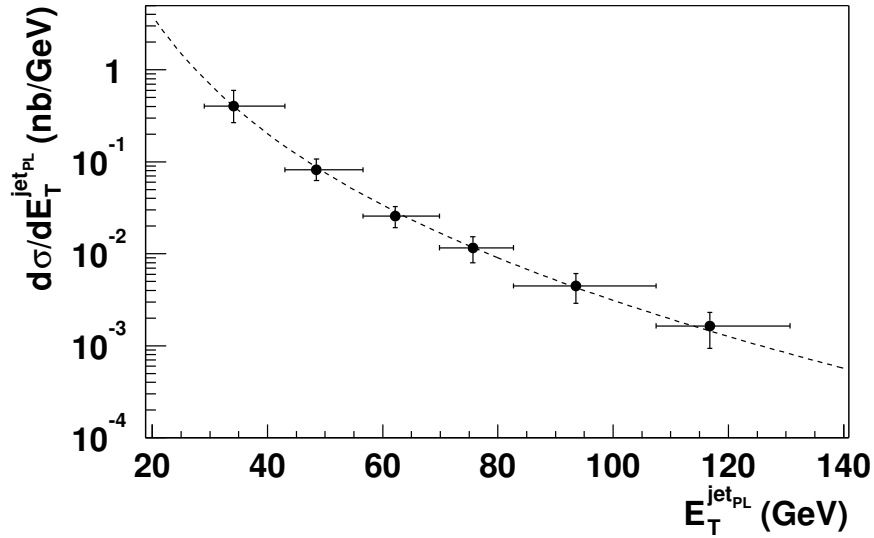


Figure 8.17: Result of fit to scaled data points. The dotted curve represents the smeared ansatz function.

Purity considerations

The procedure discussed above can only be used if sufficient events in a certain measured $E_T^{\text{jet}_{Cal}}$ region, i.e. bin, originate from that particular region. If too many events migrate into that bin from other bins, the number of events in the bin does not represent the cross section in the corresponding $E_T^{\text{jet}_{Cal}}$ region. Therefore, we define the purity in a particular bin as the number of events in that bin of $E_T^{\text{jet}_{PL}}$ in the ansatz function, divided by the number of events in that same bin in the smeared ansatz function. We also define the efficiency in that bin as the percentage of the events that does not smear out of the bin during the smearing procedure. For the six data points

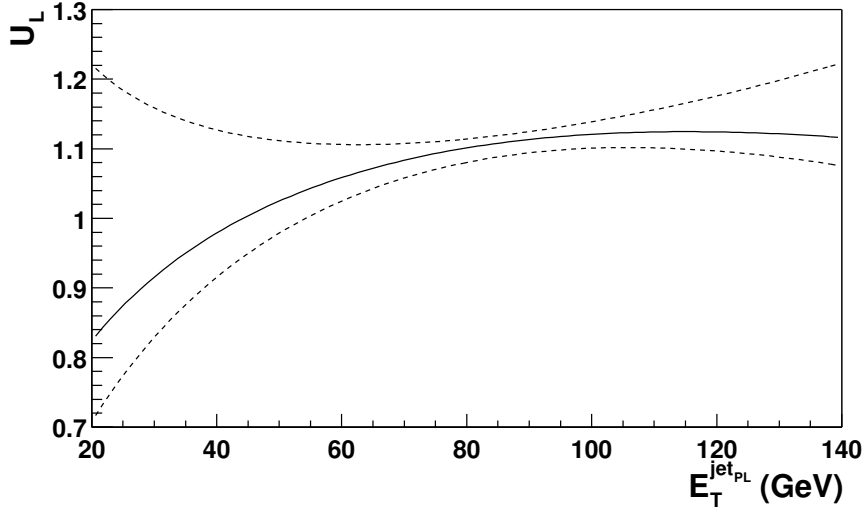


Figure 8.18: *The ratio between the smeared ansatz function and the ansatz function. The dotted lines represent the errors on the ratio that are coming from the uncertainty on the jet energy resolution function.*

used in the procedure above, the purities and efficiencies are listed in table 8.3. Clearly the purities are on the low side to justify the bin sizes used. We therefore choose to decrease the number of bins and increase their size such that the purity is at least 50% in each bin. Table 8.4 lists the efficiencies and purities for three bins, which are appropriate for a correct unfolding procedure.

$E_T^{jet_{Cal}}$ bin (GeV)	$E_T^{jet_{PL}}$ bin (GeV)	Purity	Efficiency
20-30	29-43	42	42
30-40	43-57	36	38
40-50	57-70	30	31
50-60	70-83	27	31
60-80	83-107	37	42
80-100	107-131	29	37

Table 8.3: *Purities and efficiencies for 6 bins in the data.*

$E_T^{jet_{Cal}}$ bin (GeV)	$E_T^{jet_{PL}}$ bin (GeV)	Purity	Efficiency
20-38	29-54	54	52
38-60	54-83	50	53
60-100	83-131	51	59

Table 8.4: *Purities and efficiencies for 3 bins in the data.*

8.3 Kinematic acceptance and branching ratio

Ultimately, we want to measure the inclusive differential b -jet cross section in the range $|\eta^{jet}| < 0.6$. Up to now, we have required a muon with $p_T^\mu > 6$ GeV/c, and we need to correct for this. We also have to apply a small correction due to smearing of reconstructed jets and muons in and out of the fiducial region. Both these corrections are again extracted from the Monte Carlo simulation, where we extract two distributions:

1. The distribution of generated b -jets, without any constraints on the decay of the b -quark in the jet. The jet is required to be within $|\eta^{jet}| < 0.6$.
2. The distribution of generated b -jets, with the b -quark decaying to a muon. After smearing the jet η according to the detector resolution, we require that $|\eta^{jet}| < 0.6$. Also, after smearing the properties of the muon, it is required to have $p_T^\mu > 6$ GeV/c, and $|\eta^\mu| < 0.8$.

Both distributions are made as a function of $E_T^{jet_{PL}}$. The ratio between distributions 1 and distribution 2 can now be used to scale the measured b -jet cross section in the data. This ratio is shown in figure 8.19. Scaling the measured b -jet cross section with this ratio results in the differential b -jet cross section as shown in figure 8.20. This b -jet cross section can now be compared directly with theoretical predictions, as will be done in the next chapter.

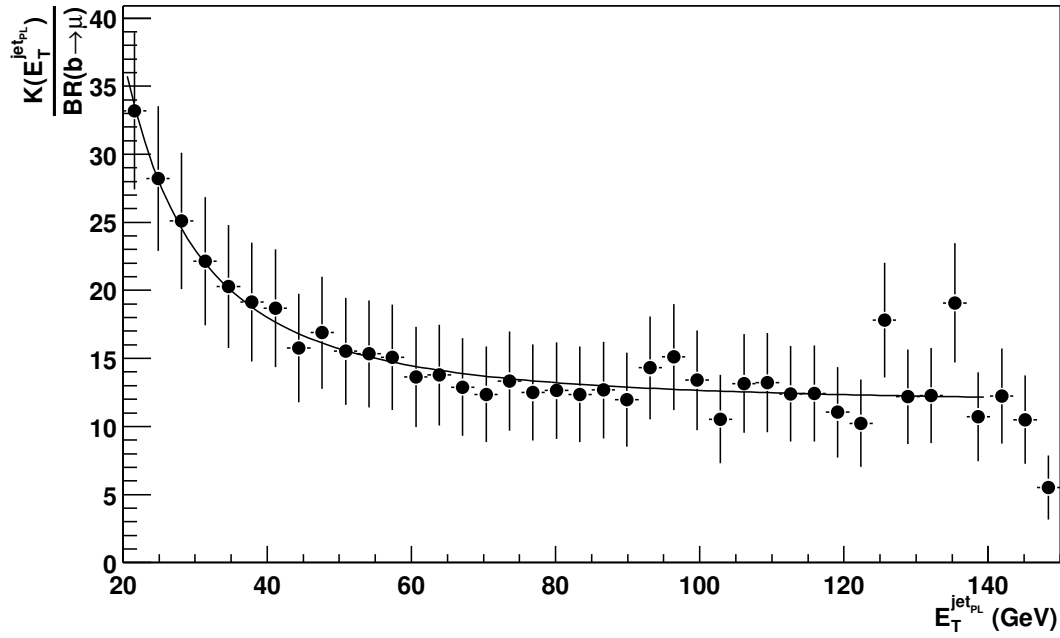


Figure 8.19: Ratio between the number of generated b -jets and b -jets that decay to a muon with $p_T^\mu > 6 \text{ GeV}/c$.

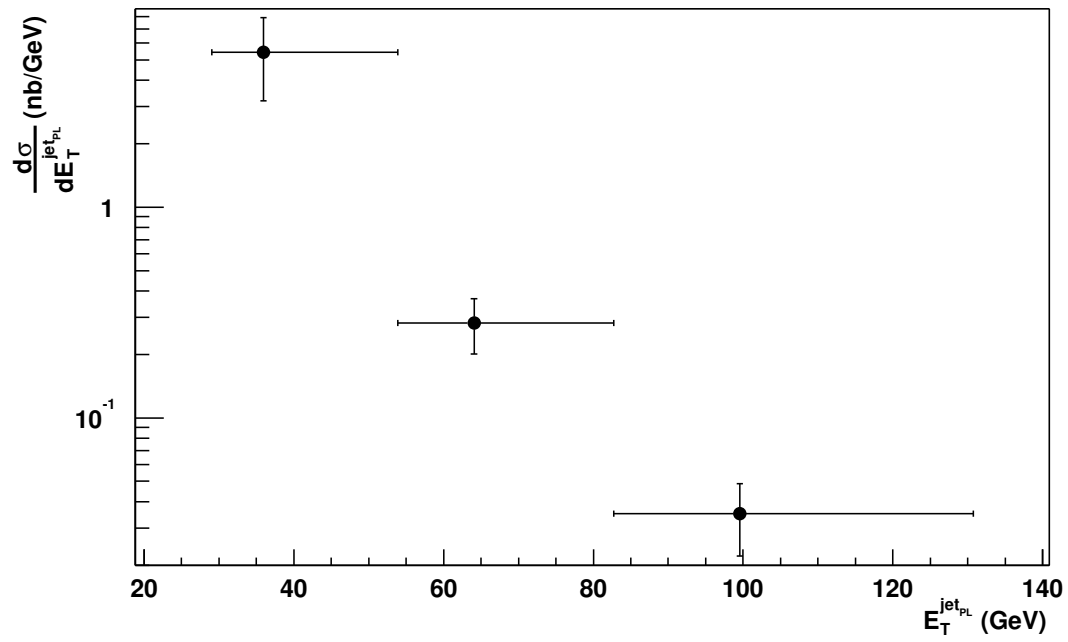


Figure 8.20: *Differential b -jet cross section as function of total b -jet E_T , corrected for all detector and tagging effects.*

Chapter 9

Theory comparison

The measured differential b -jet cross section, corrected for all detector effects and branching ratios can now be directly compared with theory predictions. For this comparison we use the next-to-leading Standard Model calculation written by Mangano, Nason and Ridolfi (MNR), as described in section 2.2, as well as the Pythia Monte Carlo simulation.

9.1 Comparison of data and theory

As has been explained in section 2.2, we compare the calculation of the next to leading order production rate of b -jets with that in the data, and not that of b -quarks, to avoid the effects of collinear gluons and fragmentation effects. We can directly compare the output of the MNR calculation with the measured data points shown in figure 8.20. Hadronization and fragmentation effects do not play a role since they are largely absorbed in the jet algorithm. The fragmentation out of the cone is taken care of by the particle imbalance correction, described in section 5.2.

Figure 9.1 shows the result of the theory calculation, compared with the data points. The error bands on the theory prediction reflect the uncertainty due to the fragmentation and hadronization scales, and the mass of the b -quark. The ratio of the data to the theory calculation, for both the central value (black dots) and the upper error band of the calculation (open circles) is shown in figure 9.2.

9.1.1 χ^2 comparison of data and theory

We now proceed by quantifying the comparison between the data and theory by means of a χ^2 comparison. The varying sources of the errors on the data points are itemized

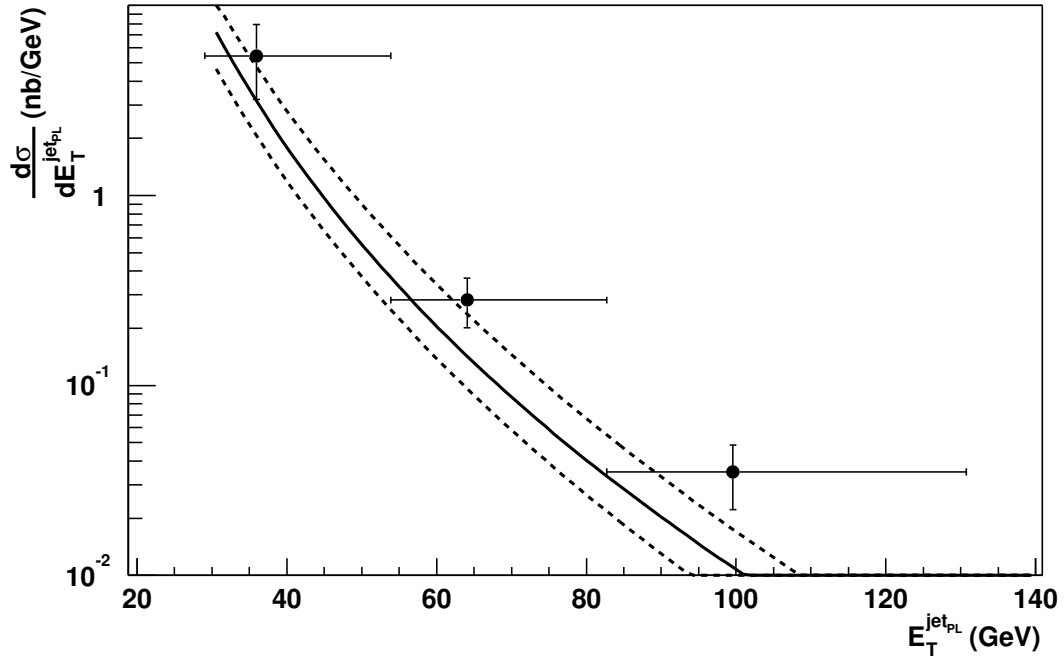


Figure 9.1: *Comparison of data to theory.*

below.

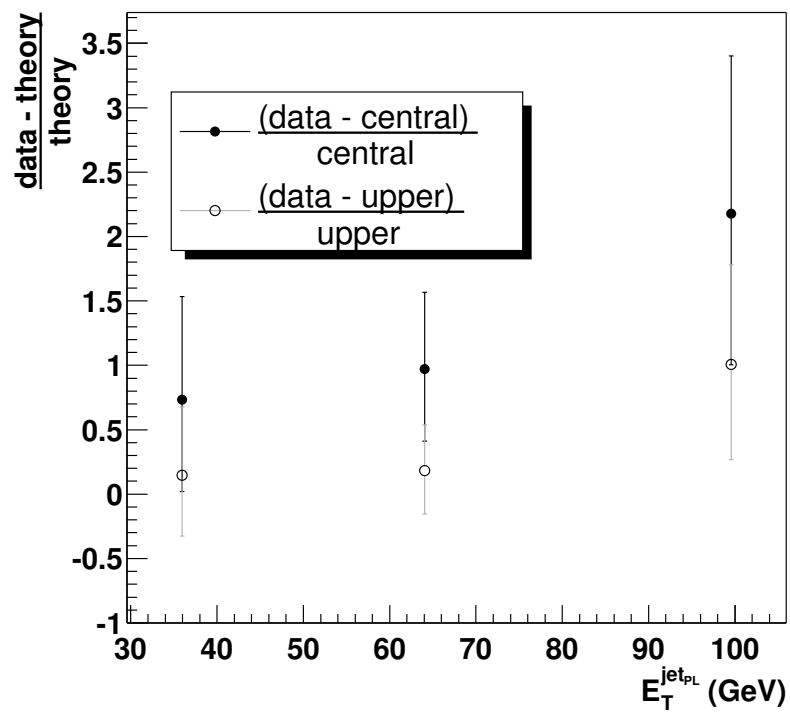


Figure 9.2: Ratio of data to theory for both the central value of the theory prediction (black dots) as the upper band of the theory prediction (open circles).

Fully correlated uncertainties

- Integrated luminosity;
- Level 1 muon trigger efficiency;
- Muon reconstruction efficiency;
- Jet Energy Scale;
- Jet energy resolution unfolding and lepton correction;
- Level 1 jet trigger efficiency;
- Jet identification efficiency;

Partially correlated uncertainties

- B -content measurement. This is a fitted function of two parameters, which results in a partial correlation between the three data points. It also includes the systematic error resulting from the use of different background templates.

Fully uncorrelated uncertainties

- Statistical errors.

The cross section values and uncertainties are listed in table 9.1.

$E_T^{jet_{PL}}$ (GeV)	$\frac{d\sigma}{dE_T^{jet_{PL}}}$ (nb/GeV)	Statistical uncertainty (%)	Fully corr. uncertainty (%)	Part. corr. uncertainty (%)
35.9	5.44	1.4907	42.1	12.9
64.1	0.28	2.24184	20.9	21.2
99.6	0.035	4.17242	22.1	31.1

Table 9.1: *Cross section values and uncertainties.*

We calculate the χ^2 by:

$$\chi^2 = D^T V^{-1} D \quad (9.1)$$

where D is the vector of differences between the data points and the theory, and V is the covariance matrix of the points. If we consider a source of uncertainty d_k , with

error σ_k , the elements of the correlation matrix V are given by:

$$V_{ij}^k = \frac{\delta B(E_T^{jetPL})_i(\sigma_k)_i \Lambda_{ij}}{\delta d_k} \frac{B(E_T^{jetPL})_j(\sigma_k)_j}{\delta d_k} \quad (9.2)$$

$$= \Delta_k B(E_T^{jetPL})_i \Lambda_{ij} \Delta_k B(E_T^{jetPL})_j \quad (9.3)$$

The factors Λ_{ij} depend on whether the source of the uncertainty is fully, partially or not correlated, according to:

- The completely uncorrelated uncertainties add to V_{ij} with $\sigma_i \delta_{ij} \sigma_j$, therefore $\Lambda_{ij} = \delta_{ij}$;
- The fully correlated uncertainties add to V_{ij} with $\sigma_i \sigma_j$ and $\Lambda_{ij} = 1$;
- The partially correlated uncertainties add to V_{ij} with $\sigma_i \rho_{ij}^k \sigma_j$, where $\Lambda_{ij} = \rho_{ij}^k$ is the covariance matrix for each systematic error.

The only partially correlated error is the b -content uncertainty, for which the correlation matrix will be derived below.

9.1.2 The correlation matrix for the b -content fit

For the b -jet content measurement as explained in section 8.1, we fit a function $B(x; a, b)$ with two free parameters, a and b to four data points by minimizing the χ^2 , defined as:

$$\chi^2 = \frac{1}{N} \sum_{i=1}^N \frac{(B(x_i) - R_i)^2}{\sigma_i^2} \quad (9.4)$$

where R_i is the measured b -content in bin i . This fit results in the optimal values of a and b , called a_0 and b_0 , that minimize the χ^2 , and it returns a covariance matrix of the form:

$$E = \begin{pmatrix} \sigma_a^2 & \rho_{ab} \sigma_a \sigma_b \\ \rho_{ab} \sigma_a \sigma_b & \sigma_b^2 \end{pmatrix} \quad (9.5)$$

where σ_a is the error on parameter a , σ_b is the error on parameter b and ρ_{ab} is the correlation between the two parameters. This covariance matrix can be used to calculate the deviation ΔB for each point on the function, according to:

$$(\Delta B(E_T^{jetCal}))^2 = \left(\frac{\delta B}{\delta a} \quad \frac{\delta B}{\delta b} \right) E \begin{pmatrix} \frac{\delta B}{\delta a} \\ \frac{\delta B}{\delta b} \end{pmatrix} \quad (9.6)$$

This results in the error bands as shown for example in figure 8.10.

For the covariance matrix V that is used to calculate the χ^2 between the data and theory prediction, we need a similar covariance matrix as described above for E , but

now not giving the covariance between the two parameters a and b , but between two different points on the function B ; something which can loosely be described as the covariance of the function B with itself. This will tell us how the data points in the b -jet cross section shown in figure 9.1 are correlated, if the shape of the function B changes. This covariance matrix for point to point correlations in the function B is defined as:

$$E_{ij} = \rho_{ij} \Delta B_i \Delta B_j \frac{\delta B}{\delta x_i} \frac{\delta B}{\delta x_j} \quad (9.7)$$

where ρ_{ij} is the correlation matrix between the points i and j , which is symmetrical and unit for $i = j$. ΔB_i is the deviation of B at point i , as shown in equation 9.6. We now describe how we can numerically construct this covariance matrix E . The parameters a_0 and b_0 provide the best fit and minimize equation 9.4 to $\chi^2 = \chi_0^2$. We can now do a large number of hypothetical experiments, where we generate the parameters (a, b) around (a_0, b_0) from a gaussian distribution with width (σ_a, σ_b) . Each experiment results in a new function $B(x; a_k, b_k)$ with a corresponding χ^2 . We now obtain the covariance matrix E by:

$$E_{ij} = \frac{1}{S} \sum_{k=1}^N \frac{(B(x_i; a_k, b_k) - \langle R_i \rangle)(B(x_j; a_k, b_k) - \langle R_j \rangle)}{\sqrt{\Delta \chi^2}} \quad (9.8)$$

where $\langle R_i \rangle = B(x_i; a_0, b_0)$ and

$$S = \sum_{k=1}^N \frac{1}{\sqrt{\Delta \chi^2}} \quad (9.9)$$

We weigh each experiment with the inverse square root of the χ^2 to normalize each experiment to the 1σ contour of the gaussian distribution. The variances (on the diagonal) now give the (squared) errors on $B(x_i)$ and the off-diagonal elements give the covariances at each point x_i with respect to another point x_j . We now extend this algorithm to calculate the impact of the errors on a and b on the final b -jet cross section. We again take a large sample of (a_k, b_k) parameters. The reference function R is now the b -jet cross section as shown in 9.1, while the trial functions are the resulting b -jet cross sections as measured using the new parameters (a_k, b_k) . Using equation 9.8 then results in a covariance matrix E which can be used directly in equation 9.3.

9.2 Covariance matrix and result

Using equation 9.3 results in the following inverted covariance matrix:

$$V^{-1} = \begin{pmatrix} 0.311 & -4.393 & -14.91 \\ -4.393 & 239.0 & -285.6 \\ -14.91 & -285.6 & 7634 \end{pmatrix}$$

Applying this matrix to the central value and uncertainty bands shown in figure 9.1, using equation 9.1, yields:

- Central prediction: $\chi^2 = 4.30$ (23.1 %)
- Upper prediction: $\chi^2 = 1.90$ (59.3 %)
- Lower prediction: $\chi^2 = 6.50$ (9.0 %)

The percentages quoted are the probabilities that a random repeat of this experiment results in a greater χ^2 [1]. Clearly, the data points favor the upper band of the theory.

We can also compare the data results with the prediction of Pythia. For this, we run Pythia in the MSEL=0 mode, which takes into account the next-to-leading order b -producing processes, and extract the b -jet cross section. This results in figure 9.3. The χ^2 comparison between the data and Pythia results in $\chi^2 = 1.82$, with a significance level of 61.6%.

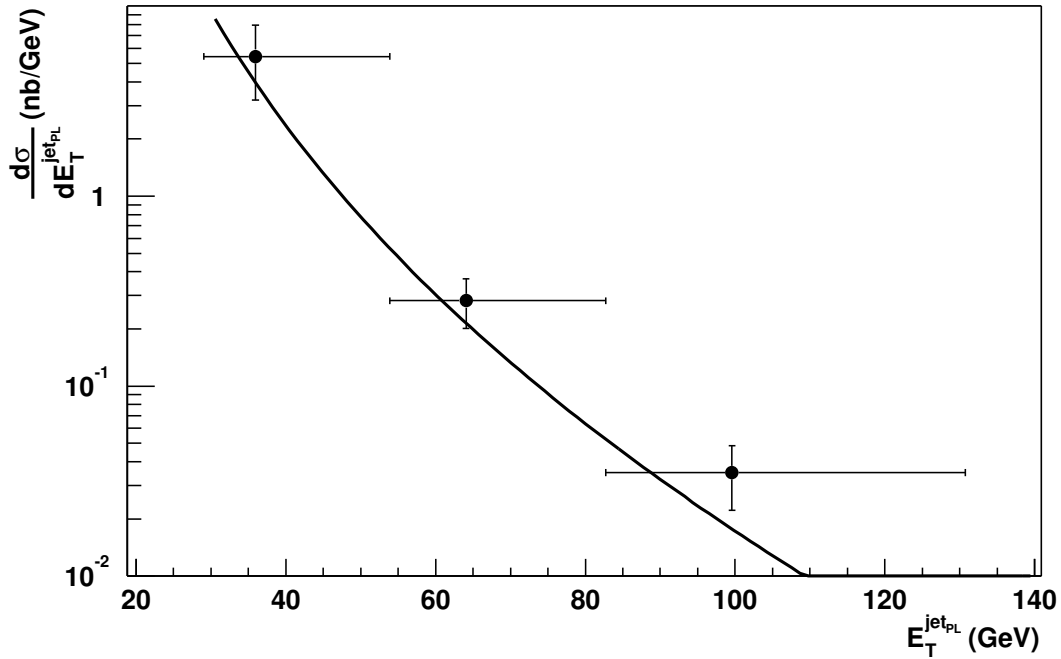


Figure 9.3: Comparison of the data to the cross section as predicted by the Pythia Monte Carlo simulation.

9.3 Comparison to the uncorrected b -jet cross section

One of the main effects on the value of the cross section is the correction of the energy of the muon and neutrino in the jet. Since we have also measured the b -jet cross section as a function of $E_T^{jet_P}$, we can compare this to the theoretical prediction. The black points in figure 9.4 show this b -jet cross section. The curves show the prediction as calculated by the MNR program, modified for the energy loss of the muon and neutrino. This energy loss is extracted using the Pythia Monte Carlo simulation. This simulation provides the cross section as function of the full b -jet E_T , $E_T^{jet_{PL}}$. It also provides the b -jet cross section as a function of particle level E_T , without the muon and neutrino, $E_T^{jet_P}$. If we weigh each Pythia event that enters in the latter cross section by the ratio of the MNR prediction with the Pythia prediction of the full b -jet cross section, the resulting cross section corresponds to MNR cross section without the muon and neutrino contribution. The dotted lines correspond to the theoretical error on the theoretical prediction, which are derived according to the same method.

For this comparison, we can also derive the covariance matrix (as shown on the next page) and calculate the χ^2 as we have done above. This results in:

- Central prediction: 3.82 (70.1 %)
- Upper prediction: 2.32 (88.8 %)
- Lower prediction: 5.35 (50.0 %)

Again, the measurement favors the upper band of the theory.

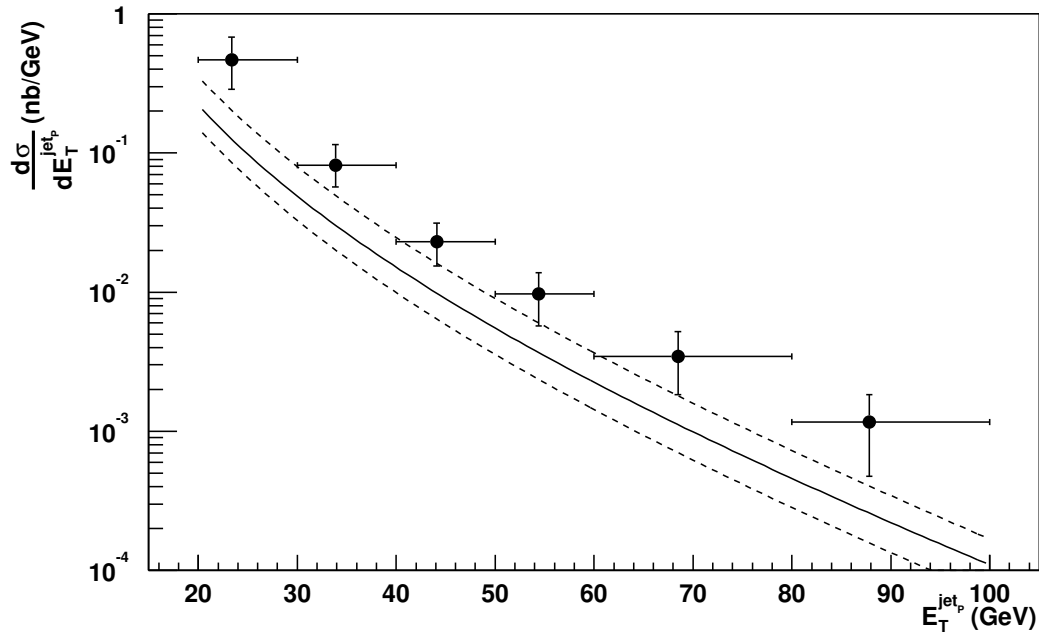


Figure 9.4: Comparison of the data to the cross section as predicted by MNR and scaled by Pythia.

$$V^{-1} = \begin{pmatrix} 100.5 & -560.5 & -14.639 & -27.88 & 301.84 & -15936 \\ -560.5 & 5520 & -3019 & -4771 & -8924 & -2.683 \cdot 10^4 \\ -14.64 & -3019 & 2.552 \cdot 10^4 & -7321 & -1.359 \cdot 10^4 & -1.715 \cdot 10^4 \\ -27.88 & -4771 & -7321 & 1.006 \cdot 10^5 & -2.219 \cdot 10^4 & -5.140 \cdot 10^4 \\ 301.8 & -8924 & -1.359 \cdot 10^4 & -2.219 \cdot 10^4 & 4.566 \cdot 10^5 & -1.055 \cdot 10^5 \\ -1593 & -2.683 \cdot 10^4 & -1.715 \cdot 10^4 & -5.140 \cdot 10^4 & -1.055 \cdot 10^5 & 3.761 \cdot 10^6 \end{pmatrix}$$

9.4 Conclusions

In this analysis the measurement of the differential b -jet cross section has been presented and confronted with theoretical predictions. First, the total b -jet cross section, fully corrected for all detector effects and lepton contributions is compared to the next-to-leading order calculation by Mangano, Nason and Ridolfi. The comparison to the central value of this prediction results in $\chi^2 = 4.30$. The upper error band of the theory gives a better fit to the data points, with a χ^2 of 1.90. This confirms earlier measurements where the data points prefer the upper band of the theory [33].

The measured data points are also compared with the Pythia Monte Carlo simulation, which takes into account the next-to-leading order processes. This comparison results in $\chi^2 = 1.82$, indicating a better fit than to the MNR calculation.

Due to the resolution effects associated with the energy carried away by the muon and neutrino of the b -quark decay, the comparison done above can only be done for three measured data points. By modifying the MNR calculation of the cross section for the energy loss associated with the muon and neutrino, its prediction can also be compared to the b -jet production cross section without the lepton correction. This comparison results in a χ^2 of 3.82 for the central prediction and $\chi^2 = 2.32$ for the upper prediction, again favoring the upper error band of the calculation.

9.5 Outlook

The data sample used in this analysis has been taken during the early days of a successfully operating DØ detector. Currently, both the accelerator and the detector have both been much improved. The peak luminosity delivered by the accelerator has been increased to $4.0 \cdot 10^{31} \text{ cm}^{-2}\text{s}^{-1}$, allowing the total data sample taken by DØ to increase to 120 pb^{-1} . The DØ detector itself has improved its trigger system over time. The Level 1 muon trigger now uses tracks found by the CTT to match to scintillator hits, while the calorimeter trigger extends out to an η range of 3.2, allowing a greater region of phase space in which the b -jet cross section can be measured. The Level 2 and Level 3 triggers are now fully implemented and functional, which results in a better selection of μ +jet events, at higher rates.

Offline, the reconstruction program has improved significantly. Especially the reconstruction of central tracks has improved such that local muon tracks can be matched with central tracks to get an enhanced measurement of the kinematic properties of the muon. Additionally, progress has been made on the understanding of the jet energy resolution and energy scales, which are the dominating errors in this analysis. This understanding decreases the errors on the measured data points, and also allows a more detailed (i.e. more data points) study of the data, and the comparison to the theory.

All of these points will allow a measurement of the b -jet cross section in a larger η range, with improved statistics and reduced systematic errors.

Bibliography

- [1] The European Physical Journal C. 15:191–194, 2000.
- [2] D. Adams. Finding Tracks. DØ Note 2958.
- [3] R. Barlow and C. Beeston. Fitting using finite Monte Carlo samples. *Computer Physics Communications*, 77:219–228, 1993.
- [4] M. Bhattacharjee. Technical Design Report, Level 2 Preprocessor for Central and Forward Preshower Triggers. Unsubmitted note, 1999.
- [5] A. Brandt. Triggering with the Forward Proton Detector. 1998.
- [6] T. Burnett. Arve - the Atlas Reconstruction environment, <http://b.home.cern.ch/b/burnett/www/arve/>. November 1998.
- [7] DØCollaboration. [http : //www.fnal.gov/pub/now/live_events/dzero_live.html](http://www.fnal.gov/pub/now/live_events/dzero_live.html).
- [8] DØCollaboration. High-pT Jets in pbarp Collisions at \sqrt{s} =630 and 1800 GeV. *Phys. Rev. D*, 64, 032003, 2001.
- [9] DØ Upgrade Collaboration. DØ Silicon Tracker Technical Design Report. DØ Note 2169.
- [10] The DØCollaboration. Proposal for a Forward Proton Detector at DØ.
- [11] Private communication with B. Abbott.
- [12] F. Déliot. The Fit Algorithm in muo_trackreco. Unsubmitted note, 2000.
- [13] A. Gordeev *et al.* Technical Design Report of the Forward Preshower Detector for the DØ Upgrade. DØ Note 3445.
- [14] B. Abbott *et al.* Specification of the Level 2 Central Tracking Trigger Preprocessor Gate. DØ Note 3645.
- [15] D. Edmunds *et al.* Technical Design Report for the Level 2 Global Processor.

- [16] F. Abe *et al.* Observation of Top Quark Production in $\bar{p}p$ Collisions. *Phys. Rev. Lett.*, 74:2626, 1995.
- [17] F. Borchering *et al.* CTT TDR for the upgrade L1/L2 tracking trigger. DØ Note 3551.
- [18] F. Canelli *et al.* Jet Energy Scale at DØ in Run II. DØ Note 4011.
- [19] G. Alexeev *et al.* Technical Design Report for the DØ Forward Muon Tracking Detector Based on Mini-Drift Tubes. DØ Note 3366.
- [20] J. Bantly *et al.* The Level 0 trigger for the DØ Detector. *IEEE Trans. Nucl. Sci.*, 41:1274–1279, 1994.
- [21] J. Pumplin *et al.* New Generation of Parton Distributions with Uncertainties from Global QCD Analysis. *JHEP*.
- [22] S. Abachi *et al.* Observation of the Top Quark. *Phys. Rev. Lett.*, 74:2632, 1995.
- [23] S. W. Herb *et al.* Observation of a Dimuon Resonance at 9.5 GeV in 400 GeV Proton-Nucleus Collisions. *Phys. Rev. Lett.*, 39:252, 1977.
- [24] T. Diehl *et al.* Design of the Central Muon System. DØ Note 3365.
- [25] U. Bassler *et al.* NADA, A New Event by Event Hot Cell Killer. DØ Note 3687.
- [26] V. Abramov *et al.* Technical Design Report for the DØ forward trigger scintillation counters. DØ Note 3237.
- [27] V. V. Ezhela *et al.* *Particle Physics, One Hundred Years of Discoveries.* "American Institute Of Physics", 1996.
- [28] S. Frixione and M. Mangano. Heavy-Quark Jets in Hadronic Collisions. hep-ph/9605270, 1996.
- [29] G. Hesketh. Track Extrapolation. September 2002.
- [30] K. Meier N. Hadley F. Aversa M. Greco P. Chiapetta J.Ph. Guillet Z. Kunszt S.D. Ellis J. Huth, N. Wainer and D. Soper. Toward a Standardization of Jet Definition. Proceedings of *Research Directions for the Decade, Snowmass 1990*.
- [31] O. Peters. Muon Segment Reconstruction - Linked List Algorithm. DØ Note 3901.
- [32] CFT Technical Design Report. *The DØ Upgrade Central Fiber Tracker*. 1997.

-
- [33] A. Sznajder and A. Maciel. Measurement of the b Jet Production Cross Section in $p\bar{p}$ Collisions at $\sqrt{s} = 1.8TeV$. DØ Note 3703.
- [34] J. J. Thomson. Cathode Rays. *Phil. Mag.*, 44:293, 1897.

Appendix A

Glossary

ARVE Atlas Reconstruction and Visualization Environment

CAL Calorimeter

CC Central Calorimeter

CFT Central Fiber Tracker, outer part of the inner tracker consisting of scintillating fibers

CHF Coarse Hadronic Fraction

CJT Level 1 Calorimeter Trigger Term

CPS Central Preshower

DØVE D0 Event Display, 3-dimensional wire frame event display

DSP Digital Signal Processor

EC Endcap Calorimeter

EMF Electromagnetic Fraction

FAMUS Forward Angle Muon System, forward muon spectrometer

FPD Forward Proton Detector

FPGA Field Programmable Gate Array

FPS Forward Preshower

ICR Inter Cryostat Region, the gaps between the central and forward calorimeters

JES Jet Energy Scale, correction on the energy of jets measured in the calorimeter

MDT Mini Drift Tube, used in the forward muon system to measure passing muon tracks

MTC Muon Trigger Card, used for the Level 1 Muon Trigger

NADA New Anomalous Deposit Algorithm, used to suppress hot cells in the calorimeter

PDT Pressurized Drift Tube, used in the central muon system to measure passing muon tracks

PS Preshower

SC Scintillating Counters of the muon system

SMT Silicon Microstrip Tracker, innermost tracking detector consisting of silicon strips

VME Versa Module Europa, bus system allowing communication between readout and trigger devices.

WAMUS Wide Area Muon System, central muon spectrometer